

Scanning Probe Microscopy Studies of Functional Molecular Structures Prepared via Electrospray Deposition

INAUGURALDISSERTATION

zur

Erlangung der Würde eines Doktors der Philosophie

vorgelegt der

Philosophisch-Naturwissenschaftlichen Fakultät

der Universität Basel

von

Sebastian Moritz Alexander Scherb

2022

Genehmigt von der Philosophisch-Naturwissenschaftlichen Fakultät
auf Antrag von:

Prof. Dr. Ernst Meyer
Prof. Dr. Martino Poggio
Dr. Clemens Barth

Basel, den 21. Juni 2022

Prof. Dr. Marcel Mayor, Dekan

Für meine Familie.

Abstract

FUNCTIONAL molecular materials built-up by self-assembly on surfaces in ultra-high vacuum (UHV) require rationally designed complex and appropriately equipped elementary building blocks. Access to increasingly complex and large precursor molecules with functional groups can offer interesting features as a result of newly accessible properties. A well-established method to allow high-resolution scanning probe microscopy (SPM) studies of such large and complex molecular structures on surfaces with the necessary cleanliness and reasonable control over the coverage is electrospray deposition (ESD). Thereby, molecular solution droplets are electrically accelerated towards surfaces in UHV through a differential pumping setup.

In this thesis, SPM studies of large two-dimensional supramolecular islands on surfaces in UHV, formed by ESD of already large, complex and functionalized molecules, are first performed to reveal specific responses to external stimuli and their tuning. In a second step, solution synthesized nanoribbons are deposited by ESD to investigate their novel and interesting structures and properties on even previously not accessible surfaces in UHV.

First, the influence of the deposition method on adsorption properties and surface morphology is evaluated in comparison to thermal evaporation in a model study with non-contact atomic force microscopy (nc-AFM). Then, the thermal response of molecular networks due to alkyl chains is investigated for a large spoked wheel (SW) molecule with nc-AFM at 300 K, scanning tunneling microscopy (STM) and CO functionalized AFM at 5 K. In combination with molecular dynamics (MD) simulations this reveals a mechanism of thermal expansion based on alkyl chain mobility. This mechanism is applied to tune the thermal response of hexabenzocoronene (HBC) based molecules equipped with different alkyl chain lengths. STM and nc-AFM imaging at 5 K, 77 K and 300 K unveil an inverse correlation of chain length and thermal expansion coefficient, shorter chains result in a higher expansion.

In a second part of this thesis, two solution synthesized graphene nanoribbons (GNRs) containing fragile moieties, alkyl chains, *tert*-butyl and methoxy edges, are investigated. Nc-AFM studies at room temperature demonstrate a significant influ-

ence of edge functionalization and structure. A planar and flat rigid structure is observed for a methoxy functionalized "cove"-type GNR, while a non-planar twisted and significantly more flexible structure is observed for the three-dimensionally designed fjord-GNR. Subsequent depositions of this GNR on non-metallic surfaces open high-resolution studies to fragile GNRs even on previously inaccessible surfaces and when annealing should be avoided.

Zusammenfassung

FUNKTIONALE Materialien, die durch Selbstanordnung von Molekülen auf Oberflächen im Ultrahochvakuum (UHV) gebildet werden, benötigen in geeigneter Form designte molekulare Bausteine mit komplexen Strukturen und funktionalen Gruppen. Die Möglichkeit solche Moleküle auf Oberflächen aufzubringen, bietet interessante neue Funktionen aufgrund ihrer möglichen neuen Eigenschaften. Eine fest etablierte Methode solche Moleküle mit der für hochauflösenden Rastersondenmikroskopie (SPM) Untersuchungen erforderlichen Reinheit und Kontrolle auf Oberflächen im UHV aufzubringen, ist die Elektrospray Deposition (ESD). Tröpfchen einer Moleküllösung werden durch das Anlegen einer elektrischer Spannung durch ein differenzielles Pumpsystem in Richtung der Oberfläche im UHV beschleunigt.

In dieser Dissertation werden hochauflösende SPM Untersuchungen auf zweidimensionalen supramolekularen Inseln, die auf Basis von großen, funktionalisierten Molekülen durch Aufbringen mit ESD gebildet wurden, durchgeführt. Dies zeigt spezifische Reaktionen auf externe Stimuli und erlaubt das Erkunden ihrer Regulierung. In einem zweiten Schritt wird die hochauflösende SPM Untersuchung von in Lösungsmittel synthetisierten Graphene Nanoribbons durch das Aufbringen via ESD auch auf bisher unerreichten Oberflächen ermöglicht. Zunächst wird der Einfluss von ESD auf die Adsorptionseigenschaften und Oberflächenmorphologie im Vergleich zur thermischen Verdampfung mit der Untersuchung eines Modellmoleküls durch Nichtkontakt-Rasterkraftmikroskopie (nc-AFM) beurteilt. Anschließend wird die thermische Reaktion molekularer Netzwerke ausgelöst durch Alkylketten für ein großes Speichenradmolekül (SW) mithilfe von nc-AFM bei 300 K und Rastertunnelmikroskopie (STM) bei 5 K untersucht. Basierend auf Molekulardynamiksimulationen werden die Mobilität und Fluktuationen der Alkylketten als zugrundeliegender Mechanismus erkannt.

Dieser Mechanismus wird dann zur Regulierung der thermischen Reaktion von Hexabenzocoronemolekülen (HBC) durch Veränderung der Alkylkettenlänge verwendet. STM und nc-AFM Untersuchungen bei 5 K, 77 K und 300 K offenbaren hier eine inversproportionale Korrelation zwischen Kettenlänge und thermischem Expansionskoeffizienten. Kürzere Ketten entsprechen einer größeren Expansion der Molekülnetzwerke.

Im zweiten Teil der Arbeit werden in Lösung synthetisierte Graphene Nanoribbons (GNR) mit fragilen Gruppen, wie Alkylketten oder *tert*-Butyl, untersucht. Nach dem Aufbringen durch ESD zeigen nc-AFM Untersuchungen einen starken Einfluss der Kantenstruktur und Funktionalität. Ein Methoxy-funktionalisiertes GNR zeigt dabei eine planare und flache Struktur, während ein dreidimensional designtes fjord-GNR eine verdrehte nicht-planare, deutlich flexiblere Struktur zeigt. Anschließende Depositionen auf nichtmetallischen Oberflächen eröffnen die Möglichkeit GNRs mit oder ohne fragilen Gruppen auf bisher nicht zugänglichen Oberflächen und auch ohne Annealing zu untersuchen.

Contents

Abstract & Zusammenfassung	v
Table of Contents	viii
List of Figures	xi
List of Tables	xv
Introduction	1
1 Experimental Principles:	3
1.1 Scanning Tunneling Microscopy	3
1.2 Non-contact Atomic Force Microscopy	4
1.2.1 Interaction Forces	6
1.3 Increasing and Stabilizing High-resolution	8
1.3.1 Multimodal AFM	8
1.3.2 Multipass AFM	9
1.4 Kelvin Probe Force Microscopy	11
1.5 Atomic Force Microscopy at Low Temperature	12
1.6 Summary	13
2 Experimental Realization and Methods	15
2.1 The Room Temperature Setup	15
2.1.1 The RT UHV Setup	15
2.1.2 The Microscope	17
2.1.3 Measurement Control	18
2.1.4 Cantilever Preparation	18
2.2 The Low Temperature Setup	19
2.2.1 The LT UHV Setup	19
2.2.2 The LT Microscope and Cryostat	20

Contents

2.2.3	Tip Preparation and Modification	21
2.2.4	Measurement Control	21
2.3	Surface Preparation	22
2.3.1	Preparation of Au(111) and Ag(111)	22
2.3.2	Preparation of KBr(001)	23
2.3.3	Preparation of HOPG	23
2.4	Summary	24
3	Electrospray Deposition	25
3.1	Molecular Deposition Methods	26
3.1.1	Alternative Deposition Methods	26
3.2	ESD Principle	27
3.3	ESD Setup	30
3.4	Examples of ESD of Molecules	32
3.5	Influence of ESD on Molecular Deposition	38
3.5.1	Influence of ESD on Metallic Surfaces	38
3.5.2	Influence of ESD on an Insulating Surface	40
3.5.3	Influence of ESD on a Semi-conducting Surface	43
3.6	Summary	44
4	Thermal Expansion by Alkyl Chain Motion	47
4.1	Thermal Expansion of Molecular Materials	47
4.2	Single Spoked Wheel Molecules	51
4.3	Molecular Assembly Thermal Response	52
4.4	Single Molecule Thermal Response	53
4.5	Thermal Expansion Mechanism	56
4.6	Summary	59
5	Tuning Thermal Expansion by Alkyl Chain Functionalization	61
5.1	Thermal Response of Alkyl Chain Functionalized HBCs	62
5.2	Thermal Expansion Dependent on Alkyl Chain Length and Substrate	64
5.3	Chain Length Influence on Temperature Dependent Molecular Surface Chirality	66
5.4	Phase Behavior upon Cooling of HBC-6C ₄ H ₉	67
5.5	Summary	69
6	Solution Synthesized Graphene Nanoribbons on Surfaces by ESD	71
6.1	Graphene Nanoribbons on Surfaces	72
6.1.1	On-surface Synthesis	72
6.1.2	Solution Synthesis	73
6.2	Methoxy-GNR	75
6.2.1	Adsorption of OMeGNR	75
6.2.2	Room Temperature Manipulation of Solution Synthesized GNR	78
6.3	Fjord-GNR	81
6.3.1	Fjord-trimer Precursor Molecule	81

6.3.2	Adsorption of FGNR	85
6.3.3	Non-planarity of FGNR	87
6.4	Solution Synthesized GNRs on Non-metallic Surfaces	88
6.5	Summary	92
Conclusion		93
Bibliography		97
Appendix		121
Nomenclature		124
Acknowledgments		127
List of Publications & Communications		129

List of Figures

1.1	Schematic representation of a STM	4
1.2	Schematic representation of a nc-AFM	5
1.3	Interaction forces	6
1.4	Oscillation modes	9
1.5	Multipass method	10
1.6	Schematic representation of a FM-KPFM	11
1.7	Schematic representation of a qPlus sensor	12
2.1	The RT UHV setup	16
2.2	The microscope	17
2.3	The cantilevers	19
2.4	The LT UHV setup	20
2.5	The qPlus sensor with tungsten tip	21
2.6	Ag(111) sample with atomic resolution	22
2.7	KBr(001) sample with atomic resolution	23
2.8	HOPG sample with atomic resolution	24
3.1	Function of the electrospray setup	28
3.2	Modes of the electrospray depending on voltage	29
3.3	Formation of gas-phase ions	30
3.4	Illustration of the electrospray setup	31
3.5	Electrospray deposition in vacuum	32
3.6	Electrospray deposition of C ₆₀	33
3.7	Electrospray deposition of carbon nanotubes	34
3.8	Electrospray deposition of polymers	34
3.9	Electrospray deposition of single-strand DNA	35
3.10	Electrospray deposition on bulk insulator KBr(001)	36
3.11	Electrospray deposition of dye molecules	37
3.12	Comparison of molecular deposition via thermal evaporation and ESD on Au(111)	39

List of Figures

3.13	Adsorption properties after ESD on Au(111) and Ag(111)	40
3.14	Comparison of molecular deposition via thermal evaporation and ESD on KBr(001)	41
3.15	Different coverage levels achieved by ESD	42
3.16	Comparison of molecular deposition via thermal evaporation and ESD on NiO(001)	44
4.1	Mechanisms of thermal expansion	48
4.2	Thermal expansion by conformational changes	49
4.3	Thermal expansion by geometric changes	49
4.4	Thermal expansion by guest-host interaction	50
4.5	Thermal expansion by molecular rearrangement	50
4.6	The spoked wheel molecule	51
4.7	Thermal response of a SW molecular assembly on Au(111)	53
4.8	Thermal response of SW core versus chains based on MD simulations .	54
4.9	Thermal response of a single SW molecule	55
4.10	Building a SW trimer assembly for MD simulations from an experimental assembly	57
4.11	Thermal response of the SW trimer by chain mobility	58
5.1	Structure of alkyl chain functionalized HBCs	62
5.2	Thermal response of alkyl chain functionalized HBCs	63
5.3	Thermal expansion dependent on alkyl chain length and substrate . . .	66
5.4	Illustration of temperature dependent molecular surface chirality	67
5.5	Phase response of HBC-6C ₄ H ₉ dependent on temperature	68
6.1	Structure of the GNR molecules	71
6.2	Schematic illustration of on-surface synthesis	72
6.3	Schematic illustration of the solution synthesis of GNRs	74
6.4	Schematic illustration of the synthesis of non-planar GNR	74
6.5	OMeGNR on Au(111)	76
6.6	Single OMeGNR on Au(111)	76
6.7	Two lobe structure of a "cove"-type GNR	77
6.8	Tip induced manipulation of OMeGNR on Au(111)	79
6.9	Large scale tip induced manipulation of OMeGNR on Au(111)	80
6.10	f-trimer on Au(111)	81
6.11	Adsorption of f-trimer	82
6.12	On-surface reaction of f-trimers	83
6.13	FGNR on Au(111)	85
6.14	Single FGNR on Au(111)	86
6.15	Non-planarity of FGNR	87
6.16	FGNR on KBr(001)	89
6.17	Single FGNR on KBr(001)	89
6.18	Submolecular resolution of a FGNR assembly on KBr(001)	90
6.19	FGNR on HOPG	91

A.1	Alkyl chain fragments of a "cove"-type GNR with high alkyl chain functionalization.	121
A.2	C ₆₀ -4C ₁₂ H ₂₅ molecule assemblies deposited by ESD	122
A.3	DBOV-TDOP molecule assemblies after ESD	122

List of Tables

5.1	Coefficients of thermal expansion of 2D molecular assemblies.	65
-----	---	----

Introduction

FUNCTIONAL materials formed by molecules, polymers or their assemblies provide intriguing new opportunities in mechanical, optical, electronic or biological applications [1–4]. For example novel approaches for sensors and non-linear optics, the formation of artificial muscles or flexible biocompatible devices or highly-stable materials for aerospace applications can be facilitated [5–10].

At the nanoscale the build-up of assemblies of rationally designed molecular structures can lead to such materials [1–3]. More complex and increasingly larger building block molecules possibly including specific functional groups, facilitated by progresses in synthetic chemistry, can allow the investigation of novel functions and material properties on surfaces [11–13]. Access to a large variety of such molecules can be afforded by electrospray deposition (ESD).

It is well-established for large and complex molecules, especially for biological uses, in mass spectrometry and more recently extended to many molecules for nanosciences and surface science [14–22]. Based on the electrospray ionization method (ESI), a droplet jet is accelerated by high voltage through a differential pumping setup towards the surfaces in UHV [14–18]. With sufficient solubility of molecules ESD can offer high cleanliness and reasonable control over molecular coverage for various molecules ranging from small molecules to large and complex molecules, polymers or ribbons [17–35]. The only limitation on possible depositions, thereby, is the solubility of the species.

This work focuses on scanning probe microscopy (SPM) studies of the structures and functional properties of two-dimensional (2D) supramolecular assemblies formed by the deposition of already large and complex functional molecules and, in a second step, on studying extended solution synthesized graphene nanoribbons accessed via ESD.

In the first Chapter 1, the principles of the experimental tools employed for this study are described. The theoretical background of non-contact atomic force microscopy (nc-AFM) and scanning tunneling microscopy (STM) and improvements to enhance the resolution at room temperature (RT) are introduced, including multimodal and

multipass techniques.

Thereupon, the experimental realization of the techniques with their experimental setups, methods and materials are established in Chapter 2. The UHV setups, preparation, and measurement control systems are explained along with the materials and methods used.

In Chapter 3, the electrospray deposition method, chosen to access the functional molecules on surfaces, is introduced after an in-depth discussion of deposition methods and their limitations. Previous uses of ESD for molecular depositions are summarized and their influence on molecular adsorption and surface morphology evaluated in comparison to thermal evaporation (TE) with a study performed on a model molecule on three different surfaces. Especially, the spray deposition influence on the formation of buckminster fullerene (C_{60}) assemblies is compared to TE.

The next two chapters are dedicated to accessing the functionalities provided by alkyl chains in molecular networks. In Chapter 4 the thermal response of two-dimensional supramolecular networks based on alkyl chain functionalization is studied on a shape-persistent polyphenylene spoked wheel molecule (SW). First, a discussion of thermal expansion in molecules and assemblies is presented. Subsequent high-resolution low temperature (LT) STM and nc-AFM studies at 5 K and 300 K reveal a giant thermal expansion of molecular assemblies. With molecular dynamics (MD) simulations the observed thermal response is attributed to a supramolecular mechanism based on alkyl chain mobility forcing network expansion. In the following Chapter 5, this mechanism is applied to investigate tuning possibilities of the thermal response of molecular assemblies. By studying the thermal expansion of three hexabenzocoronene (HBC) molecules equipped with three different lengths of alkyl chains with STM and nc-AFM at 5 K and 300 K, an inversely proportional dependence between thermal expansion and length of the side chains is found. Shorter alkyl chains result in an increased expansion with temperature.

Chapter 6 covers the deposition and high-resolution study of solution synthesized graphene nanoribbons (GNRs) containing fragile moieties and novel edge and ribbon structures. The advantages and limitations of the state-of-the art on-surface synthesis method and solution based synthesis are compared. Thereupon, two GNRs containing fragile groups and promising edge and ribbons structures are deposited and their properties studied with nc-AFM at RT. Two distinctly different structures are found for a methoxy functionalized "cove"-type GNR (OMeGNR) equipped with alkyl chains and a fjord-edged GNR (FGNR) with *tert*-butyl groups. While the OMeGNR shows a rigid planar structure adsorbed on the surface, the FGNR exhibits high flexibility along with a twisted non-planar structure. Based on studies of a model precursor, the twist is attributed to steric hindrance of the *tert*-butyl groups in the fjord-edges and on-surface reaction evaluated. Lastly, the FGNRs are also deposited on bulk insulator potassium bromide (KBr(001)) and semi-metal highly oriented pyrolytic graphite (HOPG) opening the possibility of studies of solution synthesized GNRs with fragile structures even to those and further surfaces without the need for any post-deposition annealing or procedures.

Experimental Principles:

NANOSCALE investigations of molecules on surfaces in real space are facilitated by scanning probe microscopy, a reliable and powerful class of techniques based on scanning a physical sensor - the probe - over the surface of the sample. With SPM atomic resolution has been achieved on a variety of surfaces after its invention in 1981 by Binnig *et al.* [36] and the first atomic structure resolution of the Si(111)-(7×7) reconstruction in 1983 [37]. A variety of environments is accessible with SPM with atomic resolution achieved in air [38, 39], at the liquid solid interface [40] and in UHV. Biological applications became accessible with amplitude modulation (AM) AFM mostly operated in tapping mode [41, 42]. Thanks to further developments like multimodal AFM [43], multipass imaging [44], Kelvin probe force microscopy [45] or the qPlus sensor [46] and CO functionalization [47], SPM techniques still present the most powerful characterization methods for surfaces and adsorbed molecules, even down to single bonds or atoms. In this chapter various scanning probe methods and specific scanning modes relevant to this work are introduced.

1.1 Scanning Tunneling Microscopy

Scanning tunneling microscopy (STM), developed by Binnig and Rohrer in 1981 [36], is based on the quantum tunneling effect. Due to the non-zero probability of electrons to tunnel through a potential barrier between two electrodes, a current arises when bringing a probing tip in close proximity to the surface of a conductive sample and applying a bias voltage V_{Bias} . This tunneling current I_t exponentially depends on the distance between tip and sample. In a STM, the tunneling current is used in two distinct ways to gain insight into the morphology of the surface. Generally, the probing tip is brought into close proximity of the surface of the desired sample and a bias voltage is applied, resulting in a tunneling current flow. Then, the dependence is applied to control the tip-sample distance by adjusting the tip height to keep the current constant while scanning over the surface (constant-current mode). The recording of the height adjustments is converted into a map of the topography. Alternatively, the tip is moved

Chapter 1. Experimental Principles:

at a constant height during the whole scan and the current is recorded. A map of the current, then, provides a representation of the surface. In this work, constant-current mode was used exclusively with the schematic setup of a STM shown in Figure 1.1.

Due to the high resolution achievable with STM, it has become an exceptional tool for studying conductive surfaces. Which also indicates its biggest limitation, non-conductive surfaces can generally not be investigated with STM. A large class of experiments for example insulators and many biological applications are, thus, not accessible to it. Partial decoupling of molecules and their molecular orbitals from the surface, while still allowing tunneling, can be achieved by deposition of monolayers of insulating ionic crystals [48, 49].

For an optimal measurement of the tunneling current and to avoid imaging artifacts from multiple current flows, the tip should ideally be terminated by a single atom. With the tungsten tips frequently used for UHV studies this can be accomplished by indenting the tip into a clean patch of the surface and retracting outwards to form the desired sharp apex based on the surface material.

A significant improvement of the STM resolution at low temperature, first applied by Gross *et al.* in 2009 [47], is the functionalization of the tip apex with a CO molecule. For this CO is dosed onto the surface and CO either spontaneously adsorbed to the tip apex or picked up by approaching towards it. Imaging with a CO terminated tip allows significantly increased resolution, with bond level imaging achieved by constant height atomic force microscopy, as described in Section 1.5 [50–52].

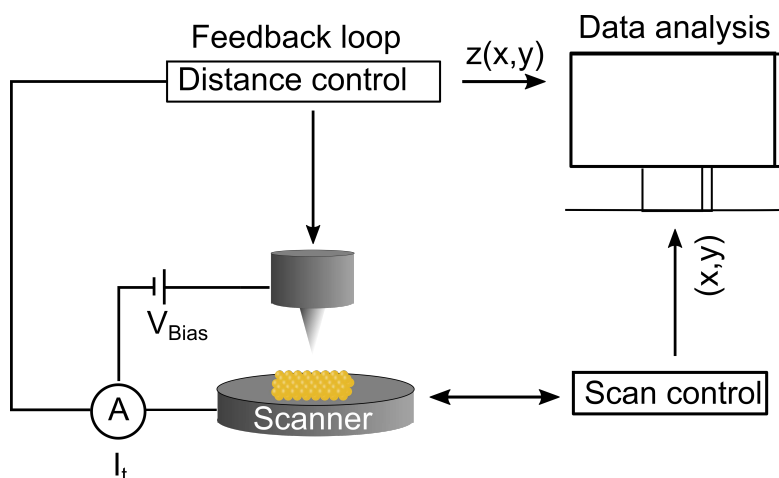


Figure 1.1: Schematic representation of a STM. The tunneling current arising with the bias voltage V_{Bias} is kept constant by adjusting the tip-sample distance via a feedback loop (constant current mode). The resulting map provides the surface topography.

1.2 Non-contact Atomic Force Microscopy

The development of the atomic force microscope in 1986 [53], in its first iterations based on measuring the deflection of a probe by STM, opened up new possibilities in

1.2. Non-contact Atomic Force Microscopy

surface science. Now, SPM was no longer limited to conductive surfaces and atomic resolution became accessible on insulating surfaces.

AFM, like STM, is based on bringing a probe, most often a sharp tip mounted on a cantilever, close to or in contact with a surface. The deflection of the cantilever due to the interaction forces F_{int} is measured and converted to the signal. Depending on the measurement mode topography and different additional signals are considered, like excitation for energy dissipation [54–56].

Non-contact AFM was first presented by Albrecht *et al.* in 1991 [57] and enjoys great success in surface science in UHV, with the first atomic resolution images on Si achieved in 1995 [58–60].

The working principle of nc-AFM, schematically shown in Figure 1.2, is based on exciting the cantilever at the resonance frequency of its undisturbed flexural oscillation mode, i.e. far from the surface. The amplitude is, thereby, kept constant by adjusting the excitation. The tip is, then, approached into close proximity of the surface. Resulting interaction forces modify the oscillation frequency of the cantilever, a frequency shift is observed in respect to the free resonance. Using a feedback loop this frequency shift is kept constant, via the regulation of the tip-sample distance, resulting in a topographic map.

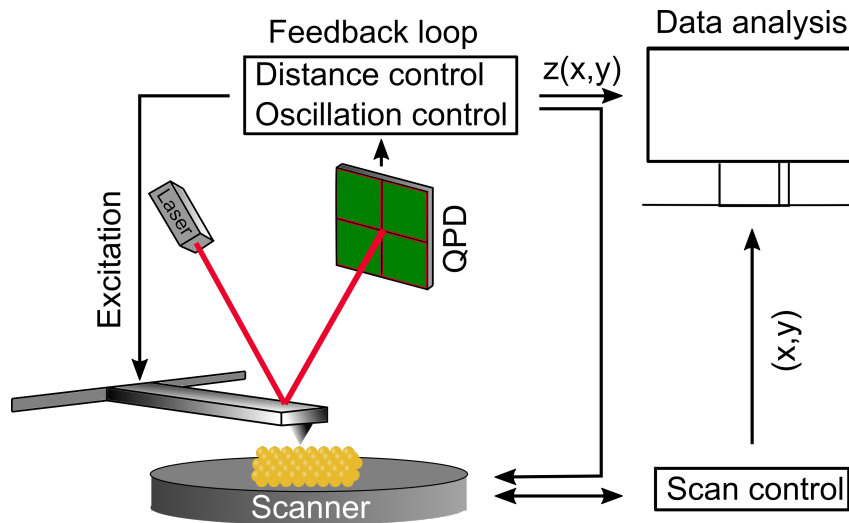


Figure 1.2: Schematic representation of a nc-AFM. In nc-AFM the frequency shift due to tip-sample interaction is regulated to be constant by adjusting the tip-sample distance to obtain a topographic representation of the surface.

The detection in nc-AFM is generally achieved by reflecting a laser of the back of the cantilever onto a quadrant photo diode (QPD). The detected signal is transferred to a phase-locked loop (PLL), where amplitude and phase shift are regulated, with the excitation adjusted to keep the oscillation amplitude constant, revealing energy dissipation over the surface [56].

1.2.1 Interaction Forces

As introduced above, when approaching the sample, the oscillating cantilever experiences a sum of forces, leading to a shift in oscillation frequency. This force consists of long- or short-range contributions from different forces, exhibiting different influence depending on distance. For nc-AFM in UHV the main contributing forces are first the long-range electrostatic F_{el} observed up to a tip-sample distance of 100 nm, second, the van der Waals (vdW) interaction force F_{vdW} , also up to 100 nm and last, the short-range chemical forces F_{chem} [61, 62].

The contributions of the described forces and the resulting total force acting on the cantilever dependent on tip-sample distance are visualized in Figure 1.3. During the approach the cantilever first experiences attractive forces, dominated by the electrostatic and vdW interactions, on closer approach to below 500 pm the contribution of these forces diminishes and chemical forces dominate [62, 63]. It is in this regime, where atomic resolution can be obtained.

On further approach the cantilever experiences a repulsive force. Of note is the non-monotonic behavior of the total force. Since the feedback signal, the frequency shift, depends on the total force, a stable feedback for nc-AFM is only possible in the attractive regime.

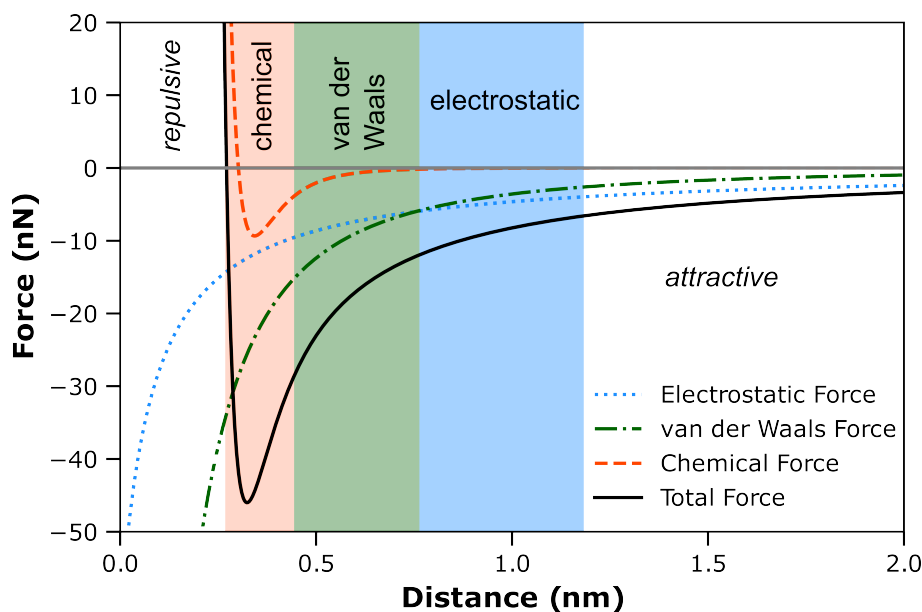


Figure 1.3: Interaction forces. *Tip-sample interaction forces typically arising on approaching a surface as function of the distance (z). Atomic resolution can be achieved by optimizing the sensitivity to the chemical force regime by adjusting tip-sample distance and oscillation properties.*

The electrostatic forces F_{el} acting on the cantilever arise without the presence of an external bias or trapped charges due to the difference in work function Φ of the tip and sample materials $\Delta\Phi = \Phi_{Sample} - \Phi_{Tip}$. Generally, F_{el} can be expressed by the gradient of the capacitance C and the potential difference between tip and sample [64]:

1.2. Non-contact Atomic Force Microscopy

$$F_{el} = \frac{1}{2} \frac{\partial C}{\partial z} V^2, \quad (1.1)$$

where V is the potential difference between tip and sample.

When considering a spherical tip with radius r at height of z over an infinite plate acting as capacitor this can be simplified to:

$$F_{el} = -\pi\epsilon_0 \frac{r^2}{z(z+r)} V^2, \quad (1.2)$$

with the vacuum permittivity ϵ_0 [65].

By applying a specific bias voltage V_{Bias} to the sample so that the potential difference $V \approx 0$, the influence of the electrostatic force can be minimized. The necessary bias voltage is given by the potential difference as follows:

$$V = V_{Bias} - \frac{\Delta\Phi}{e}, \quad (1.3)$$

where $\frac{\Delta\Phi}{e}$ with the elementary charge e is also known as the contact potential difference V_{CPD} (CPD). The average CPD can for homogeneous surfaces be compensated by a constant bias applied once before a scan by sweeping the bias and recording the corresponding frequency shift. By adjusting the bias to the maximum value of the parabola – the minimum of the absolute value of frequency shift – the force can be compensated locally. For surfaces with non-uniform potential differences, the compensation should be repeated for each area. A continuous compensation is also possible for each point of the scan by applying Kelvin probe force microscopy (KPFM) [66, 67]. A continuous adjustment of the bias voltage is desirable, when the work function of the surface is not homogeneous, i.e. the surface consists of different materials, shows non uniform surface potential or is modified by adsorbed molecules or atoms [68–70]. The working principle and implementation of KPFM are discussed in the Sections 1.4 below.

In contrast, no minimization is possible for the forces arising from van der Waals interactions during measurements. vdW forces arise from interactions between neutral atoms or molecules, here especially of tip and sample.

Again considering a spherical tip and an infinite plate, the vdW forces can be described as:

$$F_{VdW} = -A_H \frac{r}{6z^2}, \quad (1.4)$$

with the tip radius r and the Hamaker constant A_H , which describes the vdW interaction between two particles [71–73].

As can be seen from Equation 1.4 the only possible reduction of the vdW forces is the use of very sharp tips, which during a scan, especially at room temperature, can not be guaranteed due to pick up of material and resulting modification of the radius of the tip apex.

To obtain atomic resolution, one has to sense in the short-range regime, where chemical forces become dominant [56]. The tip apex atoms interaction with surface/molecule

atoms forming temporary bonds [63,74,75] responsible for the chemical interaction can, thereby, generally be described by a pair-wise Leonard-Jones [76].

$$F_{chem,LJ} = -12 \frac{E_{Bond}}{\sigma} \left[2 \left(\frac{\sigma}{z} \right)^7 - \left(\frac{\sigma}{z} \right)^{13} \right], \quad (1.5)$$

where E_{Bond} is the bond energy and σ the equilibrium distance.

The interaction can also be described by the Morse potential in terms of the exponential decay of the bonding [77]:

$$F_{chem,Morse} = -E_{bond} (2e^{-\kappa(z-\sigma)} - e^{-2\kappa(z-\sigma)}), \quad (1.6)$$

with the decay length κ .

1.3 Increasing and Stabilizing High-resolution

Sensing chemical forces being difficult, when only using the first flexural resonance in nc-AFM, several methods to improve the imaging resolution and stability to obtain reliable atomic or submolecular resolution, like multimodal imaging, higher resonances or multipass imaging, are employed to increase the time present in this force regime. The methods relevant to this work are described in the following.

1.3.1 Multimodal AFM

An important increase in resolution can be achieved by simultaneous to the flexural resonances, whose frequency shift is used for the tip-sample distance regulation, also exciting the cantilever to further resonance modes. By superimposing an additional excitation signal to the drive signal, this enables the use of so called multimodal AFM [43,78–84]. In theory, an unlimited number of modes, including higher flexural resonances, torsional modes or shearing modes, could be envisioned, limited only by the setup and possibly the scan stability. The additional modes provide access to the measurement of further interaction signals simultaneously or in addition to the topographic and dissipative information obtained from the flexural mode [55]. A selection of commonly used resonances in nc-AFM is shown in Figure 1.4a.

The mode superimposed during this work is the torsional resonance. It is especially sensitive to short-range lateral forces, since its oscillation amplitude is generally less than 100 pm and its frequency shift, thus, is directly dependent on the short-range lateral forces [43,80,81,85]. This can allow submolecular or atomic contrast, which could not be achieved from the topographic image. The enhanced sensitivity works best for periodic structures with a high symmetry since the local force gradient can otherwise lead to complicated imaging contrasts, which often limits the use on molecules. An example of a well suited molecule is presented in Figures 1.4b and c, where a nc-AFM topography and the corresponding torsional frequency shift image of fjord-trimers (f-trimers), described in Section 6.3.1, are visible. The topography already shows lines of dimeric structures, formed by two curved molecules of different heights with a small opening in them. This periodic arrangement of the molecules allows for an

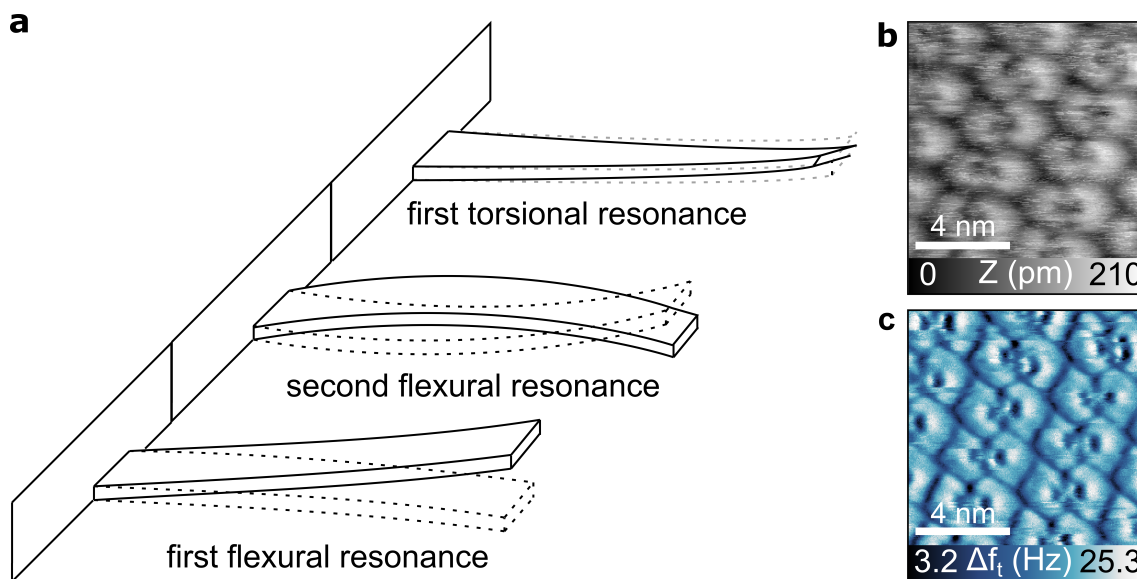


Figure 1.4: Oscillation modes. **a**, Oscillations typically excited during this work. Left to right, first flexural resonance f_1 , second flexural resonance f_2 , and first torsional resonance f_t . Multiple resonances can be excited simultaneously. **b**, **c**, nc-AFM topography and torsional frequency shift image of fjord-trimer precursor molecules on Ag(111) illustrating the benefits of simultaneous excitation of multiple modes ($A_2 = 600$ pm, $\Delta f_2 = -13$ Hz, $A_t = 80$ pm).

even higher resolution in the torsional frequency shift image below. There, in addition to the double structure also the trapezoid shape of the molecules along with the fjord shaped opening in the molecule is well resolved, allowing precise investigation of the adsorption and interaction of the molecules. Noticeably, however, the height resolution is diminished, both dimers show very similar frequency shift values.

The second flexural mode can not only be superimposed but also be used for tip-sample distance regulation [79, 82]. In comparison to the first flexural resonance, the stiffness is increased by a factor of 40, allowing smaller oscillation amplitudes while still maintaining stable scan conditions [83]. Thereby, amplitudes between 1.2 nm and 200 pm can generally be achieved. While the smaller amplitude will not bring the tip as close to the surface at maximum, limiting damaging of the sample [79], the tip on average will remain in closer proximity of the sample. As a consequence the sensitivity to short-range forces is increased, allowing an enhancement of the contrast.

1.3.2 Multipass AFM

Additional improvement of stable scan conditions can be obtained by applying the multipass technique, first developed by Moreno *et al.* in 2015 [50] at temperatures below 80 K. Recently, it has also been applied at room temperature with significant success [86, 87]. It addresses the limitation of the tip-sample distance regulation due to the non-monotonic behavior of the $\Delta f(z)$ curve by imaging without the distance controller active. This allows entering the repulsive regime, where submolecular features can be

Chapter 1. Experimental Principles:

resolved thanks to Pauli repulsion [44, 47].

The principle of the multipass method is scanning each line twice, as illustrated in Figure 1.5a. While constant height imaging could achieve similar results and is most often performed at LT, as described in the following Section 1.5, the stability, thermal drift and especially the height of molecules necessitate taking into account the topography at RT. This is achieved in the first pass, where the topography is recorded in stable imaging conditions with the distance controller active. Then, a second pass of the same line is performed, but the distance controller is switched off. Instead, the recorded topography is replayed and followed with a constant z -offset of hundreds of picometers applied towards the surface and the ensuing frequency shift is measured. By repeating this for every line in the scan limitations due to thermal drift are minimized and even molecules with a significant 3D structure can be imaged with up to submolecular resolution [88]. This is visualized in Figures 1.5b and c, where a topographic image, the first pass, and the corresponding second pass frequency shift Δf_{2nd} image of a hexabenzocoronene molecule (HBC- $6C_4H_9$) network, introduced in Chapter 5, on an Ag(111) surface is shown. While in the topography image a network of hexagonal protrusions is visible, each corresponding to one molecule, the second pass frequency shift image reveals not only the molecule core, the protrusion, but also resolves pairs of interdigitated alkyl chains, which stabilize the network by vdW interaction, as submolecular features.

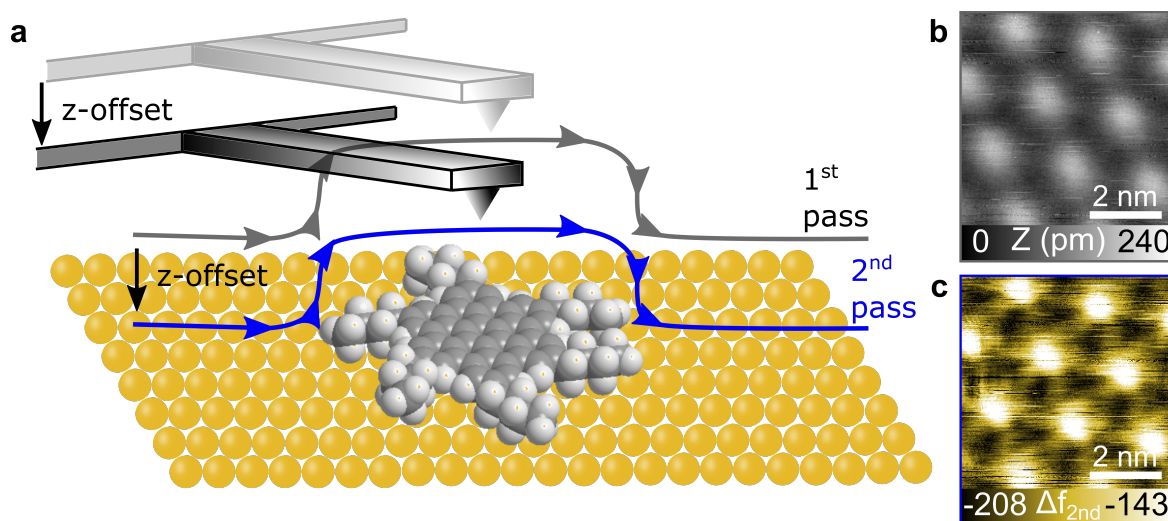


Figure 1.5: Multipass method. *a*, Schematic illustration of multipass technique. *b*, Topographic image of HBC- $6C_4H_9$ molecules acquired during the forward scan of the first pass (gray) ($A_2 = 400$ pm, $\Delta f_2 = -100$ Hz). *c*, Corresponding frequency shift image acquired in the second pass (blue) by replaying the topography with an offset $z_{offset} = -100$ pm towards the surface, showing submolecular contrast.

Even at LT during standard STM scans multipass can provide interesting possibilities e.g. measuring the local density of states directly during the scan with the second pass [89].

1.4 Kelvin Probe Force Microscopy

To reveal local modulation of the work function, as mentioned in Section 1.2.1, the CPD and, thus, the electrostatic forces, can be compensated locally, but also continuously for each point of the scan by KPFM. The basic principle, thereby, is the same as for local compensation. The actual implementation, first reported at the nanoscale in 1991 [45,90], is based on modulating the cantilever motion by applying an AC voltage V_{AC} with the frequency ω_{AC} . The electrical interaction forces then become:

$$F_{el} = \frac{1}{2} \frac{\partial C}{\partial z} [V_{DC} - V_{CPD} + V_{AC} \cos(\omega_{AC} t)]^2. \quad (1.7)$$

Thereby, oscillations at ω and 2ω are additionally excited on the cantilever. At ω the amplitude depends on the uncompensated part of the potential difference $V_{DC} - V_{CPD}$. In AM-KPFM this additional oscillation amplitude is measured very sensitively at the second resonance and by adjusting V_{DC} to equal V_{CPD} via a feedback loop set to zero [66,67,91]. The applied V_{DC} values over the scan can with a well-calibrated tip provide a map of the work function of the sample.

KPFM can also be performed in frequency modulation (FM) mode, FM-KPFM, which in contrast to the force compensation of AM-KPFM relies on the force gradient [65,92–94]. Here, a quite low AC frequency ($\omega_{AC} \approx 1$ kHz) is applied resulting in a modulation of the frequency shift of the flexural resonance of the cantilever. This modulation is, as shown in Figure 1.6, tracked by a lock-in and its amplitude used as a feedback signal in a Kelvin controller to compensate the electrostatic forces.

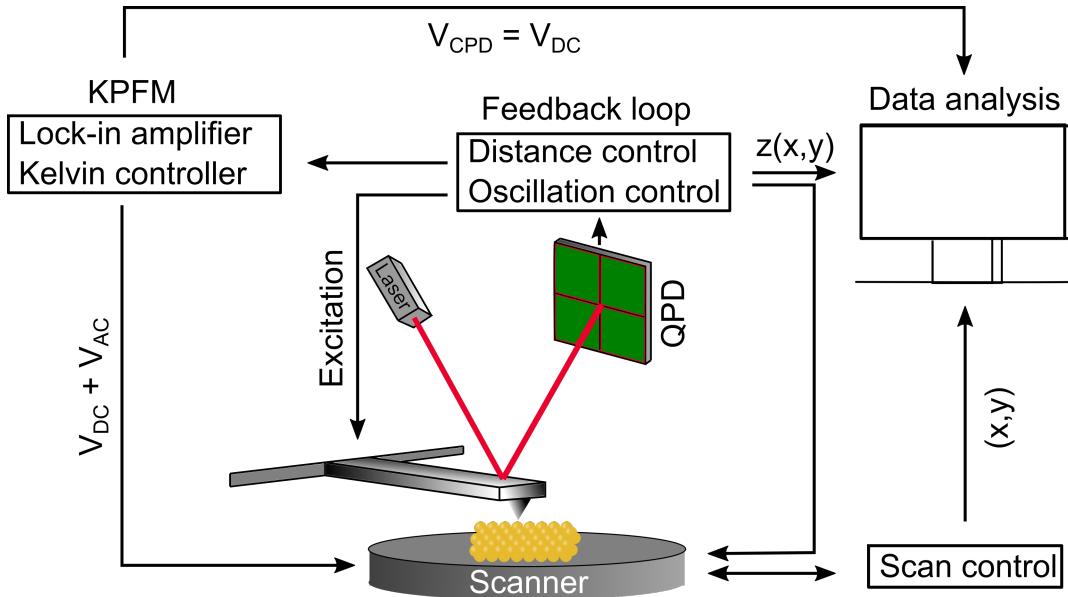


Figure 1.6: Schematic representation of a FM-KPFM. The AC voltage V_{AC} induces a modulation of the frequency shift Δf . This is used to compensate the electrostatic forces by adjusting V_{DC} to equal V_{CPD} via a feedback loop.

The absolute value of the CPD depends on the work function of tip and, thus,

the observed CPD can vary slightly between scans depending on tip modification. However, the observed CPD difference remains preserved.

1.5 Atomic Force Microscopy at Low Temperature

The most common configuration to acquire nc-AFM at LT is using qPlus sensors, allowing both STM and FM-AFM measurements [95]. The qPlus sensor is based on a tuning fork, where one prong is glued to an actuator and, thus, immobilized. The second prong is equipped with a conductive tip and can freely oscillate. Connected is a current to voltage (I-V) converter which allows detection of the deflection. A schematic illustration of a qPlus sensor is provided in Figure 1.7.

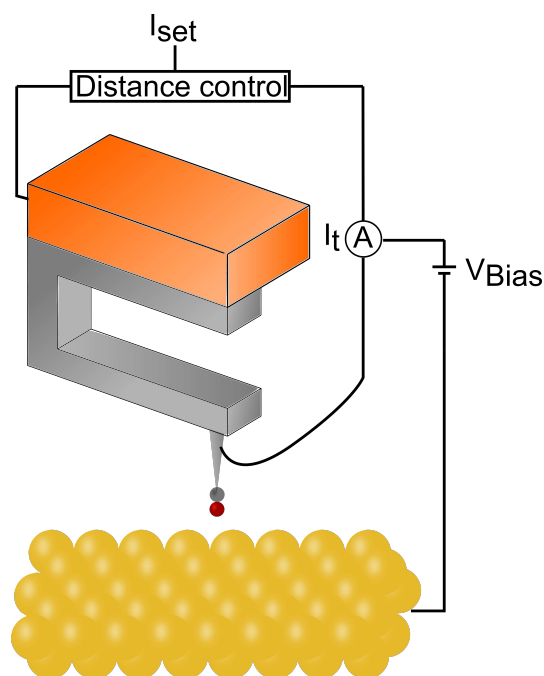


Figure 1.7: Schematic representation of a qPlus sensor. A sharp tip is fixed to one prong of a tuning fork, while the other is fixed to a mount on an actuator. The applied bias voltage and resulting tunneling current allow distance control.

AFM measurements with a qPlus sensor are mainly performed in constant height mode recording the frequency shift. This allows measuring in the repulsive regime with submolecular resolution down to the single bond level, especially when combined with tip functionalization [44,47,96]. The most common functionalization is adsorbing a CO molecule to the apex of the tip [97]. This allowed bond level contrast, achieved by Gross *et al.* in 2009 [47]. The CO molecule is inert and can, thus, be approached closely to the surface without forming temporary bonds to the surface. Thereby, the short-range Pauli repulsion can be measured with higher precision than other functionalizations, like for example Xe atoms [98].

1.6 Summary

In this chapter the principles of the SPM techniques employed for the studies performed during this work were introduced. The high resolutions, down to submolecular and atomic or even bond level, of STM and nc-AFM were discussed along with the methods and improvements facilitating them. This included the modification of the tip with single molecules at LT and the associated constant height measurement, and important scanning modes and compensation methods at RT with nc-AFM. Notably, multimodal AFM, higher resonances, multipass imaging, and the compensation of electrostatic forces, either locally or continuously by KPFM, were introduced.

Experimental Realization and Methods

THE experimental realization of the investigation and preparation of samples and the specific components necessary for the desired resolution are introduced in the following sections. Since in this work the study of molecules and surfaces without outside influences to achieve insights into their structure and fundamental properties is desired, all investigations presented in this thesis are performed under UHV conditions.

For this two distinct UHV systems were chosen. Most of the work was performed in the RT setup presented in Section 2.1 with the home-built microscope introduced thereafter along with its measurement control system. Then, the preparation of the cantilevers used as sensors is described. Subsequently, the second system, a LT UHV STM/AFM setup equipped with a qPlus sensor cooled either to 4.7 K or 77 K is introduced in Section 2.2.

Finally, the preparation of the different samples used in this work is explained.

2.1 The Room Temperature Setup

2.1.1 The RT UHV Setup

Room temperature measurements presented and discussed in this thesis are exclusively performed under UHV conditions. The preparation of samples are largely also performed in UHV, when applicable, while for some molecule depositions high-vacuum conditions are maintained. The setup necessary to achieve this consists of three chambers, the analysis, the preparation and the load-lock chamber, separated by gate valves and is shown in Figure 2.1. The analysis chamber (dark red) contains the microscope and the sample/cantilever storage carousel as well as a wobble stick for transferring between microscope and carousel or to the preparation chamber. A small ion getter pump fixed close to the microscope maintains the pressure in the analysis chamber below 10^{-8} mbar. To improve the base pressure, the gate valve separating analysis and preparation chambers (turquoise in Figure 2.1) is generally kept open to benefit from the turbo-molecular pump along with its prevacuum pump, the large ion getter pump

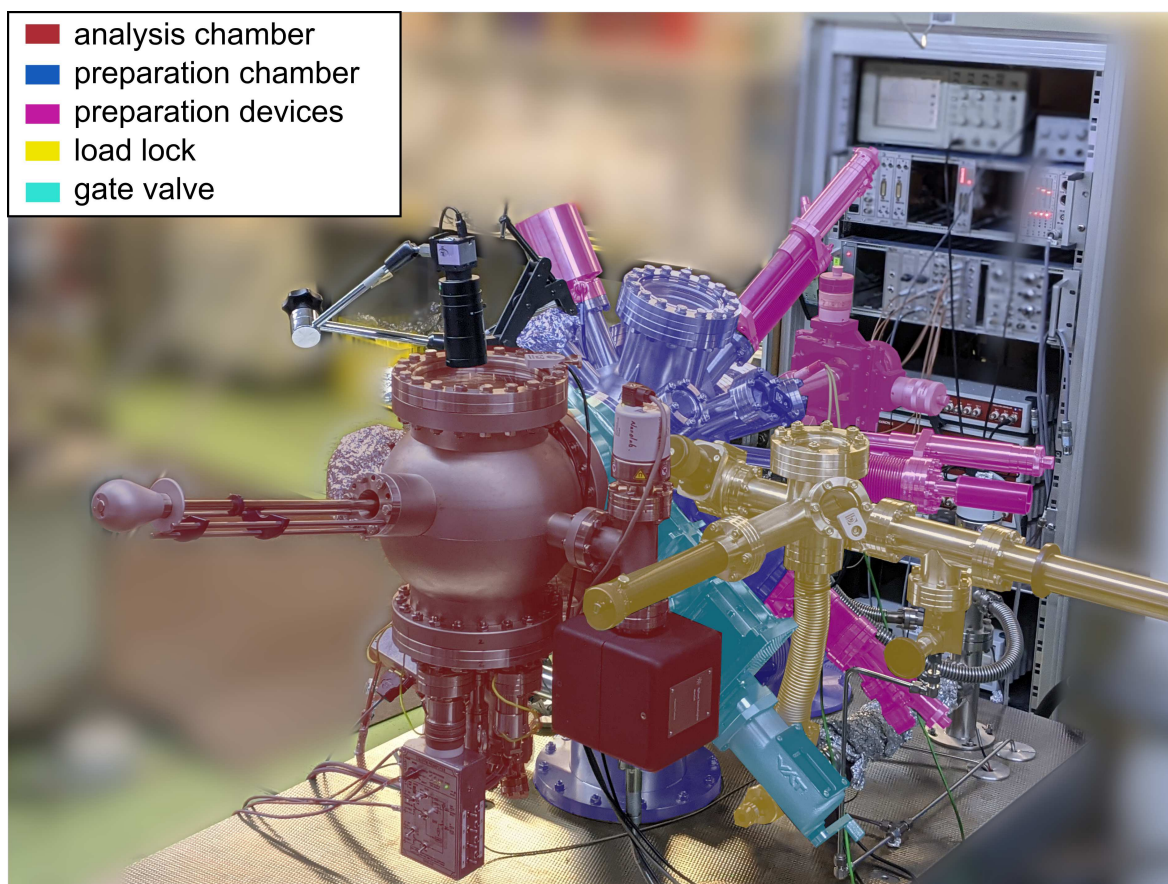


Figure 2.1: The RT UHV setup. *The two main chambers, analysis chamber (dark red) and preparation chamber (blue) with various devices (pink) are separated by a gate valve (turquoise). Visible in yellow is the load-lock, in the background the measurement control rack.*

and titanium sublimation pump (TSP) of the preparation chamber, allowing a vacuum base pressure of $\sim 10^{-10}$ mbar. The turbo-molecular pump can be closed off from the system with a pneumatic valve equipped with an emergency closing mechanism.

The preparation chamber (blue in Figure 2.1) contains a manipulator equipped with a heater, a sputter gun with an UHV leak valve, a Knudsen cell molecule evaporator, a quartz-micro-balance (QMB), a sample cleaver and an additional valve to the outside. There, the electro-spray deposition setup, described in Chapter 3, or a vacuum suitcase can be connected for transferring samples between different systems under UHV conditions.

Sample and cantilever transfer in and out of the setup is achieved via the load-lock chamber (yellow in Figure 2.1). It contains a transfer cane and a three sample/cantilever storage and is pumped by a separate turbo-molecular and prevacuum pump allowing it to reach a base pressure of $\sim 10^{-8}$ mbar within a reasonable time frame. The load-lock pumps can additionally be connected to the molecule evaporator for replacement of molecules and to a pumping stage for attaching an UHV suitcase.

The whole setup is maintained on top of two units of damping feet pairs by *The*

2.1. The Room Temperature Setup

Table Stable Ltd. to minimize outside vibrations and achieve high signal to noise ratios.

2.1.2 The Microscope

The room temperature measurements obtained in this work are exclusively performed with a home-built microscope designed and developed at the University of Basel [99].

The microscope allows nc-AFM and friction force measurements with an optical detection in cantilever setup. It is shown in Figure 2.2.

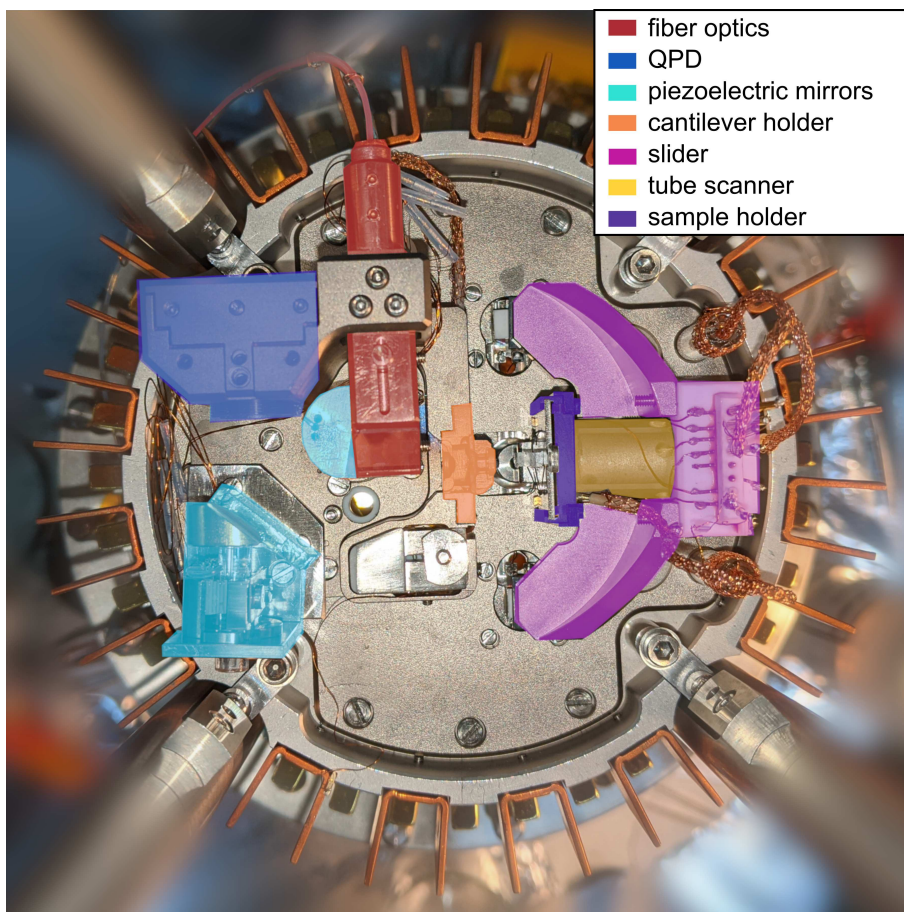


Figure 2.2: The microscope. Overview of the RT UHV AFM/STM consisting of the fiber optics (red), cantilever holder (orange), two piezoelectric mirrors (turquoise), a QPD (blue) and a slider (violet) carrying a tube scanner (yellow) and sample holder (dark blue).

All parts are mounted on a plateau isolated from external vibrations with springs and an eddy current damping system. It consists of the aforementioned optical detection setup, a cantilever holder (orange), and a slider (violet) containing the sample holder (dark blue) mounted to the tube scanner (yellow). The detection setup consists of an optical fiber (red), two piezo-driven mirrors (turquoise) and a quadrant photo diode detector (QPD) (blue). Mounted to the back of the QPD is an I-V converter for direct conversion of the signal to voltage to maintain a high 3 MHz bandwidth by avoiding

high capacitances of long cables or connections [99]. The optical fiber is connected on one side to a superlum diode (SLD), where the light with a wavelength of 678.5 nm is generated, and on the other side to the focus setup inside the UHV chamber. There, a set of lenses and mirrors aligns and focuses the beam onto a mirror. With help of this piezo-driven cylindrical first mirror the laser beam is positioned at the front end of the cantilever beam as much as possible. From the cantilever the beam is deflected towards a second mirror, which reflects it onto the QPD. Again applying piezo excitation the mirror is adjusted to center the laser spot on the QPD. For most measurements, the second mirror differed from the cylindrical first mirror as a spherical mirror, but was later replaced by a mirror that was also cylindrical. The setup shown is the final configuration.

On the detector, the motion of the beam is converted into four photocurrents by the four quadrants. As mentioned above, the currents are directly converted into voltages by the I–V converter behind the QPD. From there they are transferred to the electronics, where they are used to regulate the oscillations and tip–sample distance resulting in the topographic and other signals, like excitation.

2.1.3 Measurement Control

The control of the measurements is realized with a Nanonis RC4.5 electronics from *SPECS Zurich GmbH*, consisting of a real-time controller computer, a signal conditioning system, and two PLLs and the corresponding measurement software.

The two PLLs help realize the bimodal imaging mode, explained in Section 1.3.1. Thereby, the first PLL excites the cantilever to two oscillations, as discussed above the first or second flexural and the torsional resonance. This is achieved by superimposing an additional excitation signal at the torsional resonance frequency, generated and controlled by the second PLL, to the excitation of the first. The ensuing cantilever oscillations are detected by the QPD and transmitted in x- and y-components to the PLLs via low- and high-pass filters, respectively. The vertical component is transmitted to the first PLL, where the amplitude and frequency are measured. The amplitude is kept constant by adjusting the excitation of the cantilever and the frequency shift applied to regulate the distance to the sample and, thereby, to generate the topography map. In the second PLL the horizontal signal is also used to maintain the amplitude, the frequency shift is, however, recorded as torsional imaging signal.

2.1.4 Cantilever Preparation

The cantilevers employed during this study are non-contact silicon cantilevers (Point-probe Plus-NCL, PPP-NCL) purchased from *Nanosensor GmbH*. Their spring constant k is specified as 21 to 98 Nm⁻¹ along with their dimensions (length \sim 225 μ m, width \sim 38 μ m and thickness \sim 7 μ m), this results in a first flexural resonance at $f_1 \approx$ 170 kHz, a second flexural resonance at $f_2 \approx$ 1.05 MHz and the first torsional resonance at $f_t \approx$ 1.5 MHz. The shape of the cantilever is visible in the scanning electron microscope (SEM) image in Figure 2.3a. The front of the cantilever is shown along with the pyramidal tip.

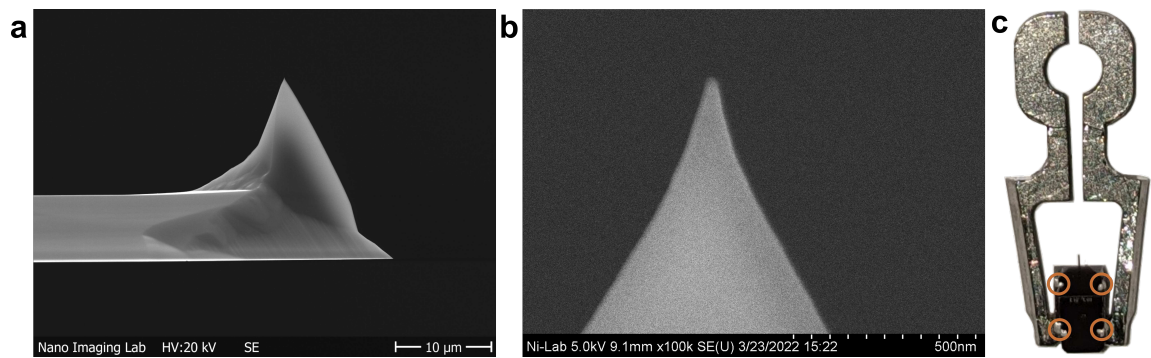


Figure 2.3: The cantilevers. *a*, SEM image of the cantilever with tip. *b*, Close-up SEM image of the sharp tip apex. *c*, Image of a cantilever glued to its holder with a four spot gluing technique (orange circles).

The tip apex, crucial for high-resolution imaging, is shown to be less than 30 nm wide in the close-up SEM image of the tip in Figure 2.3b.

For transfer and insertion into the microscope the cantilevers are glued to cantilever holders with a plate angled at 15 ° using a four spot gluing technique as shown in Figure 2.3c with a two component conductive epoxy glue to achieve high Q -factors. This reliably yields Q -factor values of close to 30000, 10000 and over 100000 for the first, second and torsional resonances, respectively. After an annealing for 1 h at 120 °C to harden the glue, the cantilevers are introduced into the vacuum system on holder plates. There, they are degassed for 1 h at 130 °C on the manipulator heater to remove residual pollution. Afterwards, the cantilever, and specifically the tip, are argon sputtered for 1 min at 1 keV to remove the native silicon oxide covering the tip [100].

2.2 The Low Temperature Setup

2.2.1 The LT UHV Setup

The low temperature measurements and the associated preparations are, also, performed under UHV conditions in a three chamber UHV system, shown in Figure 2.4.

The three chambers, analysis- (dark red) and preparation (blue) chamber, and load-lock, are separated by gate valves and connected via a motor driven manipulator and transfer cane, respectively. The preparation chamber is pumped via a turbo-molecular pump connected to a prevacuum pump, an ion getter pump and a TSP to maintain a base pressure of $\sim 10^{-10}$ mbar. Connected to it are various preparation devices, including a sputter gun and UHV leak valve, an e-beam on the manipulator, a three cell molecule evaporator, a QMB and an access valve for the ESD setup and UHV suitcase.

The analysis chamber houses the microscope inside the cryostat, described in the following Section 2.2.2, and a sample storage. The base pressure of $\sim 10^{-10}$ mbar is maintained by an ion getter pump and a TSP.

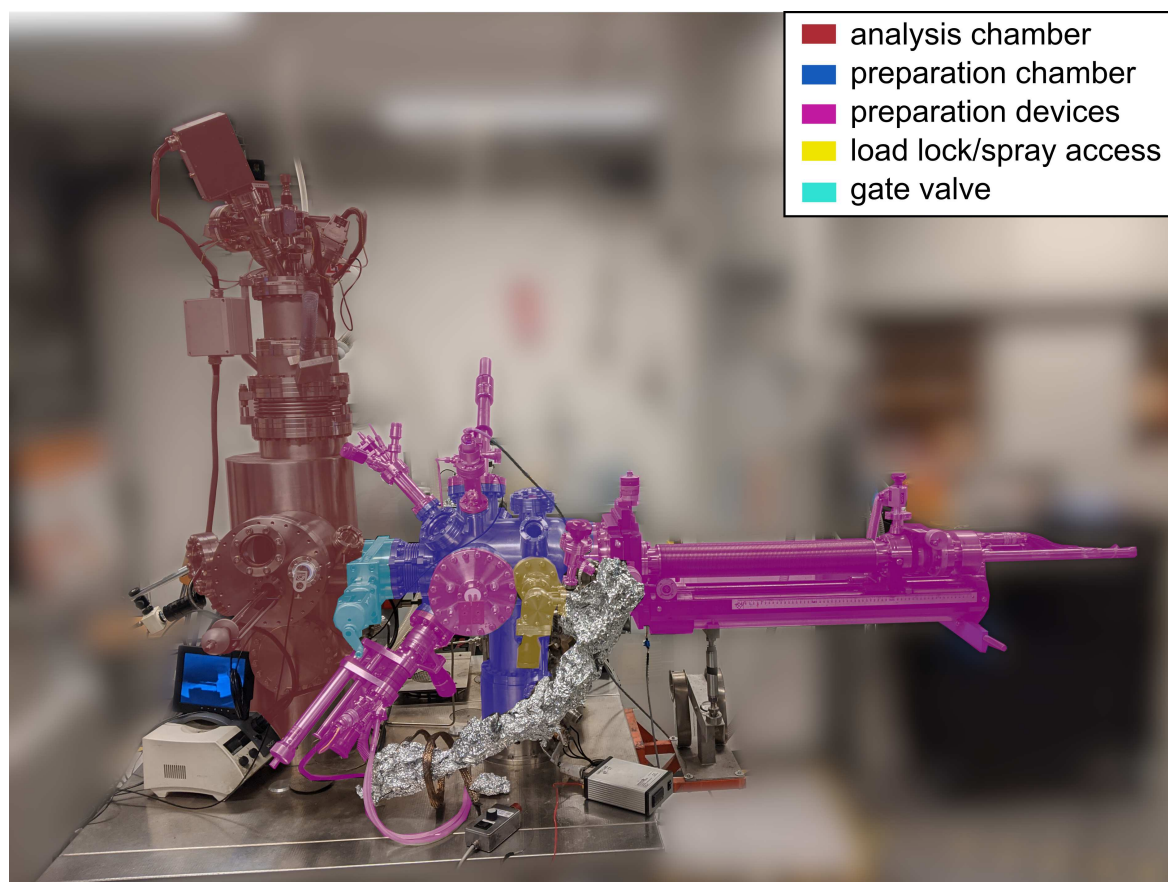


Figure 2.4: The LT UHV setup. *The microscope and cryostat (dark red) are connected via a gate valve (turquoise) to the preparation chamber (blue). There, various preparation devices (pink), including an e-beam and radio frequency heater, a sputter gun with UHV leak valve and a molecule evaporator are connected. Also visible is the attachment setup (yellow) for transfer suitcase and ESD device.*

The last chamber is the load-lock used, similarly to the room temperature setup, to insert samples and tips, pump the molecule evaporator for replacement of molecules and for suitcase access. It is connected to a turbo-molecular pump with a prevacuum pump attached to it, achieving pressures below 10^{-8} mbar.

2.2.2 The LT Microscope and Cryostat

The LT microscope built by *Omicron NanoTechnology GmbH* (now: *ScientaOmicron GmbH*) is housed inside a two chamber cryostat. The outer is, thereby, cooled with liquid nitrogen ($T_{N_2} = 77$ K), while the inner can be cooled with either liquid nitrogen or liquid helium ($T_{He} = 4.7$ K), allowing stable measurements at these temperatures. The microscope, accessible via two shutters, consists of a sample holder and a qPlus sensor, introduced in Section 1.5 before, located on a piezoelectric scanner. For noise reduction it can be decoupled via springs and is then damped, as the RT microscope, via eddy current damping.

2.2. The Low Temperature Setup

The tips attached to the qPlus sensor, shown in Figure 2.5, can be prepared during measurements and further be modified, as described in the section below.



Figure 2.5: The qPlus sensor with a tungsten tip. *Close-up photography of a qPlus sensor used in the LT setup. Visible are the two prongs of the tuning fork, one immobilized, the second one equipped with the long tungsten tip and the metal wire allowing measurement of the tunneling current.*

The qPlus sensor exhibits a higher stiffness than the cantilevers used at RT of about $k = 1800$ N/m and a corresponding resonance frequency of 25 kHz.

2.2.3 Tip Preparation and Modification

The tips, during this work made from tungsten, are chemically etched and milled with focused ion beams to achieve low tip radii and removal of oxide contaminations [101, 102]. During measurements the tip can be sharpened by indenting it into the surface and applying bias pulses, until a continuous exponential current–distance relation can be observed.

Modifications of the tip, during this work solely performed with CO molecules, are achieved by first adsorbing CO on the surface via leaking CO at a pressure of around $\sim 10^{-8}$ mbar. On the surface the CO can be detected during STM scans as small protrusions or depressions. Either, the molecule is picked up by chance or it can be adsorbed to the tip by performing a distance-current spectroscopy. Successful pickup is then indicated by a jump in the spectroscopy current.

2.2.4 Measurement Control

The measurement control at LT is realized using a Nanonis RC5 electronics consisting of a real-time controller, one PLL, a power supply and high voltage amplifier, a signal converter and an Omicron interface converter by *SPECS Zurich GmbH* with its corresponding software. The PLL, thereby, is used to excite and control the oscillations during AFM measurements, while the power supply and amplifiers facilitate the STM measurements.

2.3 Surface Preparation

For the studies performed during this work, atomically clean surfaces with large and flat terraces for the study of adsorbed molecules are desired requiring specialized preparation and handling for the different types of substrates. Thus, three distinct surface preparation methods are employed during this work, annealing and sputtering of single crystals for metallic samples, cleavage for bulk insulator ionic crystals of KBr and exfoliation and annealing for HOPG. Each method is described in more details in the following.

2.3.1 Preparation of Au(111) and Ag(111)

The vast majority of the experiments presented in this work are performed on Au(111) or Ag(111) surfaces. Their single crystal were bought at *Mateck GmbH* and are cleaned by several cycles of sputtering and annealing, leading to flat surfaces with large terraces separated by mono-atomic steps. On Au(111) the cleanliness can be verified by its distinct herringbone reconstruction (HB) and its modification upon adsorption of pollutants or molecules as discussed in details in later chapters [103, 104]. The HB is formed due to a misfit between surface layer and substrate resulting in a step-wise pattern of dislocations pairs separating domains of atoms in face-centered-cubic (fcc) and hexagonal close-packed (hcp) sites [103].

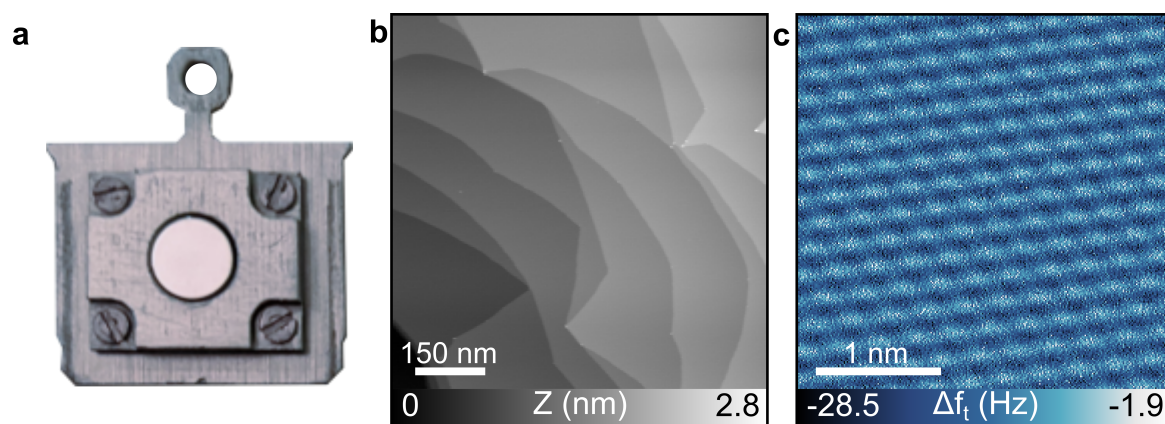


Figure 2.6: Ag(111) surface with atomic resolution. *a*, Ag(111) sample screwed to sample plate via a top plate. *b*, nc-AFM topography image of a clean Ag(111) surface with clean terraces and monoatomic steps ($A_1 = 5 \text{ nm}$ $\Delta f_1 = -10 \text{ Hz}$). *c*, Torsional frequency shift image of the atomic structure of Ag(111) ($A_2 = 800 \text{ pm}$ $\Delta f_2 = -367 \text{ Hz}$, $A_t = 40 \text{ pm}$).

A sample mounted by screwing a top plate on top of a polished hat shaped single crystal is shown in Figure 2.6a. A representative topography image of Ag(111), showing large and clean terraces separated by monoatomic steps, is presented in Figure 2.6b along with a high resolution torsional frequency shift image showing the hexagonal atomic lattice structure of the surface in Figure 2.6c.

2.3.2 Preparation of KBr(001)

The bulk insulator KBr(001) samples were purchased as bulk crystals from *Mateck GmbH*. After cleaving small rectangular cuboids, holes are drilled into the bottom and the KBr crystals fixed to sample plates with tungsten wires, as shown in Figure 2.7a.

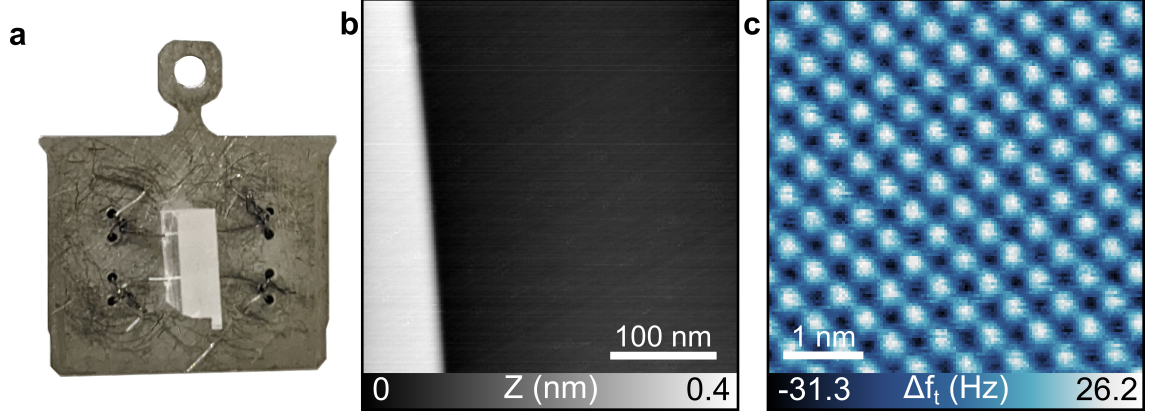


Figure 2.7: KBr(001) surface with atomic resolution. *a*, KBr(001) sample mounted with tungsten wires. *b*, nc-AFM topography image of a clean KBr(001) surface with clean terraces and a monoatomic step ($A_1 = 5 \text{ nm}$, $\Delta f_1 = -50 \text{ Hz}$). *c*, Torsional frequency shift image of the atomic structure of KBr(001) ($A_2 = 800 \text{ pm}$, $\Delta f_2 = -183 \text{ Hz}$, $A_t = 40 \text{ pm}$).

The samples are then cleaved and inserted into the UHV system within one minute to preserve their cleanliness. After insertion the samples are annealed to remove charges and remaining pollutants, resulting in flat terraces with mono- to triatomic steps between them. A representative topography image and an atomic resolution torsional frequency shift image are shown in Figures 2.7b and c. Atomic resolution measurements of the cubic lattice are used to verify both the cleanliness and also the piezo scanner calibration of the nc-AFM at RT.

2.3.3 Preparation of HOPG

The HOPGs are exfoliated in air with *Scotch Magic tape* until a flat and smooth surface with no flakes is achieved. The samples are then inserted into the UHV system within one minute and annealed to remove remaining pollutants. This provides well extended and flat terraces with minimal steps. A mounted HOPG sample is shown in Figure 2.8a. A representative topography image of the resulting surface and a torsional frequency shift image of the hexagonal lattice can be found in Figures 2.8b and c. A large clean terrace with a single monoatomic step is visible. Slight pollutants can be observed at the step edge.

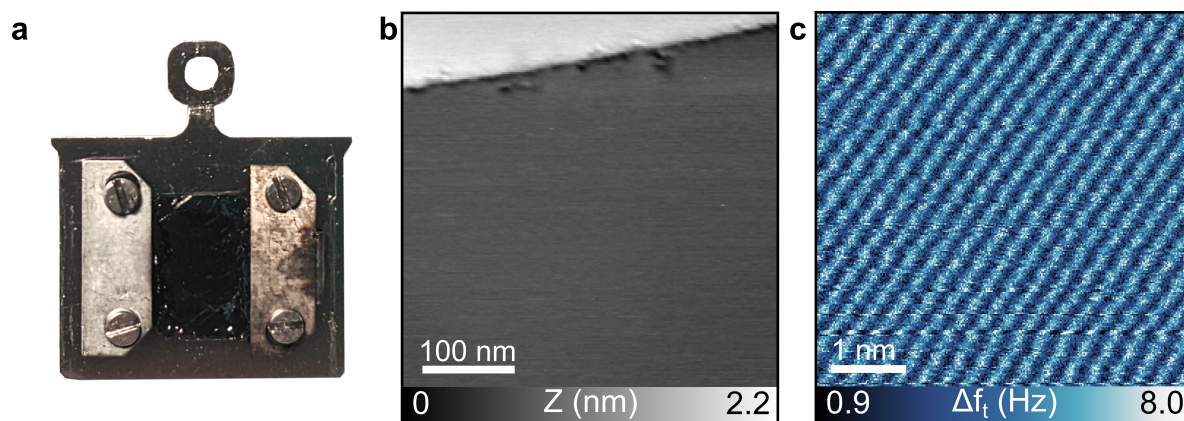


Figure 2.8: HOPG sample with atomic resolution. **a**, HOPG sample clamped to sample plate. **b**, Large scale nc-AFM topography image of a clean HOPG sample ($A_1 = 5 \text{ nm}$, $\Delta f_1 = -40 \text{ Hz}$). **c**, Torsional frequency shift image of the atomic structure of HOPG ($A_1 = 3 \text{ nm}$, $\Delta f_1 = -160 \text{ Hz}$, $A_t = 80 \text{ pm}$).

2.4 Summary

In this chapter, the UHV systems required to maintain cleanliness desirable for high-resolution studies of molecular properties on surfaces were explained. The nc-AFM operated at RT with optical detection and its cantilever along with their preparation were introduced. In this way, atomic and submolecular resolution can be achieved. Next, the LT STM/AFM equipped with its distinct qPlus sensor and tip modification allowing bond level resolution were discussed. Last, the preparation of different types of samples, metallic, insulating bulk ionic crystals and semi-metallic crystals, relying on cycles of sputtering and annealing, cleavage and exfoliation were explained.

Electrospray Deposition

THE deposition of complex molecules, possibly containing functional moieties with sufficient cleanliness for high-resolution SPM studies on surfaces in UHV poses some significant challenges. The most common method of depositing molecules on surfaces in UHV is thermal evaporation, where molecules are sublimated from powder onto surfaces, as will be described in Section 3.1 [105]. With increasing molecular weight and especially higher complexity and specific functionalizations like alkyl chains the temperature of sublimation increases, while the thermal stability of the molecules decreases, limiting TE to thermally stable and relatively small molecules [106]. For certain types of target structures, most prominently graphene-like macromolecules, e.g. GNRs, this can be circumvented by depositing rationally designed precursors and performing on surface reactions to synthesize the desired more complex molecule directly on the surface [107, 108]. Such precursors, however, are still limited in their complexity and functionalization by the deposition and, thus, only certain structures and functionalizations can be synthesized on surface. Especially three-dimensional structures and fragile substituents are not accessible, as will be discussed in detail in Chapter 6. In addition, on surface synthesis is, with rare exceptions, limited to metal surfaces [109], generally excluding insulating or semi-conducting surfaces, therefore hindering decoupling or device integration [110, 111].

Thus, alternative approaches for the deposition of complex and large molecules, also onto non-metallic surfaces in UHV are required.

In Section 3.1.1, alternate deposition approaches, ranging from specialized evaporation methods to contact transfer and solution based methods are discussed. For this work, the well-established electrospray deposition method was chosen due to the high purity achieved, while allowing quite similar coverage and control to thermal expansion, as verified below. The principles of ESD are explained in Section 3.2 with the setup employed during this work introduced in Section 3.3, followed by a literature overview in Section 3.4. Finally in Section 3.5, a comparison of thermal evaporation and ESD on metal, insulating and semi-conducting surfaces is presented, substantiating the similar coverage and high cleanliness of ESD, and demonstrating the influence ESD can have on molecular adsorption and surface modification.

3.1 Molecular Deposition Methods

Molecular deposition onto surfaces in UHV is in most applications performed by thermal evaporation from a Knudsen cell under UHV conditions [105]. Molecules from powder are heated in a crucible to sublime in order to reach the surface. For this, a small amount of molecules is inserted in a metallic or quartz crucible, depending on measurement setup, and placed in the evaporator. Thereafter, the setup is pumped down and outgassed by heating close to the sublimation temperature. The rate of deposition can be finely calibrated using a QMB, which determines deposition volumes by measuring the change in frequency of a swinging quartz upon deposition. This makes highly precise coverage formation on the surface possible by adjusting rate and deposition time. Further, reliant on pure source material and outgassing of molecules, clean surfaces covered with only the desired molecule coverage without any contaminants can be obtained. Thermal evaporation can be performed on any substrate with high cleanliness and with minimal modification of the surface properties.

However, it is limited to the deposition of molecules thermally stable up to at least their sublimation temperature, otherwise undesirable reactions like polymerization or dissociation of fragile moieties of the molecules can occur [112]. Thus, sublimation is generally limited to molecules with a molecular weight below 1000 g/mol [113]. Therefore, certain types of molecules, prominently biomolecules (DNA, proteins, etc.), polymers and nanoparticles are not accessible by thermal evaporation. This is either due to their thermal lability or the impossibility to obtain them without the presence of water or other necessary solvents. Importantly here, the limitations of TE concern alkyl chain functionalized molecules due to fragmentation and solution synthesized GNRs.

3.1.1 Alternative Deposition Methods

A possible way of circumventing the thermal lability of molecules and their fragile functional groups during sublimation is the rapid heating approach, based on considerations of the kinetics of decomposition and evaporation [114]. By specific choice of the temperature and rate of heating the sublimation of molecules can be favored over dissociation processes for short periods of time. Due to the high rate of heating and quick time-response required for rapid heating deposition laser pulses are generally used for heating instead of crucibles [115]. While this method allows deposition of additional molecules by sublimation, the yield of rapid heating is comparatively low, generally preventing high coverage of surfaces [106]. In addition, the deposition of larger molecules, like nanographenes, is still limited. Furthermore, rapid heating is only available for molecules which can be dried without damaging their structure, since the basic principle is still based on heating from powder.

For larger molecules, especially with low or no solubility, like carbon nanotubes, direct contact transfer from powder provides a possible deposition method [116, 117]. Thereby, molecules are impregnated onto a fiberglass sheath *ex situ*, which is then inserted into UHV and, along with the molecules on it, degassed. Thereafter, the desired substrate is brought into contact with the sheath, transferring a certain amount

of molecules onto the sample. This can often lead to the formation of large molecule clusters on the surface, severely limiting the investigation possibilities by STM and nc-AFM. If only few, large molecules are transferred, notably carbon nanotubes, finding the desired structures on the surface can become difficult. Recent advances, like matrix-assistance, have allowed the transfer of new GNR precursors and fragile porphyrins with high purity [118,119].

The investigation of large or fragile soluble molecules or species, which need to be kept in solvent (e.g. DNA), can be achieved with pulsed valve deposition [120–124]. It is based on forming a small leak into the UHV chamber for short periods of time with a pulsed valve. Through it a molecule solution is inserted and can access the sample. The number and time of pulses, and, thus, the amount of solution entering the chamber can be used to tune the coverage. As a result of the quasi direct entry and access of the solvent and other contaminants to the surface during deposition, often times pollution of the surface cannot be avoided. Furthermore, the reproducibility of depositions is somewhat limited due to the complex fluid dynamics during deposition [106].

An alternative approach, which does not rely on the surface being exposed to the direct influence of solvent, is electrospray deposition [16–18, 20, 21, 125] based on accelerating molecule droplets from a solution towards a surface in UHV through a differential pumping setup. Its function and setup are described in the following.

3.2 ESD Principle

Electrospray deposition is well suited for biomolecules, polymers, solvent necessitating molecules and can generally be used for all soluble molecules [16–18, 21]. It is based on the electrospray ionization process developed by Fenn for generating gas-phase ions from non-volatile and large molecules, prominently the aforementioned biomolecules, for their study with mass spectroscopy [14, 15]. Before, such molecules were generally inaccessible via ionization due to their large, fragile and thermally labile structures [15, 126]. The adaptation of ESI to surface science applications in UHV was achieved in 2006 with depositions of polymer layers and molecules [16, 127]. Thereby, a controlled leak is introduced to the UHV system. For this, a differential pumping setup and for certain setups mass spectrometer are connected, reducing solvent and contaminant particles reaching the system and maintaining a low pressure during deposition. Charged droplets are accelerated by high-voltage from a molecule solution towards the entrance capillary of the pumping stages and solvent evaporates, leading to the formation of smaller droplets or charged gas phase ions [16]. Through the pumping stages remaining solvent and contaminants are mostly removed or filtered out depending on setup and the molecules can arrive on the surface. ESD and ESI allow the deposition of a variety of molecule species, prominently molecules with increasing complexity and fragile groups, as long as solubility can be maintained [17–35]. In recent years insulating surfaces or semiconductors have also become accessible as substrates [21, 34].

A photo of an ESI source along with the spray jet and a schematic illustration of the ESI process are presented in Figures 3.1a and b. The molecules are dissolved

Chapter 3. Electro spray Deposition

and supplied to an emitter, formed by a small capillary. A high voltage is applied to the solution, inducing a strong electric field in relation to the counter electrode - the entrance to the vacuum system. Thereby, some molecules are oxidized and a separation of charges is induced by the electrical field. This leads to the formation of an elongated droplet at the tip of the emitter due to the interplay of liquid surface tension and the electrostatic force. For a sufficiently strong field charged droplets are emitted from the shape, ranging from large single to many small droplets [128].

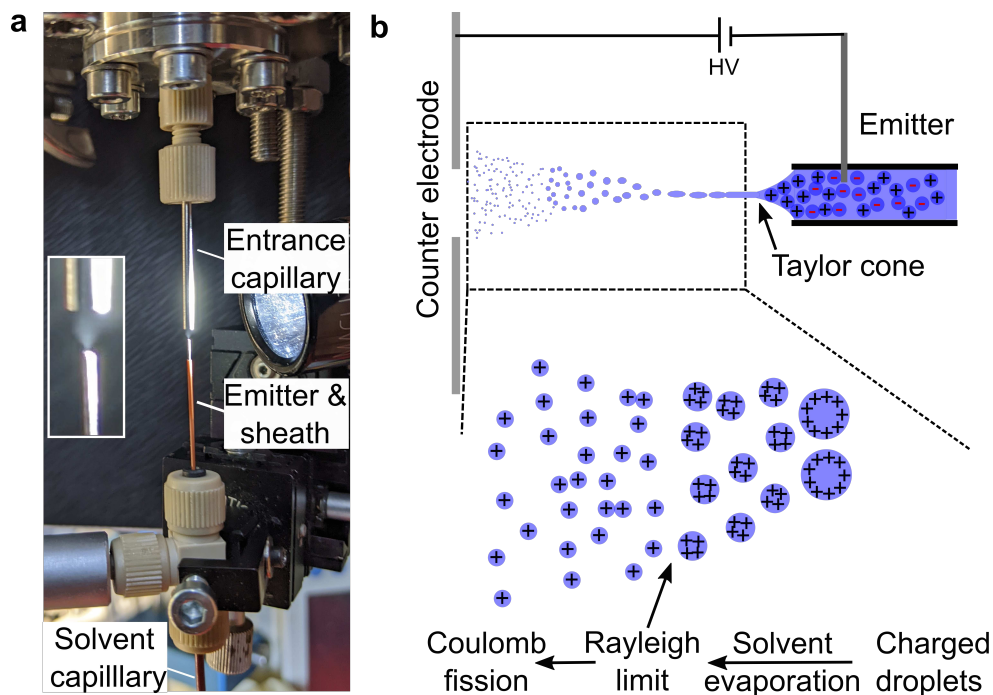


Figure 3.1: Function of the electro spray setup. *a*, The emission setup with the spray cone inset. *b*, Illustration of the function of the spray.

At a critical voltage the so called Taylor cone, a conical meniscus emitting a spray of small charged droplets from its apex, is formed [129–131]. On further increase of the voltage the jet starts to oscillate and multiple jets form [132]. This is illustrated in Figure 3.2.

The optimal emission of charged droplets occurs around the critical voltage for the Taylor cone. The necessary voltage, thereby, strongly depends on the properties and flow rate of the molecule solution and the emitter geometry [133]. Since the fluid dynamics in the capillary and, thus, the optimal parameters can not easily be reproduced, a precise optimization of these parameters is mandatory for each spray process to achieve optimal surface deposition.

Upon emission the charged droplets are accelerated towards the counter electrode formed by the entrance capillary to the differential pumping setup. The solvent in the droplets starts evaporating, reducing their size and, consequently, the charge-to-volume ratio of the droplets increases. The maximum charge a droplet can hold is defined by the critical charge q_r in the Rayleigh limit [134]:

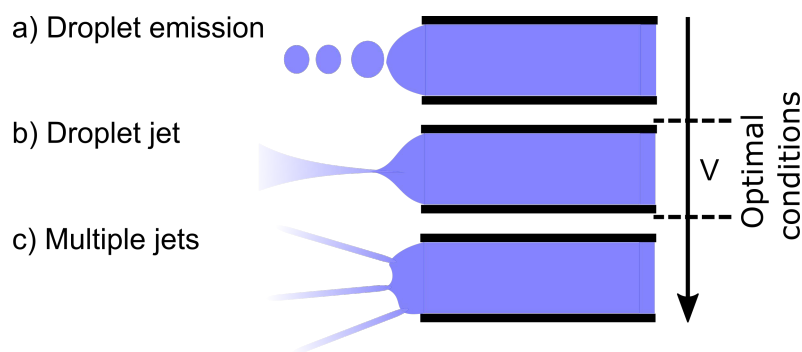


Figure 3.2: Modes of the electrospray depending on voltage. *At low voltages **a** single droplets are ejected in a drip like fashion. Upon reaching a critical potential the taylor cone forms and a stable droplet jet, the spray occurs **b**. With further potential increase multiple jets and oscillating jets start to form **c**.*

$$q_r = 8\pi\sqrt{\epsilon_0\gamma R^3} \quad (3.8)$$

Here, ϵ_0 is the vacuum permittivity, γ the surface tension of the solvent and R the radius of the droplet.

When the charges in the droplet reach the Rayleigh limit, the surface tension is equal to the coulomb repulsion. With further increase the droplets become unstable and undergo Coulomb fission, forming smaller droplets, to increase their surface area [135, 136]. Droplets from electrospray generally are not perfectly spherical and, therefore, undergo Coulomb fission already before reaching the Rayleigh limit [137]. With further evaporation of solvent, repeating cycles of coulomb fission occur reducing the size of the droplets down to the nanometer scale [138]. The small droplets either impact the surface or single gas-phase ions of the molecules are formed. Various models describe the formation of gas-phase ions from charged droplets from ESD. The most common are the charge residue model (CRM) and ion evaporation model (IEM) or especially for well-extended molecules, like DNA or polymer chains, the chain ejection model (CEM) [138]. The three processes are described in the following and illustrated in Figure 3.3.

The IEM is best applicable for small molecules [139]. It assumes the ejection of the molecule from the small droplet generated by coulomb fission as a gas-phase ion due to the electric field between charged molecule and surrounding droplet when the droplet size approaches the Rayleigh limit [138, 140–142].

Similarly, the CEM describes the formation of gas-phase ions of (unordered) chain-like molecules as a step wise charging and ejection by diffusion towards the droplet surface because of electrostatic force until the chain is fully detached from the droplet [143, 144].

In the CRM, formation of gas-phase ions is assumed to occur due to charges remaining after the complete evaporation of residual solvent around the molecule. Thereby, the presence of only single molecules is assumed in each droplet after repeated coulomb

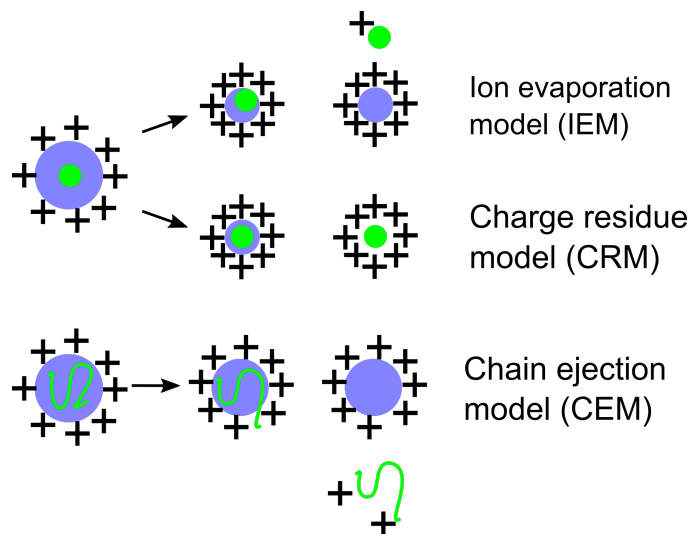


Figure 3.3: Formation of gas-phase ions after ESD. *Schematic representation of three models of gas-phase ion formation, ion evaporation model, charge residue model and chain ejection model. Molecules/ribbons are shown in green.*

fissions [138, 145, 146], necessitating a low initial concentration in the spray solution. The CRM seems to better describe the ionization of larger molecules with higher molecular weight [139].

A clear distinction between the three models, however, is not possible, since especially for not well-extended molecules in small droplets the ejection of the molecule from the droplet in IEM might also be treated as another Coulomb fission and, thus, similar to the CRM [106].

3.3 ESD Setup

The electrospray depositions presented in this thesis are performed with a commercially available ESD setup from *MolecularSpray Ltd.* modified with the addition of a final stage pumped by a second turbo-molecular pump to enhance the cleanliness of resulting samples. The spray setup is visualized in Figure 3.4. It consists of the spray emission setup a four stage differential pumping system and is connected to the main chamber via a gate valve.

The spray emission setup, shown in detail in Figure 3.1a, is formed by the emitter, a capillary with an inner diameter of 100 μm , to which the solution is supplied from a syringe pump via a poly ether ether ketone (PEEK) tube. The emitter is stabilized by a sheath and fixed to a "T" shaped piece, where the electrode is directly contacted with the solution supplied opposite from the emitter. For positioning of the emitter in relation to the stainless steel entrance capillary the "T" piece is attached to a xyz-stage. A power supply connected to the electrode supplies high voltage from 0.5 kV up to 5 kV between solution and entrance capillary to induce the spray. For optimal deposition conditions the voltage should be below 2 kV for the solution mixtures used

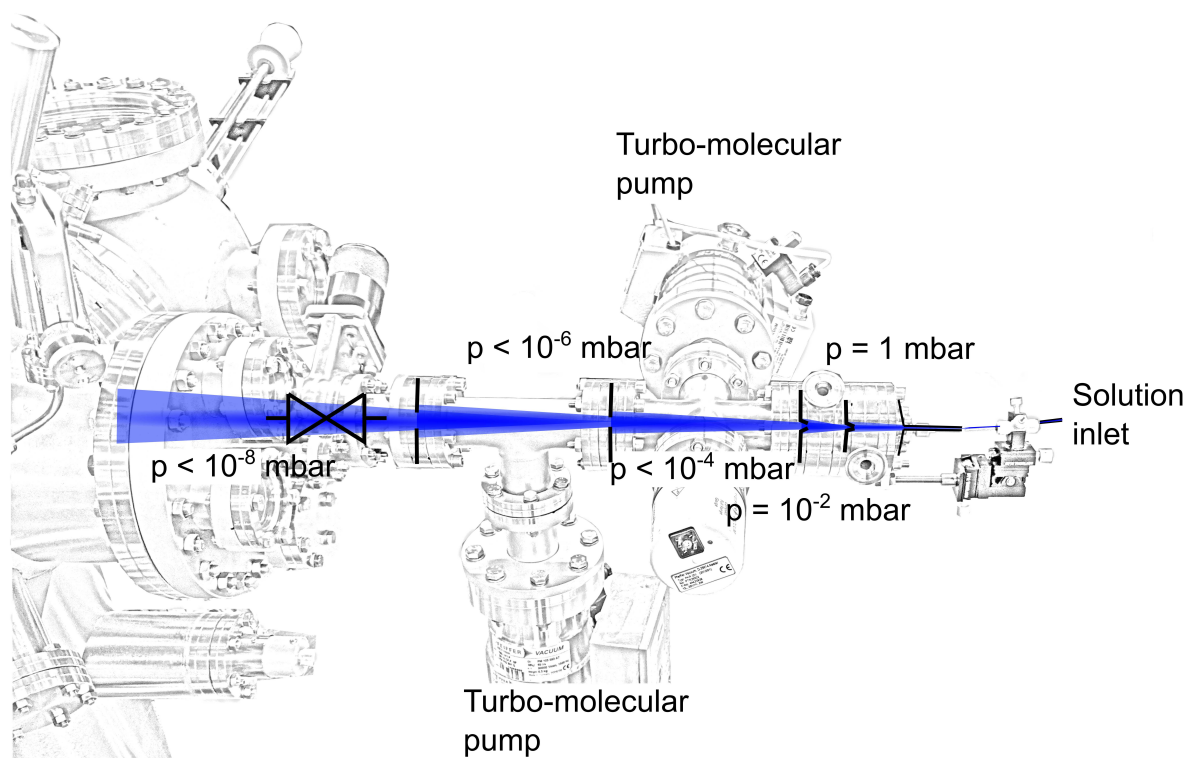


Figure 3.4: Illustration of the electro-spray setup. *The spray system attached to the RT system consists of an emission setup and a four chamber differential pumping setup with two rotary and two turbo-molecular pumps.*

during this work. The jet of sprayed droplets transverses the distance between emitter and entrance capillary of about 1 mm to 5 mm and enters the differential pumping stages through the 0.0762 mm opening.

The differential pumping setup consists of four stages, pumped by two rotary pumps for 1st and 2nd stages and two turbo-molecular pumps connected to one rotary pump for the 3rd and 4th, yielding operational pressures of 1 mbar, 10^{-2} mbar, 10^{-4} mbar and 10^{-6} mbar. The stages are separated by apertures with diameters of 0.4 mm and 0.6 mm, 1 mm and slightly above 1 mm. The first two are formed by skimmer cones, designed to collimate the droplet jet. After exiting the last aperture the spray droplets pass through the gate valve, separating spray setup from main chamber, to the sample positioned in front of the spray by the manipulator. During deposition the pressure in the preparation chamber remains below 10^{-7} mbar, while the microscope is separated by another gate valve, as described previously. Upon closing the gate valve, the pressure rapidly decreases and recovers the base pressure of 10^{-10} mbar in less than one hour.

The quality of the spray and, therefore, also of the deposition strongly depends on the choice and composition of solvent mixture. To facilitate the spray the solution has to be polar or conductive. This, however, would limit the solubility of a large share of organic and otherwise apolar and non-conductive molecules. Either small amount of acid or base can be added, or the molecules are in a first step dissolved in an apolar

solvent. Thereafter, a small amount of a polar solvent, like methanol, is added for polarity. During this work, the most common solvent mixture is toluene/methanol, with only one type of GNR being dissolved in chlorobenzene/methanol.

3.4 Examples of ESD of Molecules

Electrospray ionization was, as previously mentioned, developed by Fenn for mass spectroscopy [14] and has since been adapted to further fields of application, notably molecular surface depositions [16,127,147]. The first depositions on surfaces in vacuum were performed in 2006 with depositions of poly(ethylene) oxide (PEO), gold nanoparticles, and bovine serum albumin (BSA) [16,127]. The gold nanoparticles formed large, high aggregations on a HOPG surface with high mobility observed for uncoated clusters. This resulted in covered step edges of the previously clean substrates, as visible in Figure 3.5a. Similarly, the deposition of the BSA proteins leads to decorated step edges, but also to two-dimensional fractal clusters on the surface as can be observed in Figure 3.5b. The subfigures a-d show different coverage levels of the surfaces dependent on the position in the spray jet gradient. The lowest density is observed at the edge of the spray jet in subfigure a, while the highest coverage in subfigure d is observed in the center of the jet. In an additional step, the influence of the deposition voltage on the morphology and intactness of the molecules was assessed showing ESD to be well suited to deposit even fragile biomolecules with specific choice of parameters and possibly soft landing mechanisms – the application of a deceleration voltage either to the sample or an electrode [125].

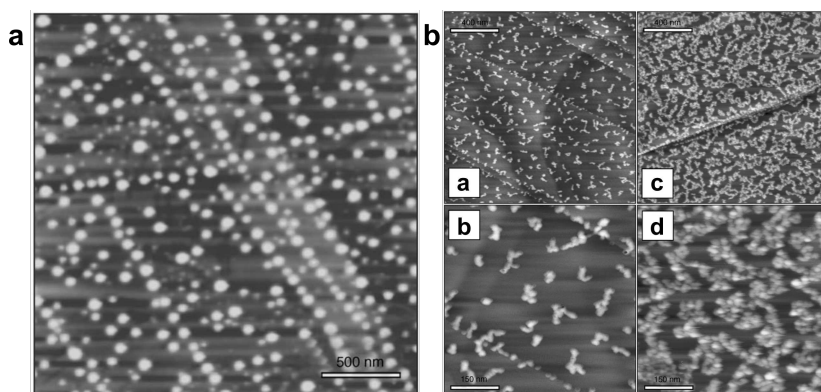


Figure 3.5: Electro spray deposition in vacuum. **a**, AFM topography image of gold nanoparticles on HOPG deposited with ESD. **b**, AFM topography image of BSA deposited with ESD on HOPG, resulting in a variety of coverage on different regions of the surface dependent on the position in the spray jet gradient. Adapted from [16].

Shortly thereafter, the first depositions of the commonly used pure carbon C_{60} (structure shown in Figure 3.12a), were reported on Au(111) and a supramolecular network of 3,4,9,10-perylene tetracarboxylic diimide (PTCDI)/melamine thereupon [17,18]. Deposited onto clean Au(111) with ESD, C_{60} at low coverage covers the step edges along with the formation of small clusters on the large terraces of the surface as visible in

Figure 3.6a [17]. Thereby, low coverage was achieved by aligning the sample slightly below the direct line of sight of the spray setup. Upon direct alignment multilayer coverage could be obtained showing the possibility of precise control of molecular coverage by spray using multiple parameters, e.g. time of deposition, alignment of sample and the aforementioned deposition voltage.

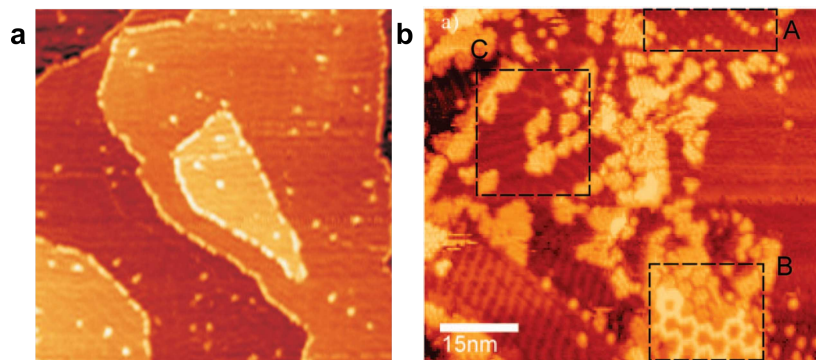


Figure 3.6: Electropray deposition of C_{60} . **a**, STM image of C_{60} molecules on Au(111) after ESD. **b**, STM image after deposition of C_{60} on a supramolecular network on Au(111). The marked areas demonstrate the three observed surface morphologies. Adapted from [17, 18].

The hydrogen-bonded supramolecular network of PTCDI/melamine on Au(111) forms bimolecular networks with hexagonal [148] and parallelogram [149] shaped pores. Deposition of C_{60} with ESD allowed insight into the effect of electro sprayed molecules impacting with a network structure and into their adsorption. In Figure 3.6b, a large scale STM topography image shows the surface morphology after 2 min of ESD. Marked in the boxes are different surface morphology areas. Area A shows a region of parallelogram network with rows of C_{60} filling the pores, area B shows hexagonal pores filled with C_{60} heptamers and area C shows an area free of C_{60} . The trapping in the networks as well as the existence of undisturbed network parts give clear evidence that ESD can be used to deposit molecules without a soft-landing mechanism with only relatively small influence on supramolecular networks.

The possibility of depositing weakly soluble carbon nanotubes (CNT) was also shown on the native oxide of Si(111) in 2007 [23]. Well-elongated double-walled CNTs (up to 10 μm) were suspended in ethanol by sonication directly before deposition. This procedure can be repeated during deposition, since the solution reservoir can be removed for further sonication without pausing deposition, making a build-up of higher coverage possible.

Resulting AFM topography images, presented in Figures 3.7a and c, show bundles of and isolated CNTs on the Si(111) surface. Lengths of up to 1.8 μm and heights of 1.5 to 3.5 nm (compare Figure 3.7b) are revealed, consistent with the height of double-walled CNTs. The length was filtered by a 2 μm frit filter to avoid large bundles entering the system and, thus, also within expected ranges.

The presence of both small bundles and isolated CNTs indicates no significant aggregation in the inlet capillary or an unbundling therein. This in combination with

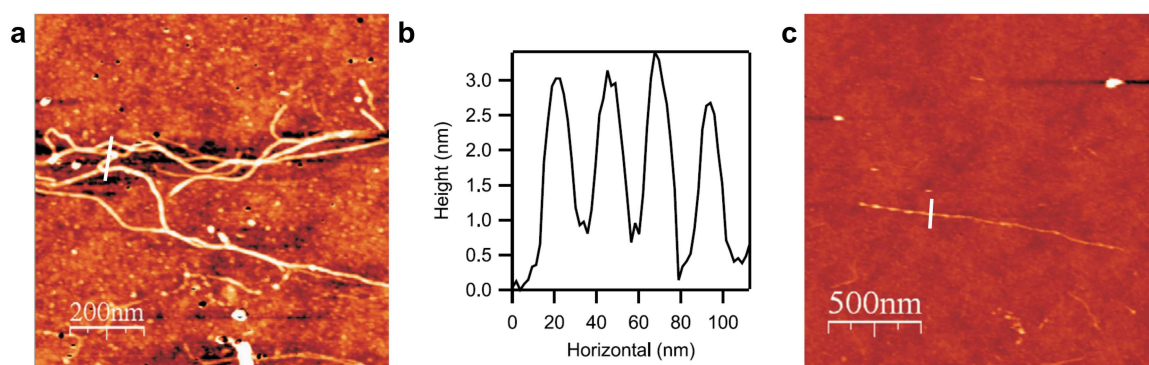


Figure 3.7: Electro spray deposition of carbon nanotubes. *a*, AFM topography image of double-walled carbon nanotube bundles on Si(111). *b*, Profiles along marked lines of *a*. *c*, AFM topography image of an isolated CNTs on Si(111). Adapted from [23].

the high cleanliness of the sample allows high-resolution studies of even barely soluble molecules with the help of ESD.

The first depositions of polymer chains and their oligomers were reported in 2010 [24]. Porphyrin hexamers and polymers – structures shown in Figure 3.8a – were deposited on Au(111). Close packed networks could be observed for hexamers, formed due to interdigitation of octyloxy side chains included to promote solubility, as shown in the STM image and corresponding model in Figure 3.8b.

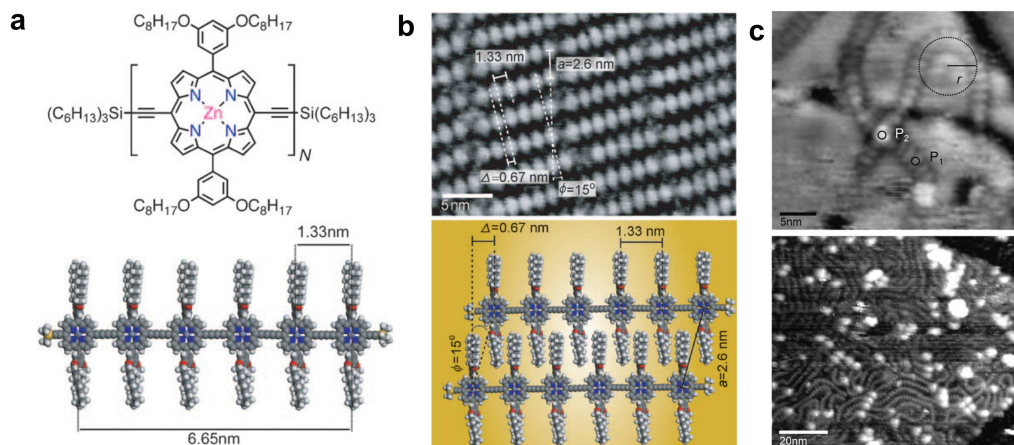


Figure 3.8: Electro spray deposition of polymers. *a*, Structure of porphyrin hexamers and polymers. *b*, STM image of a close packed domain of a hexamer deposited by ESD on Au(111) along with a structural model. *c*, STM images of porphyrin polymers on Au(111) with curvature radius and bright crossover points. Adapted from [24].

Deposition of porphyrin polymers resulted in long curved chains with high coverage on the surface. Figure 3.8c shows both a high-resolution STM image as well as a large scale topography image. The polymers are visible with strongly curved structures and crossover each other in the top image. Coverage is quite uniform over a large area

3.4. Examples of ESD of Molecules

with occasional pollution visible in the bottom image. With these depositions ESD was shown to also provide well suited coverage for polymers and elongated structures. However, pollutants can be observed, most likely from solvent, somewhat reducing the resolution and possibly influencing the adsorption. Thus, solvent influence has to be taken into account especially for well-elongated molecules.

The deposition of well-elongated molecules as well as sensitive biomolecules allowed the deposition of single-strand DNA (ssDNA) molecules [19, 150]. This enabled the study of ssDNA on Au(111) surfaces after consecutive annealing steps up to 500 K [150]. The surface morphology, provided in Figure 3.9a, thereby, evolved from large aggregates to isolated oligomers.

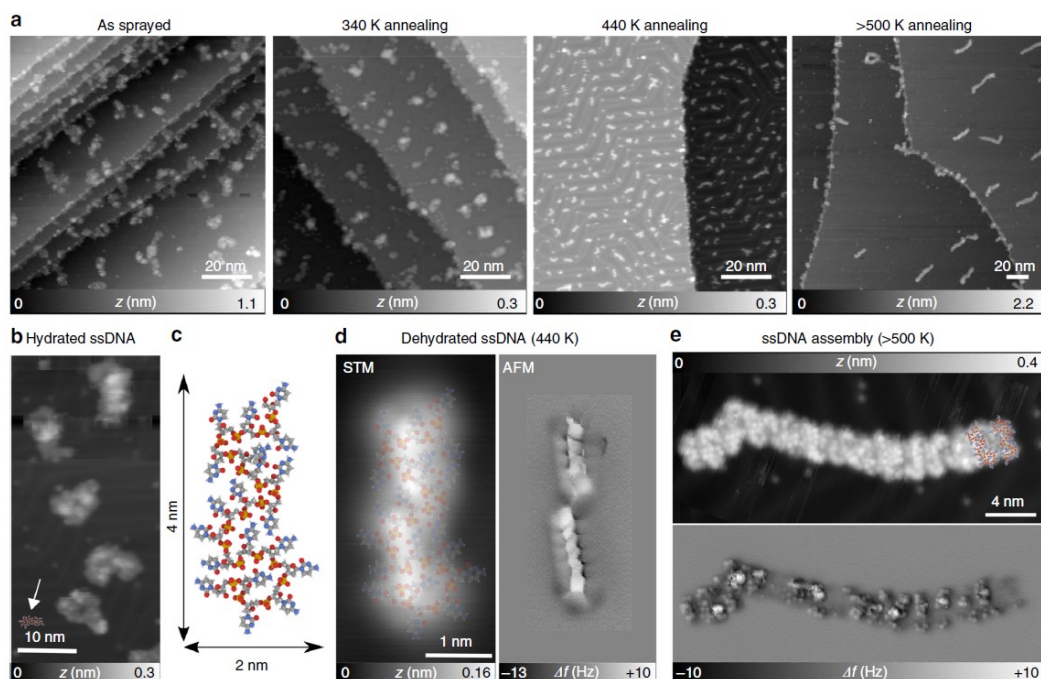


Figure 3.9: Electro spray deposition of single-strand DNA. **a**, *ssDNA morphologies after different annealing temperatures on Au(111).* **b**, *LT STM image of hydrated ssDNA after ESD.* **c**, *View of a ssDNA structure on Au(111) obtained in MD simulations at 400 K.* **d**, *LT STM topography image and corresponding constant height AFM image of a dehydrated ssDNA oligomer after annealing at 440 K.* **e**, *LT STM topography and corresponding constant height AFM images of self-assembled dehydrated ssDNA oligomers after annealing at 500 K.* Reproduced from [150].

High-resolution studies revealed a likely presence of solvent molecules around the oligomers before annealing and the presence of only "dehydrated" ssDNA oligomers after annealing at 440 K as visible in Figures 3.9b-e. MD simulations confirmed the apparent size and revealed the deposition of droplets containing the ssDNA along with solvent and its removal. In addition to the adsorption the mechanical properties of the ssDNA were observed with cryo-force spectroscopy by lifting single oligomers from the surface and confirmed by MD simulations. ESD is, therefore, also well suited for the deposition of thermo-labile and sensitive DNA molecules with sufficient cleanliness for

Chapter 3. Electro spray Deposition

high-resolution studies at LT.

Access to non-metallic surfaces with ESD was first achieved with the deposition of triply fused porphyrins on the bulk insulator KBr(001) [21]. Molecular islands were observed on KBr(001), however, a high surface charge was present after ESD. While an annealing step could reduce this to typical force compensation values, this can induce strong diffusion and changes in the molecules. To enable the study of single molecules and generally avoid an annealing step, the deposition time and molecule concentrations could be reduced to control the coverage. Isolated porphyrins on KBr(001) surface terraces are shown in Figure 3.10a. Their molecular structure was verified to show no breakup during deposition with the high-resolution *nc*-AFM topography image in Figure 3.10b.

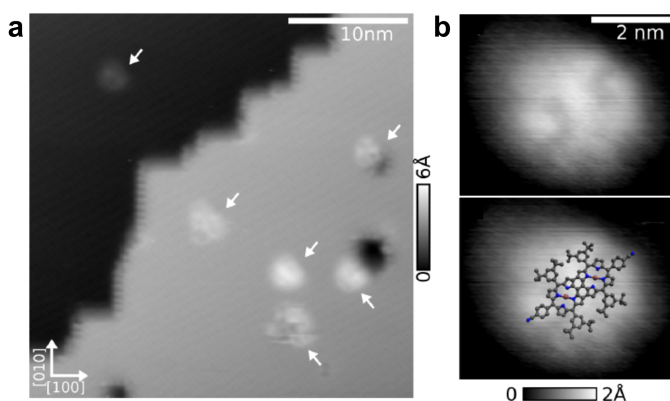


Figure 3.10: Electro spray deposition on bulk insulator KBr(001). *a*, *nc*-AFM topography image of triply fused porphyrins on KBr(001) after ESD. *b*, High-resolution *nc*-AFM topography image of an isolated porphyrin on KBr(001) after ESD along with a molecule model. Adapted from [21].

Notably, small pits, not present before deposition, are visible on the terraces in Figure 3.10a, similar to what is obtained after electron irradiation of such a surface [151]. This points toward a possible influence of ESD on surface morphology and might allow formation of new nucleation sites for molecular adsorption or general structuring of the surface.

Figure 3.10b provides high-resolution *nc*-AFM topography images of a single porphyrin along with a molecular model overlay, showing the molecule to be preserved after deposition. Therefore, providing clear evidence that ESD is well able to provide molecule deposition on non-metallic surfaces.

The chemical integrity of molecules after ESD along with the cleanliness sufficient for studies at low temperatures with CO functionalization of functionalized molecules down to bond level was confirmed in a study of a tetrathiafulvalene (TTF) based dye molecule (structure in Figure 3.11a) [27]. An island of TTFs after ESD is shown in a STM topography image at LT in Figure 3.11b. Five molecules form a star-like assembly due to hydrogen bonding. A sixth molecule could be adsorbed at the site indicated by the white arrow. A small fragment of a molecules is visible instead of a full molecule. The chemical integrity of the five molecules could be ascertained by bond

3.4. Examples of ESD of Molecules

level imaging with a CO functionalized tip in Figure 3.11c. Since other islands show only completed molecules and generally consist of six molecules, this can be assumed to occur rarely. Fragments might, furthermore, already have been present in solution due to break-up caused by the chosen solvents or as was observed in Figure A.1 of the appendix could have been present in the molecule powder.

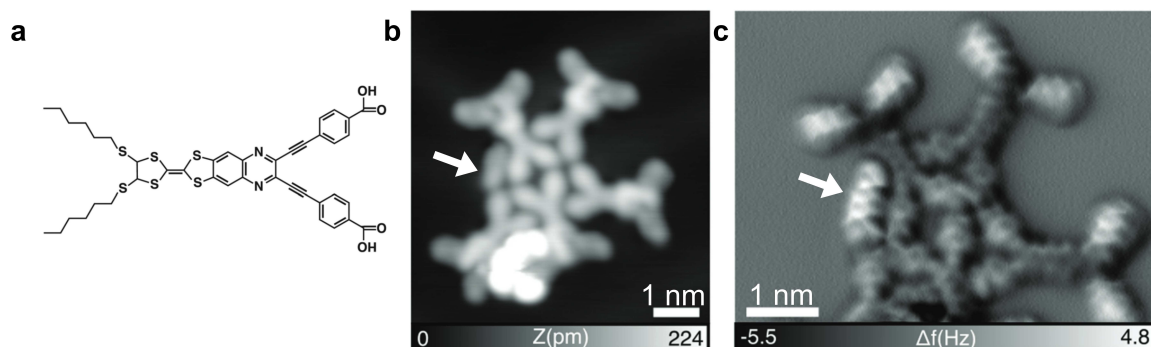


Figure 3.11: Electro spray deposition of dye molecules. *a*, Chemical structure of tetrathiafulvalene (TTF) *b*, High-resolution LT STM topography image of an island of five TTF molecules after ESD. The white arrow indicates a fragment of a molecule. *c*, Corresponding constant height AFM image with a CO functionalized tip confirming the chemical integrity after ESD. Adapted from [21].

Therefore, ESD can provide sufficient cleanliness and stability even for relatively complex molecules with only rare fragmentation being observed.

In summary, ESD is shown to be well suited for the deposition of a variety of complex, well-elongated, and thermo-labile molecules on different types of surfaces while maintaining cleanliness sufficient for high-resolution SPM studies. However, some indications of possible influence of ESD on the adsorption of molecules and the surface have been observed.

3.5 Influence of ESD on Molecular Deposition

The application of an alternate deposition method requires precise knowledge of the influence on adsorption properties and surface modification. The fundamental difference of thermal evaporation and electro spray deposition, already in the state of the molecules - in powder or in solution - necessitates fine comparisons of deposited molecular structures and the containing surfaces. ESD is well-established to yield molecular coverage on surfaces suitable for high-resolution SPM investigations and the presence of pollutants can largely be minimized [16, 19, 27, 127]. However, direct comparisons of a model molecule deposited on different model surfaces, metallic, insulating and semi-conducting, by TE and ESD can provide further insights into the influence of ESD on the adsorption and expected differences. Based on these observations, the interpretation of adsorption properties of molecules only accessible by ESD can be further improved and verified.

In this work, C_{60} , shown in a three-dimensional representation in Figure 3.12a, is chosen as a model molecule due to the ease of evaporation, the generally well-ordered structures obtained and the extensive previous studies. On both metals [152–158] and metal oxide semiconductors [159, 160] two-dimensional C_{60} layers have been formed in previous studies. On ionic crystals or bulk insulators large three-dimensional molecular islands or clusters have been observed [161–165]. In addition, C_{60} was subject to some of the first ESD studies [17, 18] and generally shows reliable and reproducible depositions.

The deposition methods are compared with nc-AFM measurements at RT regarding the resulting adsorption and structure formation of C_{60} at coverages below one monolayer down to single molecules on three model substrate surfaces as published in [34]. The first is Au(111) widely used in SPM, the second the AFM model bulk insulator KBr(001) [162, 166–168], generally used for decoupling of molecules, and last the p-type wide-band gap metal oxide semi-conductor NiO(001) [169]. To exclude any influence of the distinct herringbone reconstruction of Au(111) the spray deposition is repeated on Ag(111). Of interest is, also, the possibility of controlling the molecular coverage by ESD which is precisely possible with TE.

3.5.1 Influence of ESD on Metallic Surfaces

C_{60} is known to form monolayers up to complete coverage on Au(111) surfaces at RT upon deposition via TE [154, 156, 157, 170]. A representative nc-AFM topography image of 0.35 monolayer coverage of an Au(111) surface is shown in Figure 3.12b. Large clean terraces separated by monoatomic steps are visible with distinct molecular coverage in two preferential adsorption locations. First, all the step edges, exemplary shown by the white arrow, are filled with adsorbed C_{60} molecules confirming them to be favorable adsorption sites. Then, after complete occupancy of step edges, newly arriving molecules form islands on the terraces originating from step edges. Islands are observed at the bottom and on top of the step edges, but also on both sides as marked by the black arrow.

A comparable C_{60} coverage, in this case about 0.3 monolayers, after ESD is shown in

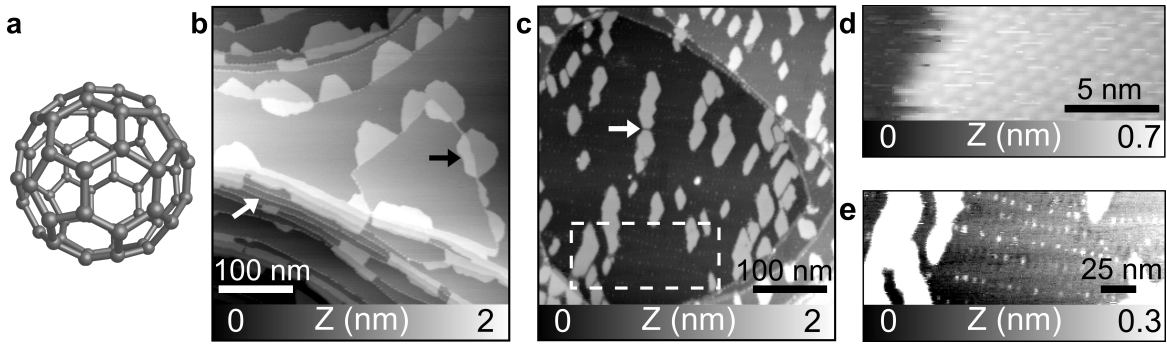


Figure 3.12: Comparison of molecular deposition via thermal evaporation and ESD on Au(111). **a**, Representation of a C_{60} molecule. **b**, Large scale nc-AFM topography image of thermally evaporated C_{60} , showing molecules adsorbed on steps and in islands at steps ($A_2 = 600$ pm, $\Delta f_2 = -40$ Hz). **c**, Large scale nc-AFM topography image of C_{60} after ESD showing adsorption on steps and in islands at steps and on terraces ($A_1 = 5$ nm, $\Delta f_1 = -15$ Hz). **d**, High-resolution nc-AFM image of an island after ESD ($A_2 = 500$ pm, $\Delta f_2 = -60$ Hz). **e**, Zoom on Au(111) surface of marked area of **c** with modified contrast.

the nc-AFM topography image in Figure 3.12c. Here, step edges are also fully covered with C_{60} molecules. This means they are still the most favored adsorption sites on the surface. Terraces with monoatomic steps are observed indicating minimal influence of the spray on the surface morphology. Islands are observed originating from both the terraces or isolated on the surface. Thus, further nucleation sites have to be present on the surface, in addition to the previously mentioned step edges. This might be due to defects generated by the spray deposition allowing trapping of molecules and, thereby, island nucleation in the middle of the terraces. The hexagonal adsorption geometry, however, is preserved as visible in the high-resolution topography image in Figure 3.12d confirming an equivalent lattice arrangement of 1 nm after both TE and ESD.

The number of defects induced by ESD has to be quite high and their separation low, as shown by the number of islands and the small distance between them. This is exemplified by the two isolated islands shown in the topography image in Figure 3.13a. There, the islands are both formed on the terrace, in contrast to a third island at a step, but each separated from the others by a few nanometers. The separation is verified by the zoomed torsional frequency shift image in Figure 3.13b, showing the molecules forming the islands but no connection between them. The defects could act as nucleation sites for the islands on the surface, resulting in an increased density but lower average size of such islands, decreasing from about 1500 nm² for 0.35 monolayers after TE to about 600 nm² after ESD with only slightly less molecules present on the surface.

On close inspection of the terraces after ESD, surface pollution can be found, pronounced especially as small dots, forming almost straight lines as is visible from the marked area of Figure 3.12c shown with enhanced contrast in Figure 3.12e. Here, the reason for the line like structure is revealed as the dots are adsorbed to the elbows

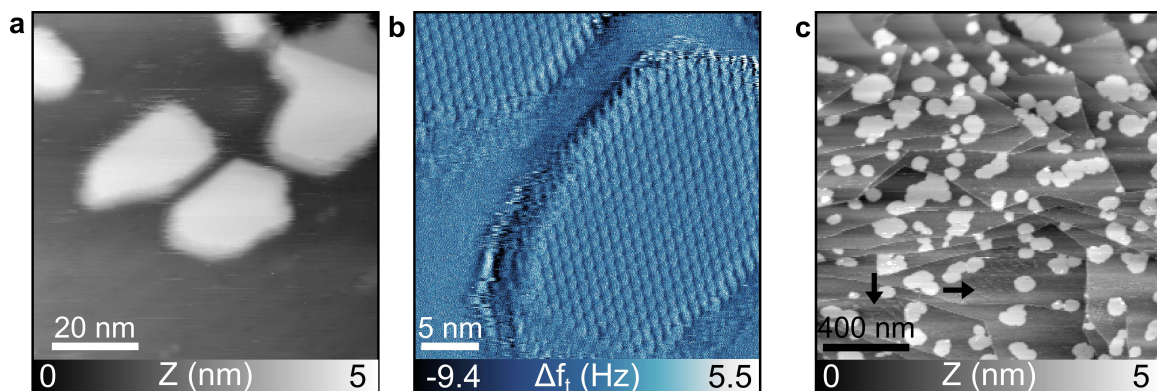


Figure 3.13: Adsorption properties after ESD on Au(111) and Ag(111). **a**, *nc-AFM topography image of C_{60} on Au(111) after ESD showing isolated islands on a surface terrace ($A_2 = 600$ pm, $\Delta f_2 = -25$ Hz).* **b**, *Zoomed torsional frequency shift image of the small separation between C_{60} islands after ESD ($A_2 = 600$ pm, $\Delta f_2 = -60$ Hz, $A_t = 50$ pm).* **c**, *Large scale nc-AFM topography image of C_{60} on Ag(111) after ESD. Adsorption occurs similarly to Au(111) on steps and in islands at steps and on terraces ($A_2 = 800$ pm, $\Delta f_2 = -25$ Hz).*

of the HB, known as favorable adsorption sites [171, 172]. The HB elbows are known to present defects that can trap solvent molecules. C_{60} molecules are, however, not adsorbed there, since no similar adsorption was found after thermal evaporation.

To investigate the influence of the distinct HB on the adsorption upon spray, ESD was also performed on Ag(111). A resulting large scale topography image is presented in Figure 3.13c. Multiple large terraces separated by monoatomic steps are visible. Similarly to Au(111), first step edges are fully decorated with C_{60} molecules, again showing them to be favored adsorption sites. Then, islands form on both the terraces from steps and isolated on the surface. On Ag(111) the islands generally show a more round shape and are less likely isolated, indicating a lower density of defects and accordingly fewer nucleation sites. On inspection of the terraces two areas marked by black arrows, where lines are visible, are observed. While not as prominent or ubiquitous as on Au(111), lines can still be generated. Here, however likely more by chance and due to spray conditions than by predefined favorable adsorption sites.

The influence of ESD on the adsorption properties of C_{60} are, thus, quite limited. The adsorption geometry and island formation is generally preserved, but new adsorption sites on terraces are formed allowing isolated islands to be grown on the terraces.

3.5.2 Influence of ESD on an Insulating Surface

Thermal evaporation of C_{60} molecules on bulk insulators generally results in the formation of large islands with multilayers forming before complete coverage [161, 162, 173]. A representative surface is visible in the large scale topography image in Figure 3.14a. Large and clean terraces separated by multiple mono- to diatomic steps are observed. Similar to the evaporation on Au(111) islands are formed along step edges. Noticeably, their edges exhibit preferential directions in accordance with the hexagonal lattice of

3.5. Influence of ESD on Molecular Deposition

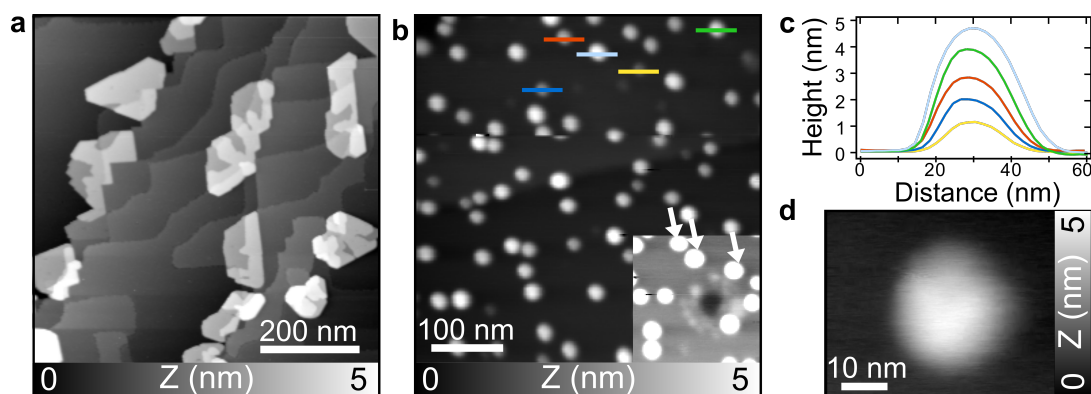


Figure 3.14: Comparison of molecular deposition via thermal evaporation and ESD on KBr(001). **a**, Large scale nc-AFM topography image of C_{60} islands on KBr(001) after TE ($A_1 = 4$ nm, $\Delta f_1 = -5$ Hz), **b**, after ESD ($A_1 = 8$ nm, $\Delta f_1 = -8$ Hz). Superimposed is the same area with a modified contrast revealing a modification of the surface. **c**, Height profiles along colored lines of **b**. **d**, Close-up topography image on an island of **b** ($A_1 = 8$ nm, $\Delta f_1 = -8$ Hz).

C_{60} . Their height reaches up to three monolayers with dewetting visible in the more round shape of the second and third layer [161, 163]. Additionally, the step edges remain mostly uncovered indicating a lower molecule-surface interaction compared to the metallic case. As a result, longer diffusion lengths are observed. The distance between islands is, therefore, larger and a more 3D growth mechanism is obtained.

ESD of molecules on insulating substrates and especially ionic crystal surfaces like KBr(001) is more challenging. The deposition of charged particles, as occurring during ESD, can induce charging of the surface, since the back electrode, that would evacuate the charges, is separated from the surface by a few millimeters. This can influence the deposition via ESD by leading to a rejection of further charged species, the surface local charge, and the island formation [21]. These effects can be mitigated by a gentle annealing during deposition, leading to a reduction of the surface charge. However, to exclude any influence from such procedure on the adsorption and surface, in this work all treatment of the samples was foregone. Instead, the spray deposition was performed with comparatively low flux (below 100 $\mu\text{l/h}$) over a longer time to reduce charge accumulation. In addition, the imaging was performed a few hours after ESD to improve scan conditions by allowing for charge reduction [69, 174].

In a first step, similar C_{60} coverage to what was obtained via TE was targeted resulting in the topography image shown in Figure 3.14b. Large terraces with high round islands dispersed widely over the surface are observed. The islands show a more round shape, as is also visible in the zoomed image in Figure 3.14d, in contrast to the preferential edge directions along the hexagonal lattice observed after TE. In comparison to the islands after TE with heights of about three monolayers, the height after ESD is more broadly distributed. This is illustrated by the profiles along the marked lines in Figure 3.14b presented in Figure 3.14c, reaching from one monolayer to at least five. Even though the number of C_{60} molecules is relatively similar to TE, a

Chapter 3. Electro spray Deposition

much higher 3D growth and lower contact area is observed along with a more spherical island shape. The average surface contact area of an island – the area of the surface covered by the first layer of an island – is reduced from 12000 nm² for TE to only 1200 nm² after ESD. The spherical shape of the island could be assumed to be due to charging of the surface, however KPFM measurements revealed no abnormal charging. Thus, either the charge could not be detected because of measurement limitations or another mechanism underpins the different shape.

Additional to C₆₀ deposition, a much more significant impact on the surface is observed for KBr compared to metals. This can be seen on the terraces and especially in the contrast enhanced topography image inset in Figure 3.14b, where crater-like pits are visible with material aggregates around them. Dependent on the spray deposition the craters are more or less pronounced, a zoom on a larger crater reaching three layers deep into the surface is shown in Figure 3.15a. The crater was generated by specifically modifying the spray parameters to induce strong impact on the surface with more droplets and higher speed. Surrounding the crater are rectangular islands with

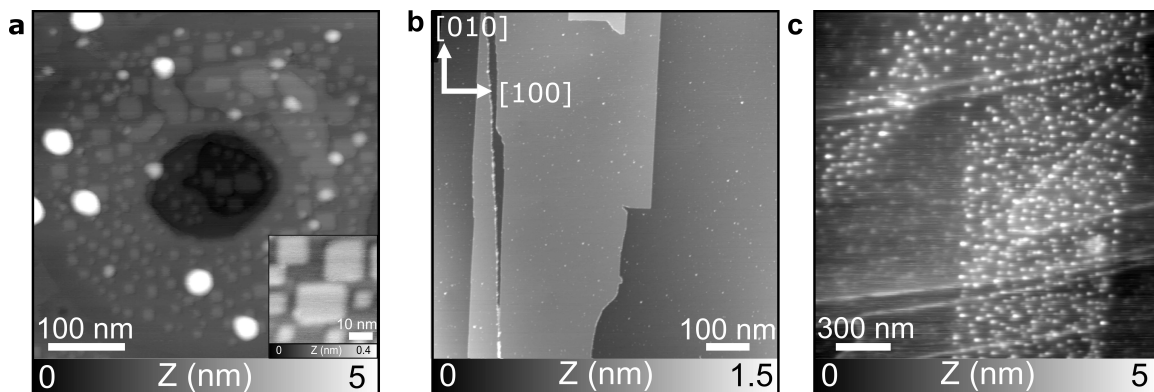


Figure 3.15: Different coverage levels achieved by ESD. a, *nc-AFM topography image of a KBr(001) surface modified by ESD. A three layer deep crater is formed. Inset is a zoom on the islands around the crater ($A_1 = 5 \text{ nm}$, $\Delta f_1 = -8 \text{ Hz}$).* **b,** *nc-AFM topography image of C₆₀ on KBr(001) with low coverage ($A_2 = 800 \text{ pm}$, $\Delta f_2 = -30 \text{ Hz}$),* **c,** *with high coverage ($A_2 = 800 \text{ pm}$, $\Delta f_2 = -30 \text{ Hz}$).*

few molecular islands mixed with them. From the inset, the material forming can be identified as KBr likely removed upon impact and creation of the crater. Volume of the crater was measured to be about 4000 nm³. This compares reasonably well to the total volume of the islands of about 7000 nm³, when considering the intermingling of solvent to the islands and the probable presence of smaller and less visible craters. Thus, KBr, removed upon impact, likely diffuses in the close vicinity of the impact and forms such islands typical for ionic crystals. Similar pits and modifications have been created by electron and ion bombardment [151, 175, 176], low plasma exposure [177], thermal evaporation of alkali halides [178] and in previous spray experiments on ionic crystal surfaces [21, 179]. Islands and pit edges can allow the trapping of molecules and, thus, their creation has been studied previously [167, 177, 180–182]. A clear identification of what impacts the surface during ESD is not possible, however, droplets of solvent

3.5. Influence of ESD on Molecular Deposition

possibly containing C_{60} molecules, which did not sufficiently evaporate and undergo Coulomb fission and ion generation, are most probable.

By reducing the flow rate and deposition time of ESD, significantly lower coverage can be achieved as shown in Figure 3.15b. Large, clean and mostly unmodified terraces with clean step edges are observed. On top of the terraces small clusters of C_{60} molecules are present, indicating a low diffusion contrary to after TE. This also points towards the formation of defects in the surface, albeit much smaller in scale, which allow trapping of molecules and formation of new nucleation sites. At slightly higher coverages and especially at the edge of the spray area, more pronounced coverage and less cleanliness can be observed. In the topography image in Figure 3.15c large terraces with covered step edges – most likely solvent – and a large presence of small clusters can be seen. The clusters are distributed in a well-defined area with a sharp edge, indicating a droplet deposition on this specific area of the surface.

The observed assembly formation and surface modification, consequently, differs significantly after deposition via TE and ESD. Modifications due to spray result in smaller, but higher islands with no preferential edge directions formed at and away from step edges. Lower coverage after spray allows the formation of small isolated clusters down to single molecules. Major modification of the surface can be observed at higher coverage and deposition rate after ESD, while low coverage shows similar surface conditions to TE.

3.5.3 Influence of ESD on a Semi-conducting Surface

NiO is of interest because of its properties as a p-type wide-band semi-conductor for photovoltaic, especially dye-sensitized solar cells, but only few previous investigations of molecular depositions have been performed [86, 87, 183]. Due to the previously mentioned limitation of TE and the complexity of certain dye molecules, ESD can provide interesting possibilities here and first spray experiments were performed in the study in [169].

Figure 3.16a shows a topography image of NiO(001) after the deposition of C_{60} molecules on NiO(001) via TE [169]. Large terraces marked by visible hole defects due to the high reactivity of the surface are observed [183]. Irregular shaped islands without any preferential orientation or edge direction are noticeable on the terraces. Their size correlates to the size of their terraces, indicating molecular diffusion on top of terraces but not over steps. Thus, more molecules are present on larger terraces thanks to the larger adsorption area. Furthermore, small clusters are visible dispersed over the terraces possibly formed by small clusters of molecules.

A zoom on top of such an island, shown in Figure 3.16b, reveals the typical hexagonal lattice of C_{60} to be present inside. As previously observed [169], after ESD only small clusters of C_{60} can be observed on the NiO(001) surface as presented in the topography image in Figure 3.16c. The presence of large terraces with only minimal defects, should analogous to TE facilitate adsorption of many C_{60} molecules on them. Consequently, large islands should be formed as a result of the high diffusion observed after TE. A possible explanation is the height of the clusters measured as a profile along the blue line. It is significantly lower after ESD in comparison to after TE, as shown in the

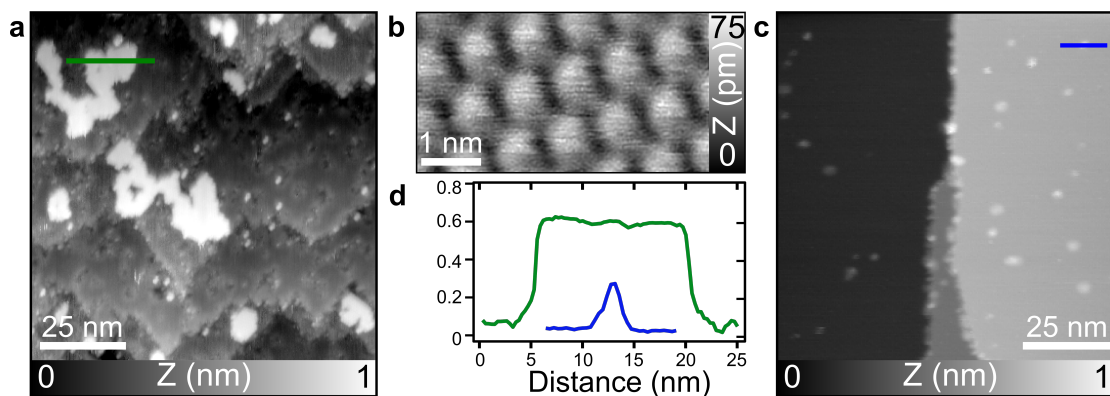


Figure 3.16: Comparison of molecular deposition via thermal evaporation and ESD on NiO(001). **a**, *nc-AFM topography image of C_{60} on NiO(001) after TE. Molecule islands are visible on terraces. ($A_1 = 8$ nm, $\Delta f_1 = -8$ Hz). **b**, *High-resolution nc-AFM topography image showing molecular resolution atop an island of C_{60} after TE.* **c**, *nc-AFM topography image of small clusters of C_{60} on NiO(001) after ESD ($A_2 = 800$ pm, $\Delta f_2 = -10$ Hz).* **d**, *Profiles measured along the green and blue lines in **a** and **c**, respectively. Adapted from [34, 169].**

profile in Figure 3.16d. This indicates that the cluster or single molecules might be trapped in defects formed immediately upon landing. Since for TE the diffusion is not reduced, this has to be induced by the spray, analogously to the adsorption after ESD for Au(111) and KBr(001).

Modifications outside of the possible small defects trapping the molecules are not observed.

3.6 Summary

In this chapter a comparison of the most common method of molecular deposition in UHV, thermal evaporation and a solution based alternative, electro-spray deposition, was presented.

First, thermal evaporation and its limitation of thermal lability and molecule size were introduced, then various possible alternate methods reaching from rapid heating to contact based deposition and ex vacuo located solution based methods were discussed along with their advantages and drawbacks. Next, the principles of the chosen method ESD, the spray jet formation, the desolvation and different theories of ion generation were discussed. Then, the setup facilitating the deposition of the molecules from solution is described, consisting of an emission setup in ambient conditions, a power supply and a four stage pumping setup. Finally, to verify the possibility and influence of using ESD as an alternative for TE, depositions of C_{60} molecules were performed on three common model surfaces, Au(111), KBr(001) and NiO(001). Depositions showed that high cleanliness of the surfaces can be obtained for ESD, however, various degrees of adsorption differences and surface modification have to be taken into account when employing ESD. Most notably, new nucleation sites, likely formed

by defects in the surface from the deposition, are generated on all three surfaces, allowing island or cluster formation independent of the most common adsorption site, the step edges. If tighter control over the modification is achieved, this could be used for nanopatterning of surfaces with or without molecules.

In conclusion, ESD was shown to be a well-established and suited molecule deposition method in UHV often providing equivalent results to TE with cleanliness sufficient even for high-resolution SPM measurements, however the influence of ESD on the adsorption and surface has to be taken into account especially on non-metallic surfaces.

Thermal Expansion by Alkyl Chain Motion

THE access to new molecules on surfaces provided by ESD allows the investigation of new functional properties in UHV based on previously less accessible complex molecules with fragile functional groups, like thermo-labile alkyl chains. Of particular interest is, thereby, the thermal response of molecules and their assemblies due to ubiquitous presence of heat as stimulus in nature. Especially, applications of new materials in mechanical or optical uses are strongly influenced by their thermal behavior.

The coefficient of thermal expansion (CTE) α per K^{-1} , positive if a material expands with heat, and negative if the material shrinks, describes this response by considering the initial length l_0 and the change in length ΔL and in temperature ΔT [9, 184]:

$$\alpha = \frac{\Delta L}{l_0 \times \Delta T}. \quad (4.9)$$

This chapter first focuses on the thermal response in molecular materials and some possible mechanisms studied in literature. Then, with a combination of STM and nc-AFM measurements at 5 K and 300 K the structural response of a two-dimensional supramolecular network of a large shape persistent polyphenylene molecule equipped with six dodecyl chains upon temperature variation is studied on Au(111). A giant thermal expansion is observed and with molecular dynamics simulations attributed to a mechanism originating from increasing mobility of the alkyl side chains with temperature forcing an expansion of the network, as published in [22].

4.1 Thermal Expansion of Molecular Materials

Molecular materials and especially supramolecular assemblies can present exceptional response to external stimuli, most commonly light, heat or mechanical stress. This is facilitated by their inherent flexibility and for supramolecular cases weak non-covalent bonding. Significant variations in adsorption, conformation or packing can be achieved by light, mechanical compression or chemical composition [3, 185–192]. Abundant in

Chapter 4. Thermal Expansion by Alkyl Chain Motion

applications of materials are changes in heat and, thus, the influence of their thermal expansion is important [9, 184, 191, 193].

Thermal expansion in molecular materials and polymers can occur in various ways. Intrinsically a positive CTE exists for materials according to the first law of thermodynamics and the Lennard-Jones potential energy curve [9]. Increased temperatures provide high kinetic and potential energies to molecules and, thus, induce thermal expansion. For typical materials this amounts to CTEs of $\alpha \sim 0 - 20 \times 10^{-6} \text{ K}^{-1}$ for inorganic materials, $\alpha \sim 13 \times 10^{-6} \text{ K}^{-1}$ for unfunctionalized hexabenzocoronene and $\alpha \sim 55 \times 10^{-6} \text{ K}^{-1}$ for polystyrene [184, 194]. Notably, the large variety of molecules and structures allows specific design of thermal expansion, both in negative [195, 196], in positive or in abnormal ways [9, 184], based on a multitude of mechanisms, with a few summarized in Figure 4.1 [184].

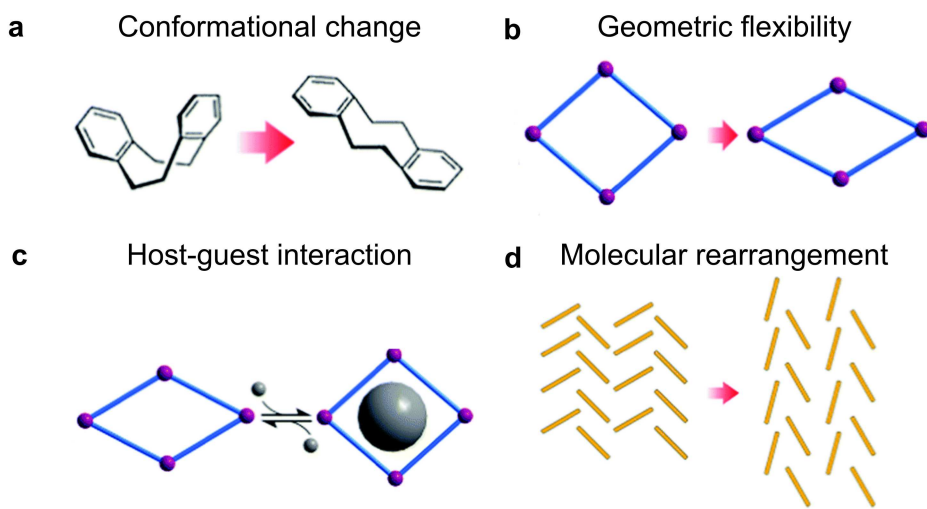


Figure 4.1: Mechanisms of thermal expansion. Thermal expansion both with negative or positive CTE in molecular materials can among others be driven by **a**, conformational changes, **b**, geometric flexibility, **c**, host-guest interactions, and **d**, molecular rearrangement. Adapted from [184].

First, thermal expansion can be based on conformational changes [197–200]. Macromolecules usually exhibit a high degree of flexibility and, thus, susceptibility to external stimuli, like ultraviolet radiation or, as desired in this work, heat. Meaning they change their shape – their conformation – upon the stimulus, which can lead to an expansion or shrinking of the molecule volume or length and, thus, to negative or positive thermal expansion. This was used in polymer films of s-dibenzocyclooctadiene (DBCOD), which exhibited an exceptional contraction in tensile measurement with a CTE up to $\alpha_{DBCOD} = -1200-2400 \times 10^{-6} \text{ K}^{-1}$ [199, 200]. DBCOD undergoes a conformational change from a twist-boat to a chair configuration, as shown in Figure 4.2, driving such shrinkage [199].

Another possible mechanism of thermal expansion is geometric flexibility, usually present in porous structures, most commonly flexible metal-organic frameworks or soft

4.1. Thermal Expansion of Molecular Materials

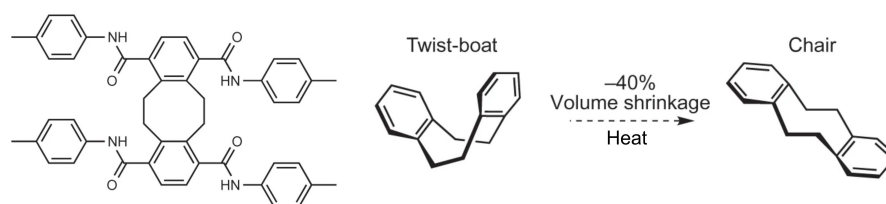


Figure 4.2: Thermal expansion by conformational changes. *Molecular scheme of DBCOD illustrating the change from a twist-boat to a chair conformation due to heat stimulation. Adapted from [199].*

porous crystals [201–206]. Upon external stimuli, i.e. heat, these materials possessing crystalline ordered networks and structural transformability undergo dynamic framework deformations resulting in thermal expansion [207]. A striking example is the molecular crystal perdeuterated methanol monohydrate ($\text{CD}_3\text{OD}\cdot\text{D}_2\text{O}$) [202]. As seen in Figure 4.3a, the structure looks like a scissor jack. With thermal changes, the geometry of the scissor jack changes, undergoing a large expansion in one direction and shrinking in the other, resulting in a coupled positive and negative thermal expansion along the two axes. Similarly, the 3D hinged metal-organic framework assembled from *meso*-tetra(4-pyridyl)porphine and CdI_2 exhibits a lattice fence, which allows drastic thermal expansion as shown in Figure 4.3b [203].

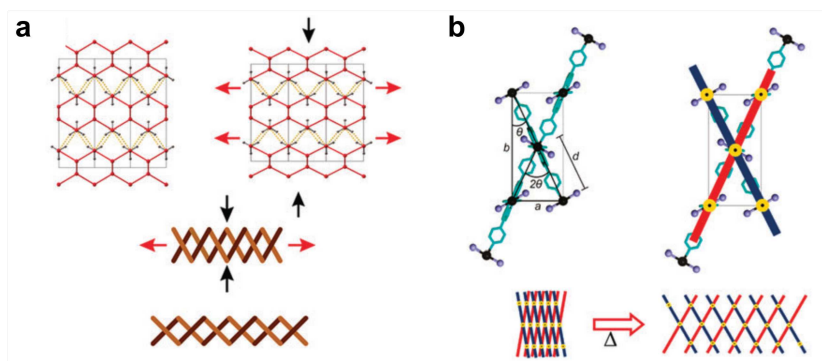


Figure 4.3: Thermal expansion by geometric changes. *a, Schematic representation of the scissor jack and hinge like geometric change in $\text{CD}_3\text{OD}\cdot\text{D}_2\text{O}$ and b, a 3D hinged metal-organic framework. Adapted from [202, 203].*

Exceptional thermal expansion can, furthermore, be achieved by host-guest interaction [208–213]. The guest, thereby, can strongly influence the thermal expansion coefficient from negative to positive or vice versa or restrict the expansion along one axis and induce it in another [214]. In Figure 4.4a the expansion of a porous crystal, the host framework, occurs along the red bars. Upon inclusion of guest dimers, the expansion is changed. The host (yellow spheres) forces the network to expand along the green spires by acting like a jack, when the dimers increase their separation upon thermal changes [212], as visible in Figure 4.4b.

Finally, thermal expansion can be obtained by rearrangement of the packing of

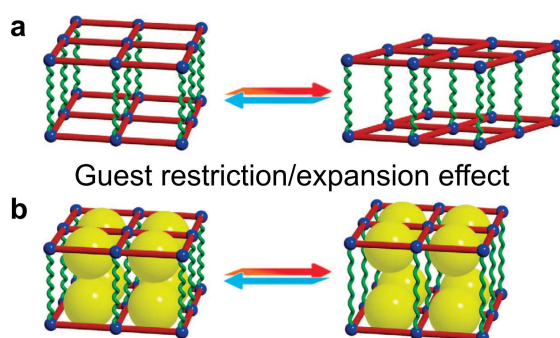


Figure 4.4: Thermal expansion by guest-host interaction. *a*, Thermal expansion of the host porous crystal without guest. *b*, Influence of the guest on the thermal expansion. The guest behaves like a jack by changing the separation between its dimers (yellow spheres), forcing deformation of the host framework in a different direction. Adapted from [212].

molecules in soft materials bound by supramolecular interactions, like van der Waals forces, π - π interactions or hydrogen bonds [184]. Generally, these bonds are weak and the materials, thus, quite sensitive to external stimuli, like heat, allowing large thermal expansion effects [215–218].

An interesting example is (S,S)-octa-3,5-diyne-2,7-diol, which was found to show bi-axial negative thermal expansion, as shown in Figure 4.5a [215]. The molecules form

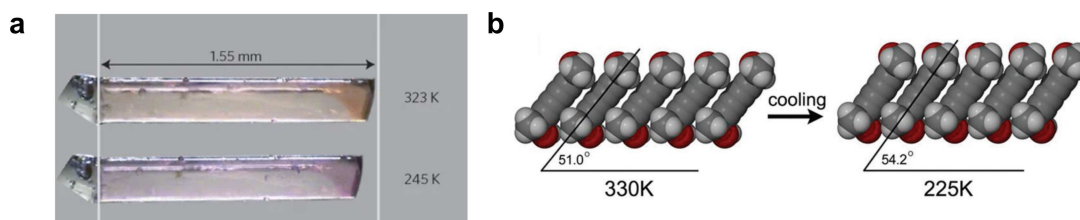


Figure 4.5: Thermal expansion by molecular rearrangement. *a*, Photomicrographs recorded at 323 and 245 K of a (S,S)-octa-3,5-diyne-2,7-diol crystal showing large negative thermal expansion. *b*, Perspective view of the packing rearrangement upon cooling. Adapted from [215].

a 3D network by stacking next to each other via hydrogen bond connection. Due to the dumbbell shape of the molecules and the hydrogen bond, the molecules can, upon cooling, change their tilt angle resulting in the observed thermal expansion behavior as can be seen in Figure 4.5b. Similar thermal expansion was reported for halogen-bonded complexes, where weakening of halogen bonding results in a rearrangement of the molecule packing [218].

Two-dimensional materials exhibiting thermal expansion can allow access to new mechanisms and applications because of the confinement imposed by the surface they are adsorbed to. Additionally, this allows high-resolution investigations in real-space with nc-AFM, STM and constant height AFM to reveal and explain the precise in-

teractions and mechanism driving expansion. Therefore, new control and induction of thermal expansion could be achieved. Based on the access to new functionalities provided by ESD a new mechanism based on 2D supramolecular materials combining their aforementioned flexibility with the inclusion of alkyl chains to provide high thermal expansion, while maintaining the conformation and phase of the molecular system, is investigated in the following.

4.2 Single Spoked Wheel Molecules

The molecule chosen to investigate the thermal response of molecular assemblies containing alkyl chains is a purely sp^2 -hybridized shape persistent polyphenylene spoked wheel molecule equipped with six dodecyl side chains [219]. The molecule was synthesized at the Max-Plank Institute in Mainz [219]. Its side chains are attached to the ends of the spoke axes, which together with the sides form the core of the molecule, as shown in Figure 4.6a.

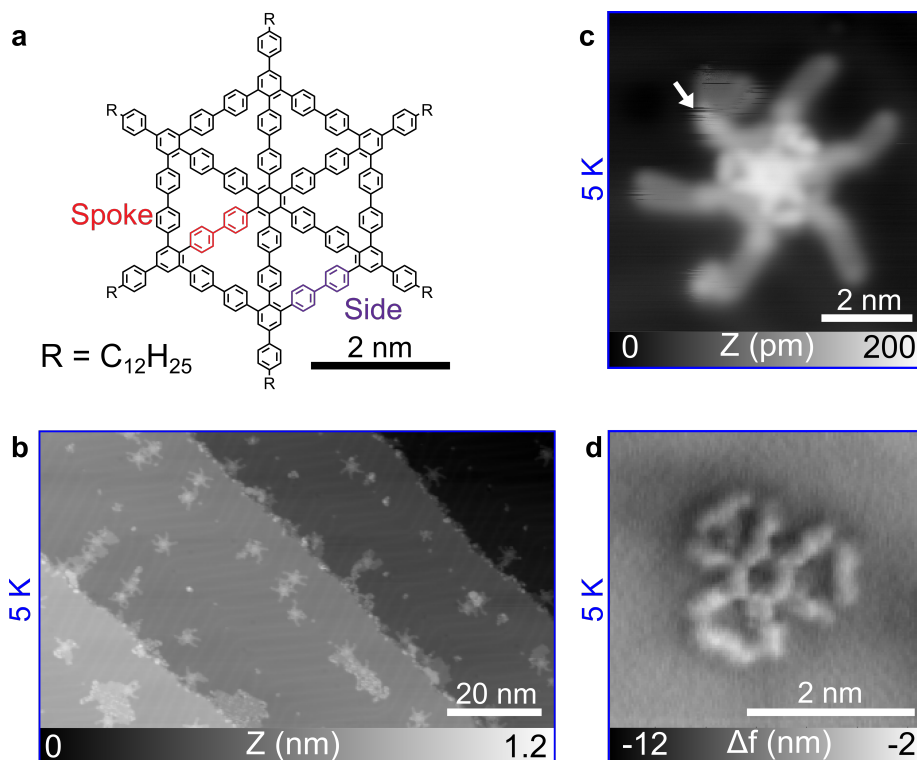


Figure 4.6: The spoked wheel molecule. **a**, Chemical structure of the spoked wheel molecule equipped with dodecyl chains. **b**, Large scale LT STM topography image of a surface without post-annealing after ESD, showing SW molecules at steps and isolated on terraces ($I = 1$ pA, $V_{Bias} = -800$ mV). **c**, LT STM topography image of a single SW molecule on Au(111) at 5 K. A height modulation in the core is visible, three sides and the spokes appear higher than the other sides and chains ($I = 1$ pA, $V_{Bias} = -380$ mV). **d**, Constant height AFM image of the core of the SW molecule acquired with a CO-terminated tip at 5 K. Six spokes, but only three sides are visible.

To safely deposit the SW onto Au(111) surfaces, ESD was applied. Depositions occurred at RT and were for later measurements always followed by an annealing step at 450 K to minimize solvent pollution. Even thereafter, single isolated SW molecules are observed on the surface indicating low diffusion. This makes the SW well suited for investigating the thermal response of supramolecular assemblies, since observed expansion would solely depend on supramolecular effects and not on single molecules.

A large scale topography image observed before the annealing step is shown in Figure 4.6b. Visible on reasonably clean terraces are isolated molecules along with some aggregates of solvent pollution. Step edges, previously shown as preferential adsorption sites, are mostly decorated with small amounts of solvent as well. A single isolated molecule on the Au(111) surface is shown in a close-up STM image in Figure 4.6c at LT. The molecule is observed intact with the core and spokes clearly visible, while the chains appear somewhat fuzzy (white arrow) due to their relatively higher mobility upon the influence of the scanning tip. Notably, inside the core the spokes and sides exhibit a slightly different contrast, indicating corrugation inside the core. This is further confirmed in the corresponding CO functionalized constant height AFM image in Figure 4.6d. Here, each spoke of the molecule core is visible, however only half of the sides are resolved. The dodecyl chains are also not resolved in AFM, but present in STM, indicating closer adsorption to the surface.

The threefold symmetry of the molecule on the surface as opposed to the chemical structure occurs because of steric hindrance between the different domains of the molecule, spokes and sides. The central aromatic ring of the molecule has to be horizontal. This results in steric hindrance of the hydrogen atoms of the spokes close to the center and, thereby, a tilting of the spokes. Depending on the tilting of the outer ring of the spokes, the sides can either lie flat or point upright, increasing surface interaction or reducing steric hindrance. In AFM they, therefore, can either be resolved or not.

4.3 Molecular Assembly Thermal Response

Upon ESD different aggregates were observed on the surface, reaching from single molecules, as shown above, to well extended assemblies spanning over multiple terraces. The thermal response of SW assemblies was studied on extended networks with at least 200 nm width and length, chosen to be of similar size to avoid packing or compression influences of the domain size on the lattice parameters. The depositions, thereby, were always performed at RT and then the samples either investigated in the RT system with nc-AFM or cooled to 5 K in the LT system for study with STM and AFM.

Figures 4.7a and b show STM and nc-AFM images of such networks acquired at 5 K and 300 K, respectively. At both temperatures individual SW molecules are observed as bright protrusions in the assemblies forming long-range hexagonal networks on two terraces. Also visible is a small amount of remaining solvent both on the steps and on the terraces.

As visualized in the profiles in Figure 4.7c obtained along the lines marked in Figures 4.7a and b, the molecule spacing of the networks shows a significant difference.

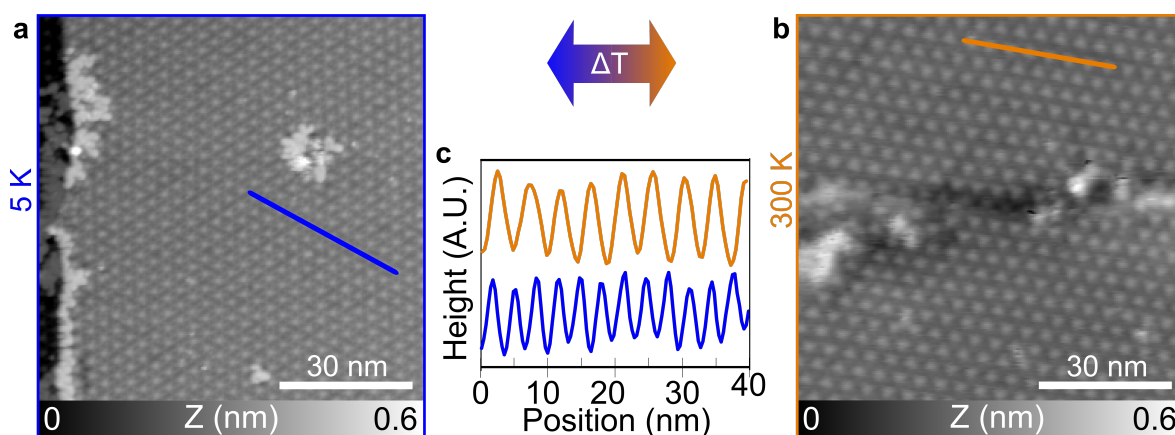


Figure 4.7: Thermal response of a SW molecular assembly on Au(111). **a**, Large scale STM topography image of a SW molecular assembly at 5 K ($I = 1$ pA, $V_{Bias} = -300$ mV). **b**, Large scale nc-AFM topography image of an assembly at 300 K ($A_2 = 400$ pm, $\Delta f_2 = -19$ Hz). **c**, Profiles along marked lines of **a** and **b** indicating the lattice spacing change.

Measurements of the lattice parameters reveal an increase from $a_{5K} = 3.5 \pm 0.2$ nm in the assembly observed at 5 K to $a_{300K} = 4.5 \pm 0.2$ nm at 300 K, corresponding to a lattice shrinking of ~ 22 % for smaller temperatures. Of note is the preservation of the hexagonal adsorption geometry between the two temperatures, suggesting the absence of any structural phase transition, as will be discussed in more detail with measurements for a similar molecule in Chapter 5.

The thermal expansion coefficient of SW assemblies on Au(111) is, thus, determined as $\alpha_{SW,exp} = 980 \pm 110 \times 10^{-6} \text{ K}^{-1}$, two orders larger than the expansion coefficient of the Au(111) substrate of about $\alpha_{Au(111)} = 13 \times 10^{-6} \text{ K}^{-1}$ and the CTE of a molecular assembly of unfunctionalized HBC $\alpha_{Au(111)} = 14 \times 10^{-6} \text{ K}^{-1}$ [194].

4.4 Single Molecule Thermal Response

To reveal the mechanism of expansion underlying the giant thermal expansion observed for the SW assemblies, in a first step, the thermal response of a single SW molecule was numerically investigated in microsecond long all atom MD simulations on an Au(111) surface at different temperatures (5 K, 300 K, 420 K, 450 K)¹. To provide a starting configuration, a relaxed molecule configuration was generated without the presence of a surface. Then, the final configuration of SW was positioned 1 nm from the Au(111) and allowed to adsorb to the surface in a 10 ns long MD simulation performed at 300 K. The temperature of 450 K, equal to the annealing temperature, was chosen to reduce the time needed to reach equilibrium, which will especially in later simulations play an important role.

Figure 4.8a shows snapshots of the final configurations of the SW molecules for each simulated molecule after 1 μ s. As can be seen in relation to the center lines the

¹<https://www.nature.com/articles/s43246-020-0009-2#Sec18>

Chapter 4. Thermal Expansion by Alkyl Chain Motion

displacement of the molecules is marginal for all temperatures, further confirming the low mobility observed in the experiments even during the annealing step. Importantly, the side chains are significantly more mobile at higher temperatures, as visible in the straighter position observed for 5 K in comparison to the increasingly more tilted and repositioned chains for 300 K, 420 K and 450 K.

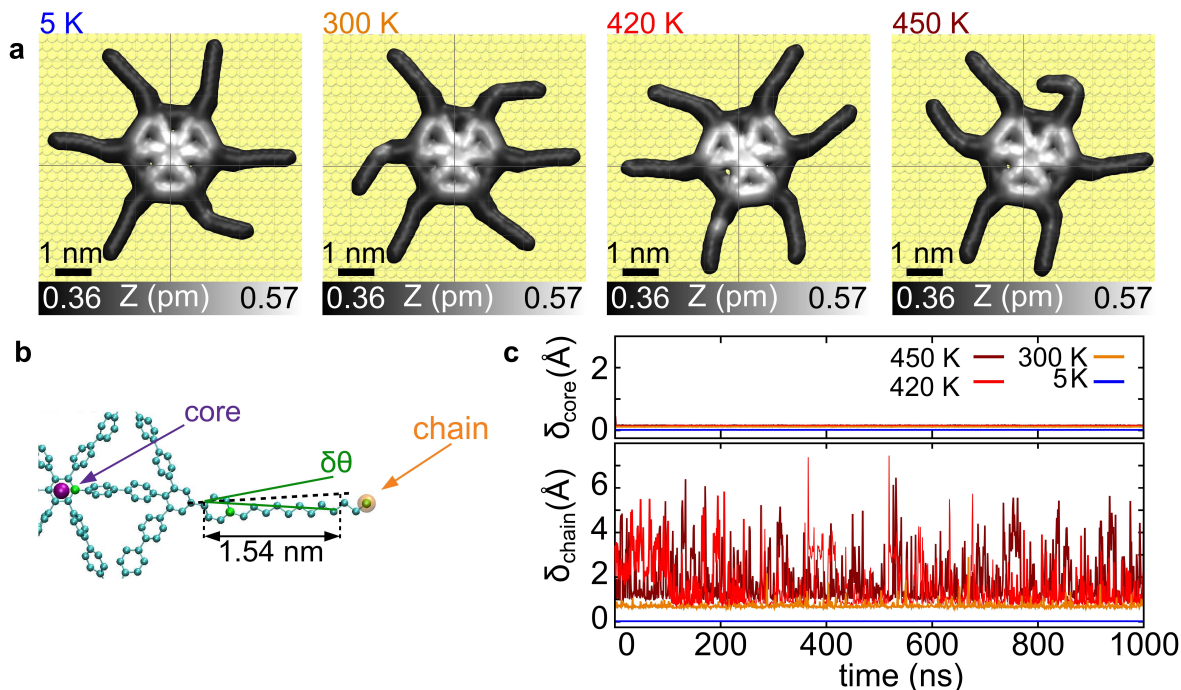


Figure 4.8: Thermal response of SW core versus chains based on MD simulations. **a**, Final configurations and positions of single SW molecules after $1 \mu\text{s}$ MD simulations at different temperatures. **b**, Schematic illustration of representative positions of the molecule parts (core and chains). **c**, Standard deviation of the mean square displacement (MSD) - δ_{core} - of the SW center of mass as a function of time at different temperatures (**top**). Standard deviation of the MSD - δ_{chain} - of a SW chains in relation to time at different temperatures (**bottom**).

In order to characterize the influence of these two distinct behaviors of the molecule core and chains, the mean square displacement (MSD) of the core and the chains was used separately. The core is, thereby, represented by the center of mass of the central aromatic ring, as marked by the purple bead in Figure 4.8b. All chains are considered to be identical and represented by its last carbon atom, marked with an orange bead. To avoid influence of single displacement events that occurred at the beginning of the simulations to improve the registry of molecule and surface, the standard deviation of the MSD, hereafter denoted as δ , is considered which provides a better representation of the observed mobility behavior.

As already seen in the snapshots in Figure 4.8a the mobility of the core and, thus, the diffusion of the molecule, is minimal for all temperatures. Only a marginal increase remaining close to zero in the standard deviation of MSD δ_{core} , plotted in Figure 4.8c is observed for 300 K, 420 K and even 450 K. This is most likely related to the large

4.4. Single Molecule Thermal Response

molecular contact area with the surface. In comparison, the chains, as shown in the lower plot in Figure 4.8c, show much higher mobility δ_{chain} , and more importantly in contrast to the core fluctuations which remain virtually unchanged close to zero, fluctuations of the chains increase rapidly with increasing temperature. To provide a geometric picture of the chain fluctuations, their angle variation $\delta\theta$, marked by green lines in Figure 4.8b, is analyzed in Figure 4.9. The angle fluctuations equally increase with increasing temperature, thus, showing how higher temperatures promote higher bending of the chains. The fluctuations, thereby, occur by rotations around the connection point to the core as well as in-plane bending of the chains. Opposed to measurements at liquid-solid interface, where chains tend to point out from the surface or can form bonding motifs of multiple chains [185, 220, 221], the chains are observed to only interact with one other chain and are continuously adsorbed on the surface.

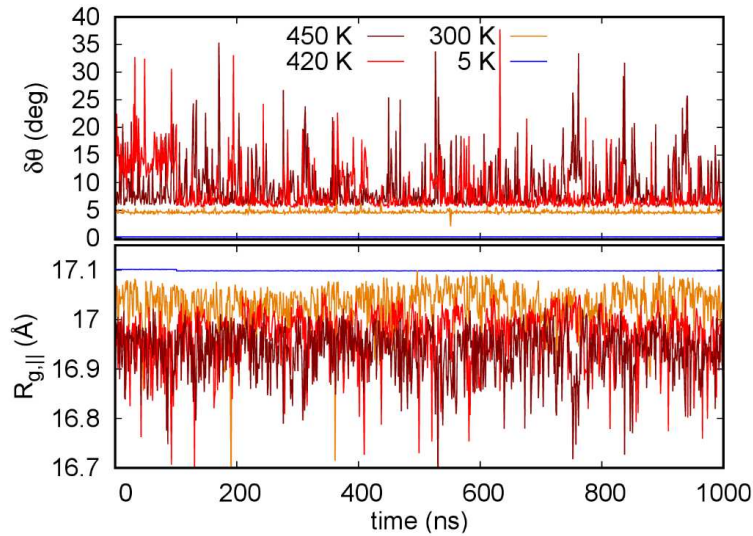


Figure 4.9: Thermal response of a single SW molecule. *Time averaged (over 1 ns) angle fluctuations (top), and parallel gyration tensor component as a function of time (bottom).*

The increasing bending of the molecule results in an interesting effect: With higher temperatures single molecules of SW show a decreasing effective radius, i.e. the molecules show a negative expansion coefficient. This is nicely shown by the sum of the diagonal terms of the radius of gyration tensor parallel to the surface $R_{g,||}$, presented in the bottom panel of Figure 4.9. A small but noticeable decrease is observed from 5 K to 300 K and then 450 K.

In conclusion, single SW molecules show a negative expansion due to increasing bending upon fluctuations of the chains with increasing temperature, but low displacement of the molecule itself. This points to a supramolecular mechanism of the observed thermal expansion of SW assemblies.

4.5 Thermal Expansion Mechanism

Deeper insights into how the thermal expansion of the SW molecular assembly is driven, were sought in a second step by considering a trimer assembly. The choice of only three molecules was made in order to maintain computational feasibility for the sheer size of the required simulation of large assemblies. This is because of the large system that has to be considered and mainly due to time scales (i.e. μs) in the simulations being several orders of magnitudes smaller than exist in the experiments (i.e.. minutes).

The simulations of the trimer were started from a compact structure mimicking a trimer observed at LT, shown with intermolecular distances in Figure 4.10a. The choice of a LT assembly is due to the time scales required to simulate cooling. With the decrease in thermal energy the time scale increases far above feasibility, since the slip events giving rise to the compaction of the network would become less and less frequent. Interestingly, the small assembly exhibits a slightly increased lattice spacing of 3.8 nm to 4.2 nm in comparison to the large assembly in Figure 4.7a with an average of 3.5 nm, pointing towards a packing effect and highlighting the importance of comparing similarly sized islands.

The trimer was generated by first using a configuration from a production run at 300 K. Then, an assembly of three SW molecules, shown in Figure 4.10b, was built with much larger distances than the experimental trimer to avoid steric repulsion between the chains of the different molecules. Following that, a 1 ns long MD simulation at 400 K was performed imposing the experimentally observed spacing of 3.9 nm with a harmonic restrain with a stiffness of 50 kcal/mol\AA^2 . This yielded the configuration seen in Figure 4.10c. Lastly, an annealing at 420 K for 10 ns was performed while maintaining the imposed intermolecular spacing by the same restrain. The resulting final configuration is presented in Figure 4.10d.

This configuration was used as initial state (Figure 4.11a) for the simulation processes started at either 5 K or 450 K². The applied heat induces an increase in thermal fluctuations and kinetic energy reducing the simulation time required to reach a thermal equilibrium. As mentioned for the single molecule, the simulation is chosen to be performed at a temperature of 450 K to allow equilibrium to be reached faster thanks to increased mobility. Experimentally, it is known that the molecules do not desorb at this temperature, since it corresponds to the annealing temperature after deposition. Influence of diffusion caused by the high temperature can be considered marginal, since, as seen in Figures 4.8a and c, the mobility of the molecule is small even at 450 K. This allows differentiation of the spontaneous core diffusion from the effect driving the thermal expansion.

Figure 4.11b shows a snapshot of the SW assembly after 1 μs MD simulation at 5 K. A small variation of the intermolecular distance is observed with small increases and decreases both visible. The reason for this is the previously mentioned shifting of the molecule position to improve registry between molecule and surface.

The simulation at 450 K – snapshot of the final state shown in Figure 4.11c – confirms

²<https://www.nature.com/articles/s43246-020-0009-2#Sec18>

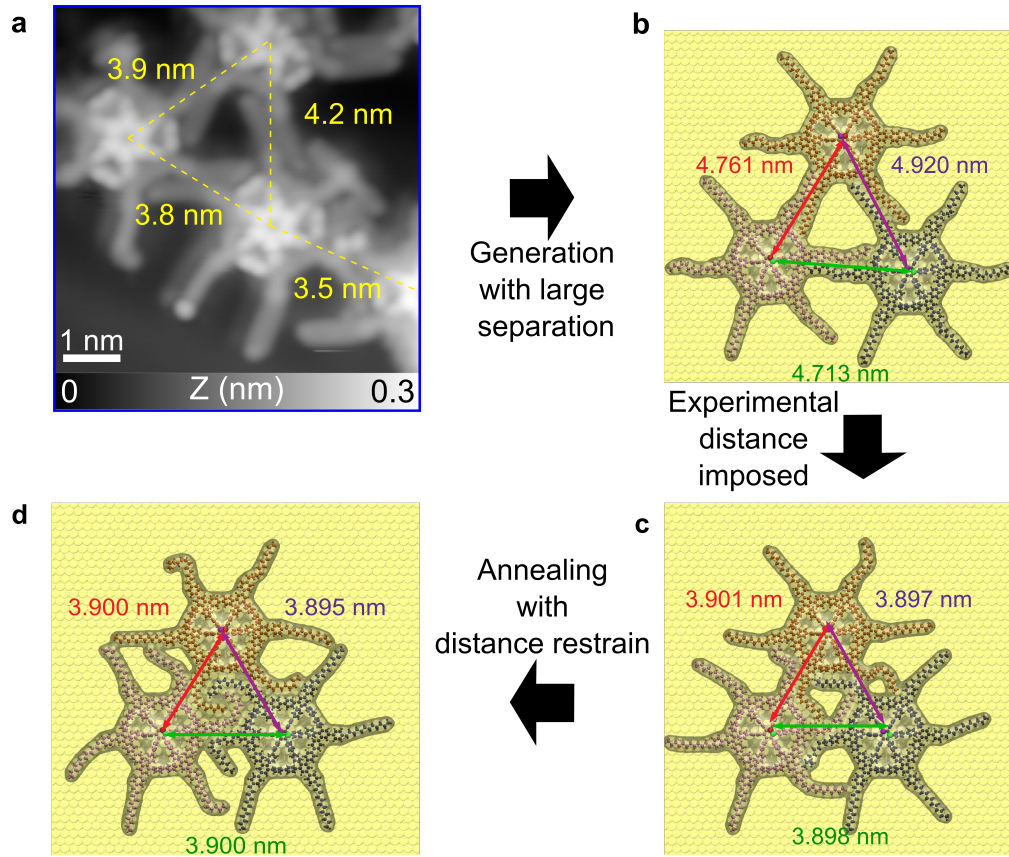


Figure 4.10: Building a SW trimer assembly for MD simulations from experimental assembly. **a**, STM topography image of a SW molecular trimer assembly at 5 K ($I = 1$ pA, $V_{Bias} = -380$ mV). **b**, Starting configuration built from equilibrated single SW MD simulations at 300 K. **c**, Configuration obtained after 1 ns of MD simulations at 300 K with the experimental intermolecular distance of 3.9 nm imposed by an harmonic restrain in the molecules center. **d**, Configuration after 10 ns long MD simulation at 450 K, keeping the molecule distance constant, to equilibrate the chains located between the molecules.

the significant thermal response of intermolecular spacing, rising from 3.9 nm at 5 K to 5.1 nm at 450 K. The corresponding thermal expansion coefficient of $\alpha_{SW,sim} = 660 \pm 120 \times 10^{-6} \text{ K}^{-1}$ compares well with the experimentally observed expansion value.

In addition, the MD simulations show the aforementioned preservation of the hexagonal network structure during each step of the simulation, further excluding the possibility of phase transition as explanation of the thermal response. At 450 K, the mobility of the chains between molecules, marked by pebbles in Figures 4.11a-c, is initially constrained by the tight packing. With increasing molecular spacing – the expansion – the chain displacement δ_{chains} presented in Figure 4.11d as a function of time increases. It starts low, but increases up to a value close to the equilibrium value of the unobstructed single chains in Figure 4.8c of $\delta_{chain}^{1,SW} = 3.34 \text{ \AA}$. In contrast to the single SW diffusion, the mobility of the cores is quite large in the triplet assembly. The

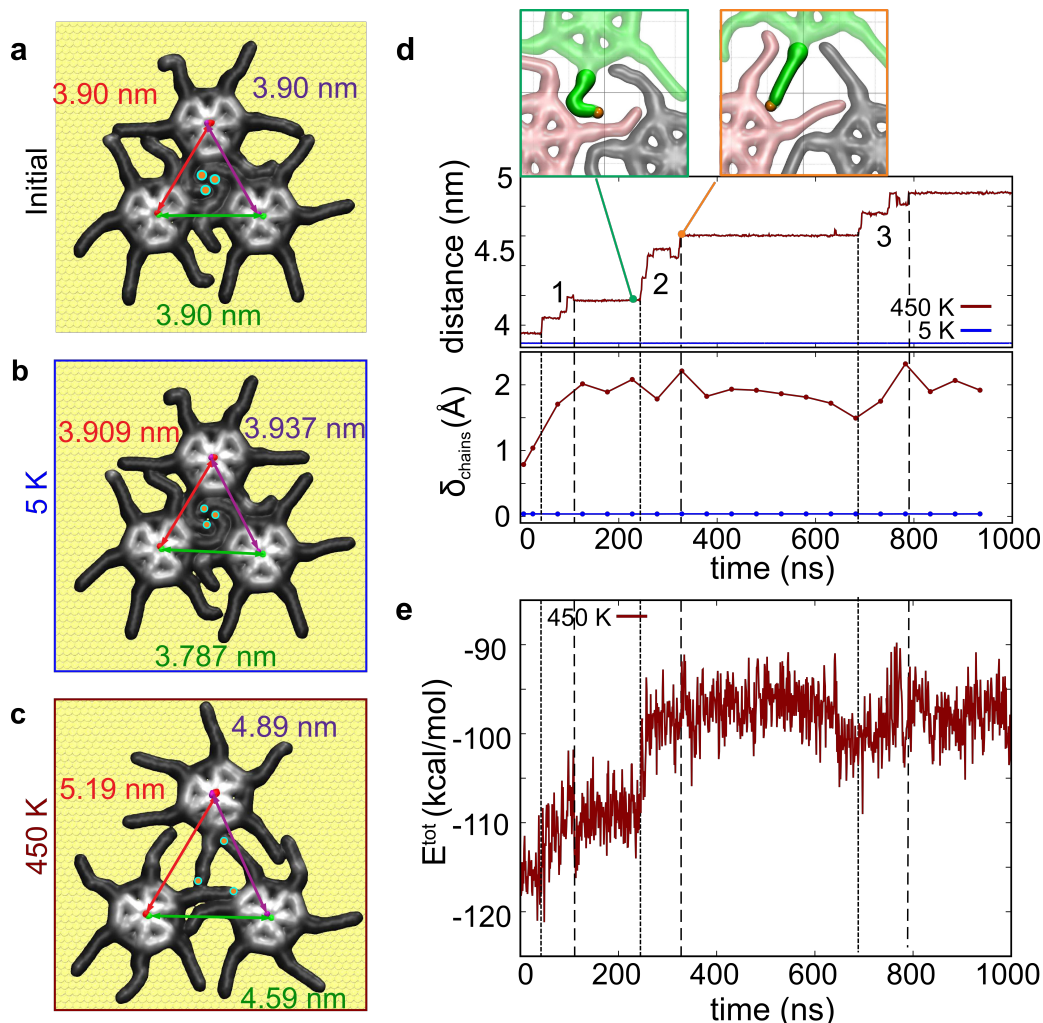


Figure 4.11: Thermal response of the SW trimer by chain mobility. *a*, Configuration of the SW trimer after initialization. *b*, Configuration of the SW trimer after 1 μ s long MD simulation at 5 K. *c*, Configuration of the SW trimer after 1 μ s long MD simulation at 450 K. *d*, Time-evolution of the average intermolecular distance (top) and chain fluctuations (bottom) of the SW trimer assembly during the MD simulation at 450 K. Inset are MD snapshots before and after expansion event 2 ($t = 275$ ns to $t = 300$ ns). *e*, Time-averaged evolution of the total energy of the SW trimer assembly during the MD simulation at 450 K.

molecule spacing increases significantly, as visible in the final state after MD simulation in Figure 4.11c and the intermolecular distance as a function of time in Figure 4.11d. This increase is driven by the increased chain fluctuations at the higher temperatures, the mobility is forcing the adjacent molecules away, pushing the network to expand.

Notably, the expansion of molecular spacing does not occur continuously, but in clearly distinguishable events, as marked by the dotted lines in Figure 4.11d. Between the expansion steps, long intervals (up to 300 μ s) of stability occur. An instructive event is illustrated by the snapshots in the insets in Figure 4.11d, showing the chain and

core positioning before and after the expansion event 2 at $t = 275$ ns. At the start of the expansion event (green inset) the green chain is close to the pink molecule restricting its lateral fluctuations, but also increasing molecular interaction by interdigitation. Following the expansion event (orange inset) the dodecyl chain is free to adopt a more extended configuration and less restricted in its lateral mobility. In the interval between event 2 and 3 (i.e. 300 ns to 700 ns) the relation of chain fluctuations to lattices expansion is especially well visible. Here, the chain mobility gradually decreases leading up to expansion event 3 and increases more thereafter.

The total energy of the SW trimer assembly as a function of time during the MD simulations is presented in Figure 4.11e. The thermal expansion causes a decrease of the internal energy of the system corresponding to the decrease in interdigitation of the dodecyl chains. At lower temperatures the interaction of the chains directs the close packing of the molecular assembly and increases the internal energy, while at higher temperatures the entropic contribution of the fluctuations of the chains to the free energy compensates the loss of internal energy and, therefore, facilitates the expansion of molecular spacing – the thermal expansion.

Thus, the giant thermal expansion can be explained by three properties of the dodecyl chains: First, the weak interaction with the surface, allowing the stark increase in fluctuations with rising temperatures, second, the soft in-plane bending of the chains, encouraging this oscillation mode over other rigid vibrations and, lastly, the two-dimensional constraint on the fluctuations imposed by the surface, preventing out of surface oscillations.

4.6 Summary

In this chapter, first, thermal expansion of molecular materials and some of the corresponding mechanisms were discussed. Then, nc-AFM and STM measurements were employed to investigate the large SW molecule deposited by ESD at 5 K and 300 K. High-resolution imaging of single molecules, still present after an annealing step, along with MD simulations revealed a corrugation inside the molecule core. The spokes and alternating sides of the spoked wheel forming the molecule core are turned upside by steric hindrance resulting from the spokes close to the core and consequently the sides.

Upon investigation of large scale assemblies a large thermal response of the molecule spacing from 5 K to 300 K was observed, the corresponding thermal expansion coefficient is, thus, $\alpha_{SW,exp} = 980 \pm 110 \times 10^{-6} \text{ K}^{-1}$. MD simulations were performed at different temperatures both on single molecules and a small assembly built from a similar trimer observed at LT. Single molecules revealed low diffusion on the surface for temperature up to 450 K, while a marked increase in chain fluctuations was observed for such temperatures.

For the trimer assembly, MD simulations at 5 K and 450 K confirmed the large lattice increase and resulted in a consistent thermal expansion coefficient of $\alpha_{SW,sim} = 660 \pm 120 \times 10^{-6} \text{ K}^{-1}$. By looking at the chain fluctuations in relation to the intermolecular spacing in the trimer, a mechanism of expansion based on the chain fluctuations forcing the network to expand was found. The chains between the molecules are limited in

Chapter 4. Thermal Expansion by Alkyl Chain Motion

their mobility by the close packing, leading to the network being pushed outwards and the chains recovering and increasing their mobility. Corresponding loss of interaction energy due to reduced interdigitation of the dodecyl chains is, thereby, compensated by the entropic contribution of the free energy.

In conclusion, a new mechanism of thermal expansion based on chain mobility of alkyl chains in supramolecular networks was found, allowing the introduction of thermal response of supramolecular assemblies with a relatively simple synthesis step.

Tuning Thermal Expansion by Alkyl Chain Functionalization

TUNING thermal expansion and, thus, precisely controlling the response of a material to heat is of high interest in a variety of fields, notably sensors [9, 222], since it opens ways to form highly precise thermal sensors. By basing those on soft materials, like polymers or supramolecular materials, this can even allow flexible sensors, possibly for biological applications [6, 9]. If specific thermal expansion with anisotropic behavior is achieved, artificial muscles become feasible [5, 223]. Applications in aerospace can be facilitated by targeting very low thermal response and a high stability of the material [8].

Based on the mechanism explained in the previous chapter and depositions facilitated by ESD, tuning of the thermal response of materials might be possible by modifying the length of alkyl chains and, thereby, their mobility behavior. In this chapter, such tuning is investigated using a model molecule, hexabenzocoronene. This choice is made because of the more simple structure shown in Figure 5.1a to minimize the already marginal influence of the core structure. In addition, it significantly reduces the difficulty of synthesis and inclusion of alkyl chains. Three HBC molecules equipped with different alkyl chains (HBC-R) are studied on both Ag(111) and Au(111), first HBC-6C₄H₉, then HBC-6C₈H₁₇ and lastly HBC-6C₁₂H₂₅, at 5 K and 300 K. Depending on chain length and associated thermo-lability, the molecules are either deposited by TE or ESD at RT. Thereafter, using STM and nc-AFM imaging their thermal response, from 5 K to 300 K, is compared. An inversely proportional dependence of thermal expansion and chain length is observed. Chiral behavior of the chains is also discovered with possible influence of chain length along with temperature. Lastly, uniformity and possible phase or packing changes are investigated by additional imaging at 77 K, revealing a larger CTE at lower temperatures.

5.1 Thermal Response of Alkyl Chain Functionalized HBCs

Even though, the small influence of the core on the thermal expansion process was evidenced for the SW, a similar core, HBC, was chosen and equipped with different length of alkyl chains. The choice of chain lengths was planned to include in addition to the butyl, octyl and dodecyl chains another molecule equipped with octadecyl chains (HBC-6C₁₈H₃₇), which however could not be deposited successfully due to low solubility. The high similarity of the molecules - only the alkyl chains differ - allows for a relative simple illustration of the molecular and network structure based on one of the molecules. All three of them consist of a molecular core formed by 13 benzene rings resulting in a hexabenzocoronene. The alkyl chains are, similarly to the SW, attached to the outer benzenes of the core giving the molecule and core a star-shaped structure as shown in Figure 5.1a. Figure 5.1b shows a high-resolution STM topography image of HBC-6C₄H₉ molecules at 5 K deposited by TE on Au(111) as an example of the molecular structure. The molecule contains the shortest (butyl) chains employed in this work, which results in low solubility, but suitability for TE. The planar star-shaped core of the molecules is easily visible along with the slightly darker appearing butyl chains forming the expected hexagonal network with alkyl chain interdigitation [194,224,225]. The corresponding constant height AFM image with a CO functionalized tip in Figure 5.1c reveals the bond level structure of both the chains as well as the core, resolving the benzene rings inside the cores.

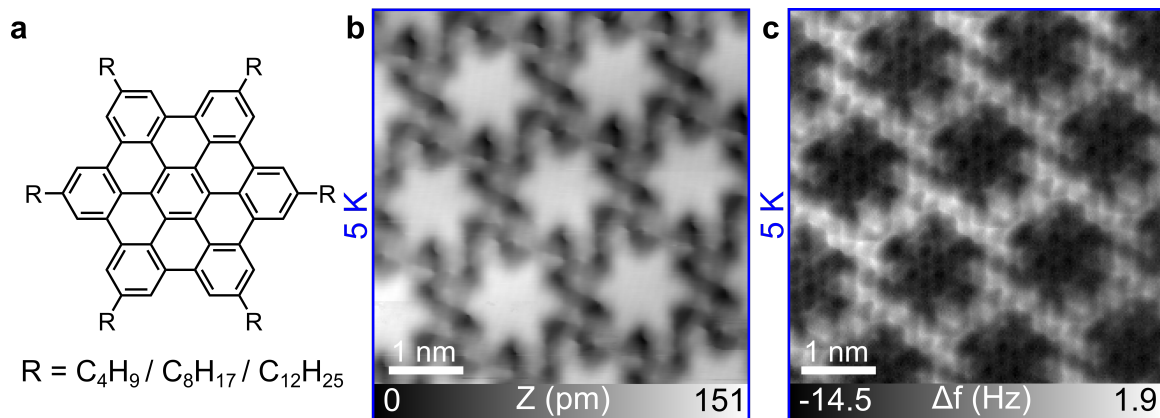


Figure 5.1: Structure of alkyl chain functionalized HBCs. **a**, Chemical structure of HBC functionalized with different alkyl chains. **b**, High-resolution STM topography image of HBC-6C₄H₉ at 5 K, showing the core and side chains ($I = 1$ pA, $V_{Bias} = -700$ mV). **c**, Corresponding bond-resolved constant height AFM image at 5 K ($A = 70$ pm).

Investigation of the alkyl chain length influence on the thermal response was also combined with a study of the influence of the surface. For this, the molecules were deposited on both Au(111) and Ag(111) for studies of their intermolecular spacing by STM and nc-AFM at 5 K and 300 K. To minimize influence of packing and compaction

5.1. Thermal Response of Alkyl Chain Functionalized HBCs

effects, similar islands in submonolayer coverage are targeted like considered for the SW. For the same reason, if accessible, islands on large terraces were investigated to limit boundary and diffusion influences.

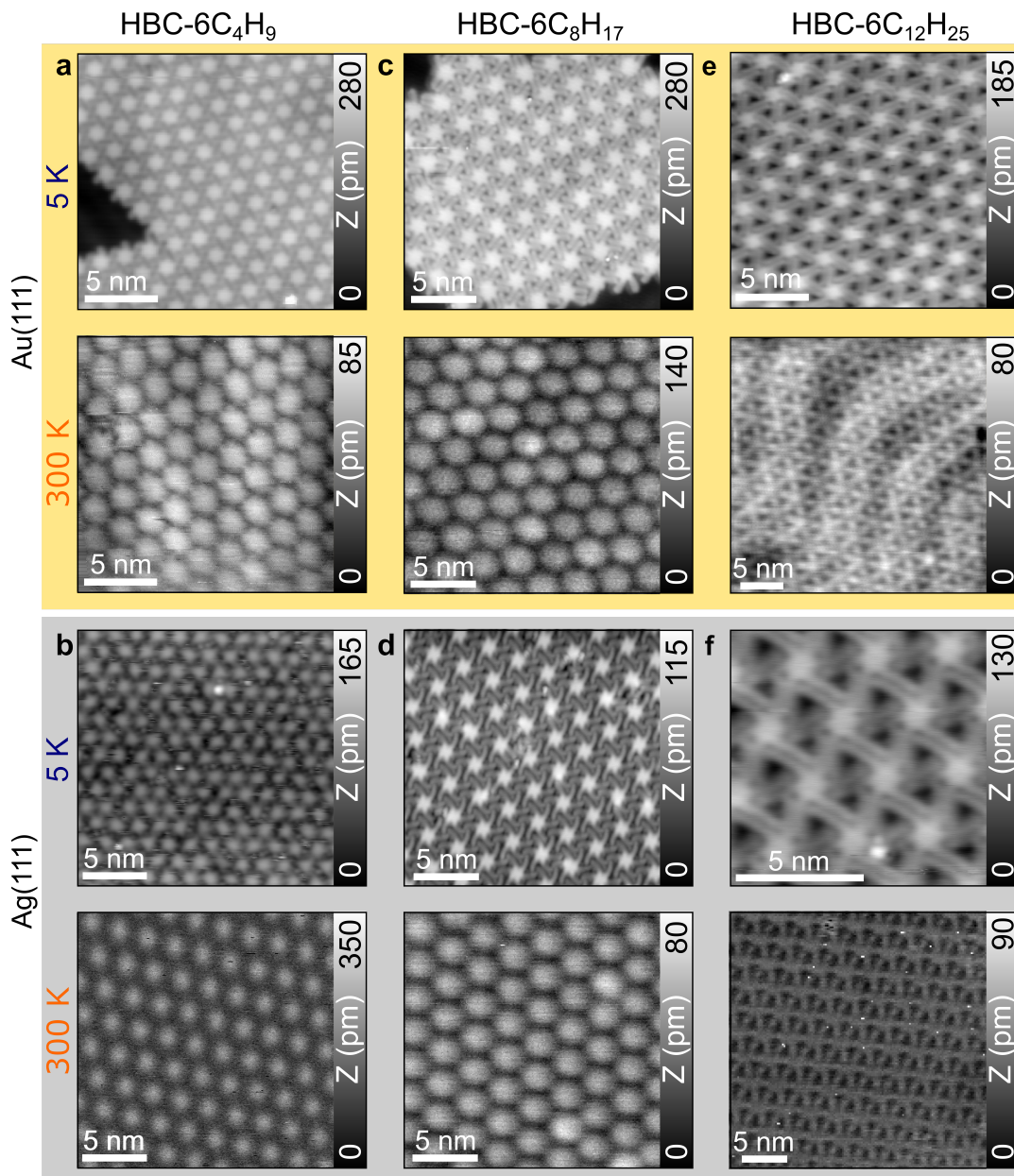


Figure 5.2: Thermal response of alkyl chain functionalized HBCs. **a**, Thermal response of a $HBC-6C_4H_9$ assembly on $Au(111)$ ($I = 1$ pA, $V_{Bias} = -500$ mV, $A_2 = 800$ pm, $\Delta f_2 = -76$ Hz) and **b**, $Ag(111)$ ($I = 1$ pA, $V_{Bias} = -700$ mV, $A_2 = 800$ pm, $\Delta f_2 = -20$ Hz). **c**, Thermal response of $HBC-6C_8H_{17}$ on $Au(111)$ ($I = 1$ pA, $V_{Bias} = -700$ mV, $A_2 = 1200$ pm, $\Delta f_2 = -65$ Hz) and **d**, $Ag(111)$ ($I = 1$ pA, $V_{Bias} = -200$ mV, $A_2 = 800$ pm, $\Delta f_2 = -30$ Hz). **e**, Thermal response of $HBC-6C_{12}H_{25}$ on $Au(111)$ ($I = 1$ pA, $V_{Bias} = -800$ mV, $A_1 = 2$ nm, $\Delta f_1 = -50$ Hz) and **f**, $Ag(111)$ ($I = 1$ pA, $V_{Bias} = -300$ mV, $A_2 = 600$ pm, $\Delta f_2 = -40$ Hz).

Figures 5.2a-f show resulting molecular networks at both 5 K and 300 K (top and bottom) for the three molecules on Au(111) and Ag(111). Importantly, the prominent hexagonal network structure is preserved for both surfaces and temperatures for all three molecules. The bright protrusions, thereby, correspond to the molecule cores. In some cases also the alkyl chains stabilizing the network and driving the mechanism of expansion are visible as elongated protrusion between the cores, mostly at 5 K but also at 300 K (compare especially Figures 5.2e and f). The aforementioned preservation of the hexagonal adsorption structure over the whole temperature, as previously discussed for the SW, indicates that the desired expansion occurs without a phase change.

By comparing the intermolecular spacing, a significant increase is visible for higher temperatures in the topography images in Figures 5.2a-d on both surfaces. The HBC-6C₁₂H₂₅ molecule assembly on Au(111), shown in Figure 5.2e, still shows pronounced expansion, while the same molecule on Ag(111) (Figure 5.2f) shows no easily discernible change.

Precise quantification of the observed expansions along with their uncertainties are obtained by real-space measurements of the molecular spacing along the molecule line closest to parallel to the fast scan axis. This method is chosen to minimize possible influence of drift and to increase statistical precision by measuring each molecule separately. For HBC-6C₄H₉, equipped with the shortest chains, this gives lattice parameters of 1.70 ± 0.04 nm and 1.67 ± 0.03 nm at 5 K, which increases to 2.06 ± 0.06 nm and 2.26 ± 0.07 nm at 300 K on Au(111) and Ag(111), respectively. The resulting thermal expansion coefficients of $\alpha_{C_4,Au(111)} = 598 \pm 119 \times 10^{-6} \text{ K}^{-1}$ on Au(111) and $\alpha_{C_4,Ag(111)} = 881 \pm 119 \times 10^{-6} \text{ K}^{-1}$ are well within the expected large regime of expansion.

Analogously, measurements on the HBC-6C₈H₁₇ molecule assemblies on Au(111) and Ag(111) reveal lattice spacings of 2.33 ± 0.04 nm and 2.54 ± 0.03 nm at 5 K and an increase to 2.91 ± 0.07 nm and 2.81 ± 0.07 nm at 300 K, respectively. Corresponding CTEs are $\alpha_{C_8,Au(111)} = 672 \pm 88 \times 10^{-6} \text{ K}^{-1}$ and $\alpha_{C_8,Ag(111)} = 325 \pm 91 \times 10^{-6} \text{ K}^{-1}$ on Au(111) and Ag(111). Lastly, the less pronounced expansion of the HBC-6C₁₂H₂₅ assemblies was evaluated. Here, measurements of the lattice spacing show 2.86 ± 0.06 nm and 2.91 ± 0.04 nm at 5 K, which increases to 3.12 ± 0.1 nm and 2.99 ± 0.06 nm at 300 K on Au(111) and Ag(111), respectively. On Au(111) this still gives thermal expansion of $\alpha_{C_{12},Au(111)} = 279 \pm 128 \times 10^{-6} \text{ K}^{-1}$, while no significant thermal expansion can be observed on Ag(111) with a CTE of $\alpha_{C_{12},Ag(111)} = 96 \pm 81 \times 10^{-6} \text{ K}^{-1}$.

5.2 Thermal Expansion Dependent on Alkyl Chain Length and Substrate

Based on the measurements obtained from the three HBC-R molecules equipped with butyl, octyl and dodecyl chains on the two surfaces of Au(111) and Ag(111), a relation between chain length and thermal expansion was found. The lattice parameters on both surfaces for the three molecules are summarized in Table 5.1 along with the associated thermal expansion coefficients. Included are also both the SW molecule

5.2. Thermal Expansion Dependent on Alkyl Chain Length and Substrate

and unfunctionalized HBC lattice parameters and expansion coefficients [22, 194].

Table 5.1: Coefficients of thermal expansion of 2D molecular assemblies. Comparison of lattice parameter a measured at 5 K and 300 K and the corresponding coefficient of thermal expansion α for supramolecular assemblies of HBC, HBCs functionalized with alkyl chains (HBC-6C₁₂H₂₅, HBC-6C₈H₁₇ and HBC-6C₄H₉) and the SW molecule.

	a_{5K} (nm)	a_{300K} (nm)	α (10^{-6} K ⁻¹)
HBC-6C ₄ H ₉ on Ag(111)	1.67 ± 0.03	2.26 ± 0.07	881 ± 119
HBC-6C ₄ H ₉ on Au(111)	1.70 ± 0.04	2.06 ± 0.06	598 ± 119
HBC-6C ₈ H ₁₇ on Ag(111)	2.54 ± 0.03	2.81 ± 0.07	325 ± 91
HBC-6C ₈ H ₁₇ on Au(111)	2.33 ± 0.04	2.91 ± 0.07	672 ± 88
HBC-6C ₁₂ H ₂₅ on Ag(111)	2.91 ± 0.04	2.99 ± 0.06	96 ± 81
HBC-6C ₁₂ H ₂₅ on Au(111)	2.86 ± 0.06	3.12 ± 0.1	279 ± 128
SW on Au(111)	3.5 ± 0.1	4.5 ± 0.2	980 ± 110
HBC	1.395 (1.2 K)	1.401	14

To illustrate the influence of the chain length, Figure 5.3 shows the thermal expansion coefficients obtained for the different chain length and substrates. Of note is the quasi linear increase of CTE from the longest chains, HBC-6C₁₂H₂₅, to the shortest chains, HBC-6C₄H₉ on Ag(111), showing a clear inversely proportional dependence of the chain length to the thermal expansion coefficient. Similar behavior is observed on Au(111) for HBC-6C₈H₁₇ and HBC-6C₁₂H₂₅, but no further increase in expansion for HBC-6C₄H₉ was observed. Comparison of the CTE on the two surfaces shows an increase from Ag(111) to Au(111) for the two longer molecules, but interestingly a reversal for HBC-6C₄H₉. This indicates that a limit to the increasing expansion is reached earlier on Au(111). Possible reasons could be a stronger bonding on the Au(111) surfaces compared to Ag(111) [226] or, even though, during measurements this influence was minimized the size of the terraces or other external factors.

The continuous CTE increase, with shorter chains showing larger expansion, on Ag(111) and excluding the limit on Au(111), is likely related to a combination of factors: First a closer packing at low temperatures due to the relatively higher space for the chains and second upon heating a stiffer in-plane bending of the chains as a result of their lower bending freedom forcing a larger relative expansion. If we compare the HBC molecules with both the unfunctionalized HBC [194] and the SW molecule (Chapter 4), the influence of the chains is once more illustrated, since no exceptional thermal expansion above the substrate expansion is observed without alkyl chains present. The SW molecule assembly, however, shows large thermal expansion even with the dodecyl chains also present in the HBC-6C₁₂H₂₅. This points towards an influence of the packing on the molecular expansion. The longer chains on the smaller HBC molecules might not allow compression of the molecules as close together upon cooling in comparison to the SW molecules with their much larger core sides and also in contrast to the shorter chain molecules. There, the butyl and octyl chains might

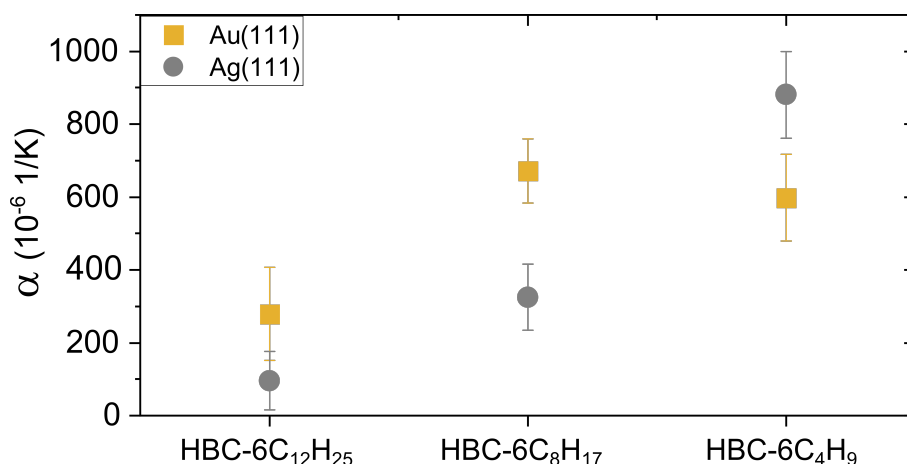


Figure 5.3: Thermal expansion dependent on alkyl chain length and substrate. *Thermal expansion dependent on alkyl chain length and substrate.*

allow for tighter compression, while the stiffer in-plane bending could still drive the large expansion, resulting in a significant increase in thermal expansion. The core, thus, influences the thermal response not by its influence on diffusion, but by limiting the packing capability.

5.3 Chain Length Influence on Temperature Dependent Molecular Surface Chirality

In addition to the desired tuning of the thermal expansion, some further intriguing properties arising from the different chain length, like chirality, can be observed in the networks shown in Figure 5.2. In previous works, chirality on surfaces has been among others shown by modification of the surface, lattice mismatch, chiral templating or by the adsorption of chiral or prochiral molecules [227–237]. High-resolution studies have allowed controlling the chiral behavior for example by SPM manipulations or by coverage level [235, 238–240].

Interestingly, the chain behavior is not uniform for the networks of the different chain lengths. For the two shorter chain molecules, HBC-6C₄H₉ and HBC-6C₈H₁₇, tilted alkyl chains on both Au(111) and Ag(111) at 5 K (compare Figures 5.2 and 5.5), result in two possible enantiomers and, thus, adsorption dependent molecular chirality. Imaging of HBC-6C₄H₉ at 77 K and 300 K revealed the chains to also be tilted at higher temperatures, albeit in the other enantiomeric configuration at 300 K (compare Figures 5.5b and c). The presence of both enantiomers can, thereby, be inferred even though only one was resolved for each surface due to the statistics of chirality and symmetry of molecules and surfaces [27, 228]. In contrast, for the dodecyl equipped HBC-6C₁₂H₂₅ no chirality at 300 K both on Ag(111) and Au(111) is observed with nc-AFM measurements, as seen in Figures 5.2e and f. The chains are positioned straight outwards from the molecules. The different adsorption motifs are illustrated in Figure 5.4. Thereby, the chains are shown as conical shapes to represent their possible

bending and mobility.

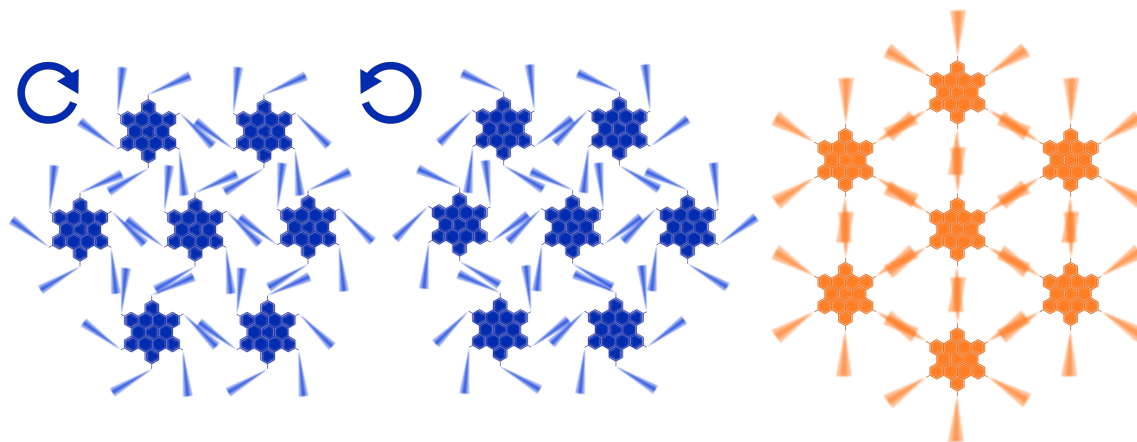


Figure 5.4: Illustration of temperature dependent molecular surface chirality. *Illustration of temperature dependent chirality of HBC-6C₁₂H₂₅ at 5 K and 300 K. Two enantiomers resulting from chain tilting are observed at 5 K, while no chirality was visible at 300 K.*

Since a thermally stable surface/adsorption chirality was observed for the shorter chains but not for the dodecyl chains equally on both surfaces, an influence of the substrate can be excluded. Thus, the only difference is the chain length and the associated change in bending freedom and spacing. The chain fluctuations are likely stiffer due to the lower bending freedom, but at the same time have a larger unobstructed area around them, allowing them the positioning in chiral fashion. The long chains are limited by packing and especially at higher temperatures show high mobility and large angle changes, as seen for the SW in Figure 4.8c and Figure 4.9. However, the limitation of the imaging time scales might also play a role here. The images are only showing an average position of the chains and the longer chains might show more flexibility and a wiggly shape which can not be resolved due to their mobility at 300 K. At 5 K, the chain mobility is close to zero and the image shows a fixed position of the chains.

5.4 Phase Behavior upon Cooling of HBC-6C₄H₉

To provide experimental insight into the behavior of the networks during the expansion and complement the MD simulations evidencing the preservation of the adsorption geometry and phase over the expansion process, i.e. for 5 K to 300 K, STM measurements of HBC-6C₄H₉ were additionally performed at 77 K on Ag(111). Resulting high-resolution topography and second pass frequency shift images with submolecular resolution at 5 K, 77 K, and 300 K are shown in Figure 5.5.

In a first step, the thermal expansion behavior from 5 K to 77 K and 77 K to 300 K can be compared and put in relation to the total thermal expansion of $\alpha_{C_4, Ag(111)} = 880 \pm 119 \times 10^{-6} \text{ K}^{-1}$. With the molecular spacing at 77 K of $1.94 \pm 0.03 \text{ nm}$ this

results in a CTE of $\alpha_{5-77K} = 1905 \pm 296 \times 10^{-6} \text{ K}^{-1}$ from 5 K to 77 K and $\alpha_{77-300K} = 637 \pm 152 \times 10^{-6} \text{ K}^{-1}$. Thus, the expansion is significantly larger in the lower regime while it is lower at higher temperatures. This fits well with the underlying mechanism of expansion. At low temperatures the network is packed compactly with a high degree of interdigitation between chains and close interaction with the molecule cores. Upon increasing temperature, the chain mobility increases quickly and due to close packing results in relatively large expansion steps to obtain less obstructed mobility. This again increases entropic contributions while reducing interaction. On the other hand, at higher temperatures the expansion has already set in quite strongly and expansion events become less frequent due to the already increased spacing, as observed in the MD simulations of SW trimer assembly shown in Figure 4.11.

The submolecular resolution images in Figures 5.5a-c, where the chains are also resolved, allow investigation of the adsorption geometry over the expansion. In the STM topography image at 5 K in Figure 5.5a the cores forming the hexagonal network along with the alkyl chains between them are resolved. Interestingly, they are not positioned straight between the molecules but instead tilted counter-clockwise.

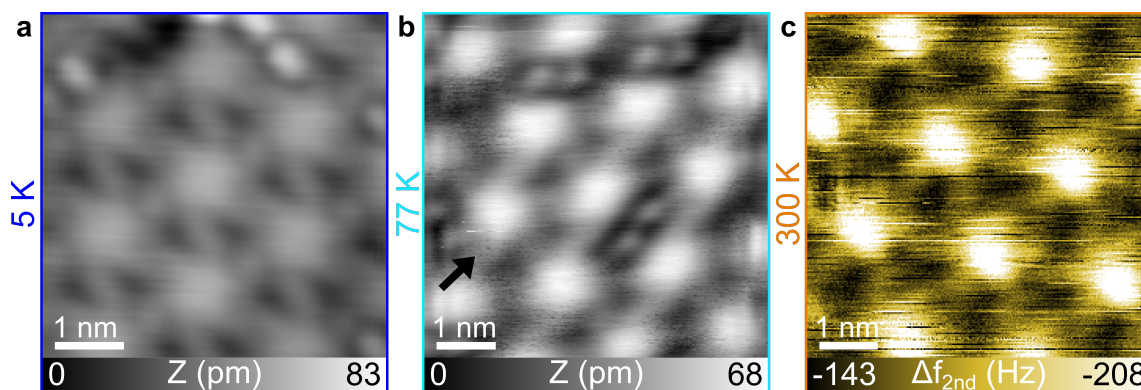


Figure 5.5: Phase response of HBC-6C₄H₉ dependent on temperature. **a**, High-resolution STM image of HBC-6C₄H₉ on Ag(111) at 5 K ($I = 1 \text{ pA}$, $V_{Bias} = -100 \text{ mV}$). **b**, High-resolution STM image of HBC-6C₄H₉ on Ag(111) at 77 K ($I = 1 \text{ pA}$, $V_{Bias} = -700 \text{ mV}$). **c**, Second pass frequency shift AFM image of HBC-6C₄H₉ on Ag(111) at 300 K ($A_2 = 400 \text{ pm}$, $\Delta f_2 = -100 \text{ Hz}$).

At 77 K, as shown in Figure 5.5b, a similar, albeit slightly enlarged, hexagonal network can be observed. The chains are, thereby, less visible, likely due to instability in the thermal regime at 77 K caused by the system not fully reaching thermal equilibrium. At the black arrow, however, the chains can be distinguished to be tilted clockwise. Imaging at 300 K with the multipass technique also allows the resolution of both core and chains, revealing the still preserved hexagonal network, as shown in Figure 5.5c. Of note is here, that the contrast of the image is reversed since the apparent height and, thus, the observed frequency shift were reversed, as previously found for nc-AFM measurements [241]. The resolved chains maintain the observed tilt and are titled clockwise similar to at 77 K as discussed above.

With the imaging at 5 K, 77 K and 300 K, the preservation of the adsorption geometry, considering the statistics of chirality, and the chain positions further strengthens

simulation based assumptions that no phase change occurred during cooling/heating and the expansion is solely due to the aforementioned mechanism.

5.5 Summary

In this chapter, the mechanism of thermal expansion, found for the SW molecule in the previous Chapter 3, was applied to present tuning possibilities of the thermal response of molecular assemblies by modifying their chain length.

In a first step, the thermal response of three HBC molecules equipped with three different chain lengths was studied with STM/AFM at 5 K and nc-AFM measurements at 300 K on both Au(111) and Ag(111). This revealed an inversely proportional dependence of the thermal expansion on the chain length with a limit to the expansion reached on Au(111), while the increase was continuous on Ag(111). CTEs increased from a minimum of $\alpha_{C_{12},Ag(111)} = 96 \pm 81 \times 10^{-6} \text{ K}^{-1}$ on Ag(111) for HBC-6C₁₂H₂₅ to a giant expansion of $\alpha_{C_4,Ag(111)} = 881 \pm 119 \times 10^{-6} \text{ K}^{-1}$ for HBC-6C₄H₉ on Ag(111). The expansion on Au(111), excluding the limitation for the shortest chains, was generally larger than on Ag(111) resulting in a still large thermal expansion even for the dodecyl chains of $\alpha_{C_{12},Au(111)} = 279 \pm 128 \times 10^{-6} \text{ K}^{-1}$. Thus, influence of the substrate seems significant and, notably, shorter chains resulted in a larger thermal expansion coefficient. This is likely related to a variation in the in-plane bending towards more stiff oscillations and a limit to the compression of the molecules equipped with longer chains due to their packing between the molecules.

In a further step, the behavior between the observed endpoints was investigated to reveal a nonuniform expansion with imaging at 77 K. At low temperatures the expansion is significantly increased in line with the underlying mechanism. In addition, the adsorption geometry was observed to also be maintained at 77 K confirming the absence of phase transitions in the expansion.

In conclusion, the possibility of tuning the thermal expansion of molecular assemblies by the supramolecular mechanism based on alkyl chain mobility was shown with an inversely proportional relation observed between the chain length and the thermal expansion. This provides interesting possibilities for sensor design, especially for biological applications, due to the high flexibility of supramolecular materials and the versatility of possible core functionalities, since addition of alkyl chains is a relatively simple process.

Solution Synthesized Graphene Nanoribbons on Surfaces by ESD

GRAPHENE nanoribbons, thin quasi-one-dimensional sheets of graphene, are of significant interest due to their interesting electronic properties [242–245]. Ballistic transport or spin-split edge states were found among other intriguing properties, like the tuning of the band gap by engineering the width of GNR [246–251]. Size confinement along one dimension, incorporation of heteroatoms or the fine control of their edges allows tuning their electronic properties [10, 12, 13, 108, 245, 252–257].

In this chapter, first the most common method of obtaining GNRs on surfaces, on-surface synthesis, is introduced. The most common reaction path and possibilities of this approach, but also its limitations are discussed. Then, the possibilities of solution based synthesis are explained. Importantly for this work, the significant hurdle of deposition for high-resolution SPM studies in UHV is discussed. In a first step towards new, previously (on surface) inaccessible GNRs, a methoxy functionalized GNR (Figure 6.1a) is deposited by ESD and studied with nc-AFM at RT. Thereby, a high mobility of the rigid OMeGNR is found on Au(111).

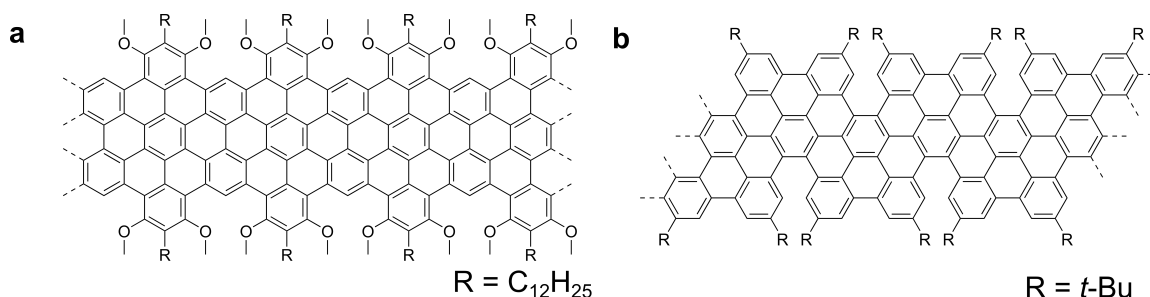


Figure 6.1: Structure of the GNR molecules. a, *Chemical structure of OMeGNR.* b, *Chemical structure of FGNR.*

In a next step, a non-planar twisted fjord-edged GNR (Figure 6.1b), is shown with help of ESD, allowing three-dimensional non-planar GNRs to be accessed. Studies of a model precursor allow confirmation of the twist induction and investigation of on-

surface reactions. Lastly, the FGNR is additionally to the metallic Au(111) surface also deposited on two non-metallic surfaces, HOPG and KBr(001). This provides access to new further surfaces and possibly decoupling from the surface. Additionally, two more depositions of GNRs are or were previously performed, a well-elongated "cove"-type GNR (CGNR) which was studied in a previous work [179] and a similar CGNR equipped with an increased number of alkyl chains, which could not be observed on the surface due to residual alkyl chains in the received molecules. Results from these are included to provide additional information in the main manuscript or in the appendix.

6.1 Graphene Nanoribbons on Surfaces

6.1.1 On-surface Synthesis

The most prevalent method of obtaining atomically precise GNRs on surfaces for fundamental studies is the bottom-up on-surface synthesis. The first successful synthesis of atomically precise GNRs was achieved in 2010 [107] based on combination of Ullmann-type coupling and a subsequent cyclodehydrogenation, as shown in Figure 6.2a [107,258]. For this generally rationally designed halogen-substituted aromatic precursor molecules are evaporated on clean metallic surfaces in UHV. Then, an annealing is applied to split off the halogen substituents resulting in the creation of biradicals and subsequent the formation of a polymer or metal-organic intermediate in a surface-assisted Ullmann-type coupling reaction (1) [108,258]. Finally, a surface-assisted cyclodehydrogenation (2) results in the formation of a GNR with atomically well-defined edge structure and precursor dependent width. A resulting armchair GNR with its structure overlaid is shown exemplary in Figure 6.2b [108,259].

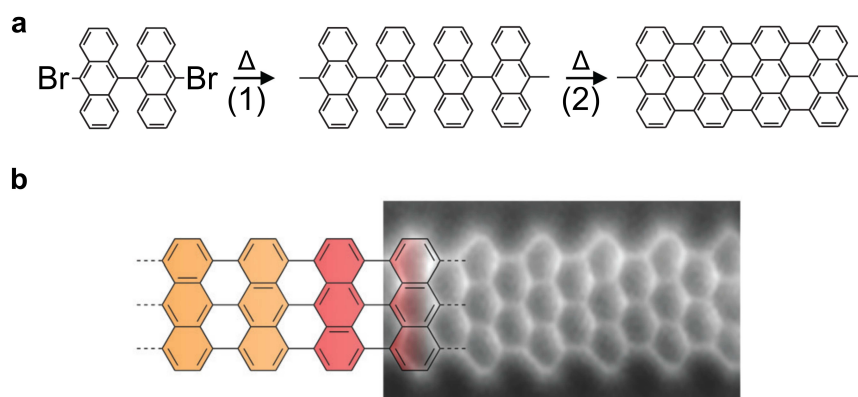


Figure 6.2: Illustration of on-surface synthesis. **a**, *On-surface synthesis steps of an armchair GNR, consisting of a surface-assisted Ullmann-type coupling reaction (1) and a surface-assisted cyclodehydrogenation (2).* **b**, *Constant height AFM image of a GNR by on-surface synthesis. Adapted from [107,108,259].*

By placing the substituents not in symmetric positions and inclusion of steric hindrance elements can allow the formation of a zigzag structured polymer and as finished product zigzag-GNR [255,260–262].

With rational design of precursor a wide variety of edge structures, like cove and "cove"-type edges or gulf edges, and inclusion of heteroatoms, notably boron or nitrogen, as well as holes and angles are achieved, allowing GNRs to present a variety of interesting properties, like topological states, quantum dots and band gap engineering [108, 243, 247, 252, 254, 260, 262–276].

The choice of precursor, however, suffers from the limitations of deposition by thermal evaporation and aforementioned annealing steps during the on-surface synthesis. Thermally labile as well as large structures are, thus, precluded, somewhat limiting the achievable structures. This mostly excludes alkyl chains and other labile functionalities and limits the possibility of achieving non-planar GNRs [277].

In addition, on-surface synthesis is usually limited by the need for a metal surface for the reactions [109, 278, 279], limiting studies of the electronic properties due to coupling to the conducting surface [48, 49, 260]. This can be mitigated by transferring on-surface synthesized GNRs onto thin insulating layers or modifying the top layer of the substrate to allow new insights into the electronic structures of GNRs [260, 265, 266, 270, 280, 281]. Additionally, some approaches have been achieved which expand the on-surface synthesis to new surfaces, e.g. rutile TiO_2 , based on sequential polycondensation, cyclodehydrofluorination, and cyclodehydrogenation reactions [109].

6.1.2 Solution Synthesis

Solution synthesis preparation approaches can offer some interesting new structures and functionalities, solving some of the limitations of on-surface synthesis, while maintaining atomic precision [11–13, 282].

A wide variety of solution based approaches to synthesize GNRs are known, commonly used are combinations of (AB-type) Suzuki, Yamamoto, Diels-Alder polymerizations and Scholl reactions or intramolecular oxidative cyclodehydrogenation [11–13, 253, 257, 282–288].

This can facilitate the formation of very long GNRs [12, 286, 289, 290] and allow the controlled incorporation of functional groups on the edges [257, 286, 291–294]. Interestingly, this can be performed both before the synthesis by incorporation in precursor molecules, but also via "post-functionalization" after the completion of the desired GNRs. Thereby, either edge chlorination [295] or transition-metal-catalyzed coupling reactions with pre-installed halogen substituents are applied [286, 296, 297]. This can allow the incorporation of edge functionalizations and additional heteroatoms not accessible by on-surface synthesis, notably alkyl chains or biomolecules, due to the annealing steps required [12]. An indicative example of two reaction paths to obtain well-defined and elongated GNRs in solution are provided for armchair and "cove"-type GNR in Figures 6.3a and b. The armchair GNR is synthesized via a Suzuki polymerization followed by graphenisation, while the "cove"-type GNR synthesis involves an AB-type Diels-Alder polymerization and intramolecular oxidative cyclodehydrogenation [11, 12]

Interestingly, solution synthesis also opens the possibility of synthesizing GNRs with twisted non-planar structures, of great interest for non-linear optics, nanomechanics and asymmetric catalysis [10, 298, 299]. 3D GNRs and notably non-planar GNRs are not readily available by on-surface synthesis due to the aforementioned limitations on

Chapter 6. Solution Synthesized Graphene Nanoribbons on Surfaces by ESD

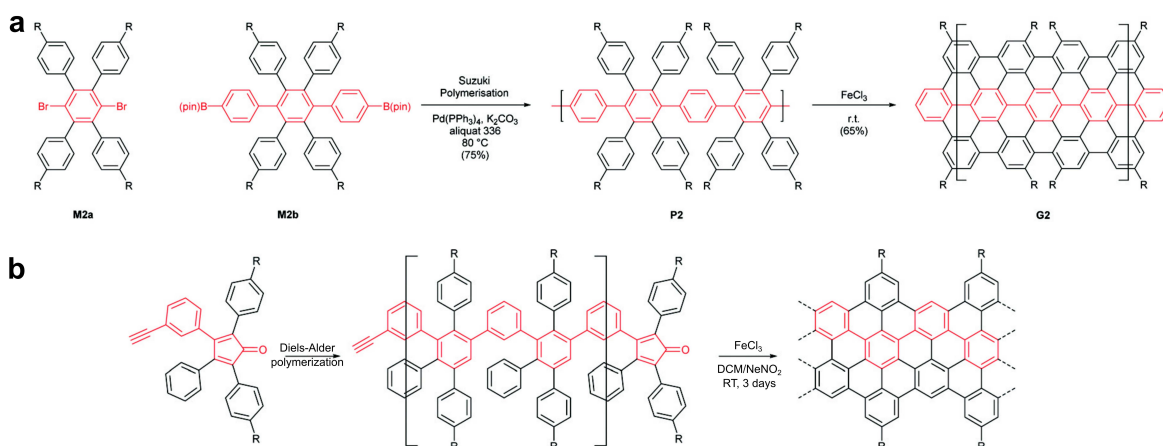


Figure 6.3: Schematic illustration of the solution synthesis of GNRs. *a*, Synthesis of armchair GNR via Suzuki polymerization and graphenisation. *b*, Synthesis of "cove"-type GNR via AB-type Diels-Alder polymerization and intramolecular oxidative cyclodehydrogenation. Adapted from [11, 12, 286].

possible precursors [277, 300]. With specific choice of steric hindrance and reaction path, this can more readily be achieved with solution based approaches [10, 255, 301–304]. As an example of such a process, the synthesis of one of the GNRs studied during this work is presented in Figure 6.4. It consists of selective borylation/monolithiation, followed by AB-type Suzuki polymerization and Scholl reaction. The inclusion of *tert*-butyl groups in specifically chosen positions (marked as residues **R**) induces a twist in the ribbons, achieving non-planarity.

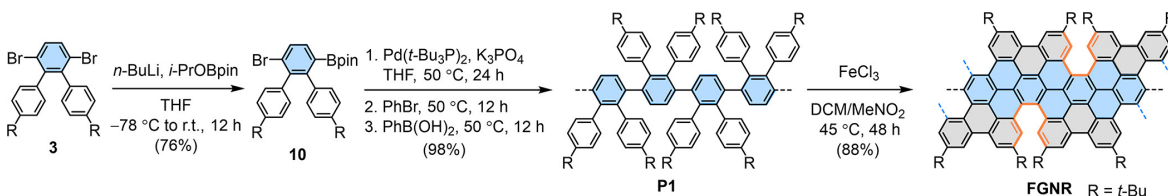


Figure 6.4: Schematic illustration of the synthesis of non-planar GNR. Synthesis of FGNR consisting of selective borylation/monolithiation of **3**, AB-type Suzuki polymerization of **10** and Scholl reaction of **P1**. Reproduced from [10].

Solution based approaches remove the need for metal surfaces or the specific design of the precursors with the specifically chosen surface in mind [109, 278, 279]. This could allow investigations of even fragile nanoribbons on a variety of interesting surfaces, like semi-conductors or insulators for device integration, or fully decoupled from conducting surfaces for fundamental studies. The transfer onto such substrates and especially atomically clean surfaces in UHV, however, largely remains elusive for solvent synthesized GNRs [110, 111, 284, 289, 305–307]. Since with the inclusion of alkyl chains and similar groups even long GNRs can be dissolved in suitable solvents, like toluene, ESD can be applied for the deposition. ESD can both provide molecules with reasonable cleanliness sufficient for high-resolution studies, but also open up the possibility of

accessing the nanoribbons on surfaces inaccessible via different routes.

6.2 Methoxy-GNR

OMeGNR, with its structure visible in Figure 6.1a, is a "cove"-type edged GNR functionalized with methoxy-groups and equipped with alkyl chains (dodecyl) to improve solubility. Its synthesis is performed according to [257]. The methoxy-functionalization was there shown to reduce the band gap and enhance the photoconductivity of GNRs. This is due to a reduction in the effective mass resulting from the methoxy edge functionalization [257].

Even with the inclusion of alkyl chains the solubility for ESD still remains somewhat limited, necessitating low GNR concentrations and a very small part of methanol (20:1 in volume) in the used chlorobenzene/methanol solution. ESD is performed immediately after long sonication to increase dispersion and improve the solubility and, thus, facilitate a higher concentration of GNRs to be deposited on the surfaces while maintaining high cleanliness of the surface. In a first step, after deposition the adsorption and structure of OMeGNR are investigated to both reveal adsorption properties and verify the completeness of the GNRs. In a second step, tip induced manipulations are performed to reveal a high mobility of OMeGNRs on Au(111) surfaces.

6.2.1 Adsorption of OMeGNR

After ESD the OMeGNRs are dispersed on the Au(111) surface, as shown in the topography image in Figure 6.5a.

Multiple well-elongated thin strips of GNR are visible on the three terraces, mostly forming small aggregates. The separation distance between them, however surpasses possible interactions, foremost alkyl chain interactions between the side chains. Measurements of the length performed on all observed OMeGNRs in all acquired images, around 250 GNRs, reveal a close to normal, broad distribution of GNR lengths around an average of 20 ± 7 nm. As illustrated in Figure 6.5b, a minimum of only a few nanometers and a maximum of 42 nm are measured. The broad distribution reveals, as observed for polymers [24], that ESD without mass/charge filtering can provide broadly distributed well-elongated molecules, like GNRs, on surfaces.

On the lower terrace first indication of an alignment to the HB can be seen. This is more clearly shown in the zoomed topography image in Figure 6.5c, where three GNRs are shown aligned to the HB. Here, it is revealed that the nanoribbons are aligned to the hcp region of the HB between elbows. Figure 6.5d provides an illustration of this adsorption position, the OMeGNR is placed over the hcp regions with its alkyl chains pointing outwards over the bridges separating hcp and fcc regions.

Close-up imaging of a single OMeGNR reveals a two lobed structure, as shown in Figure 6.6a. Two parallel higher areas surround a lower area between them, forming an elongated structure. The lower area is attributed to the GNRs, while the two higher lobes are assumed to be formed by the alkyl chains attached to the side of the GNRs (compare structure in Figure 6.1a). The profile in Figure 6.6b taken along the red line

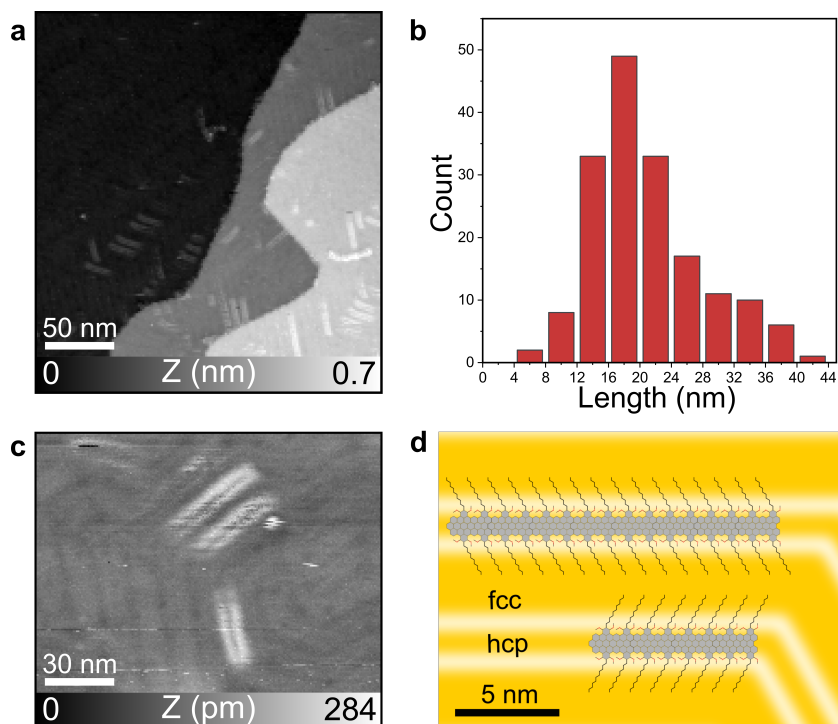


Figure 6.5: OMeGNR on Au(111). **a**, Large scale *nc*-AFM topography image of OMeGNR on Au(111) ($A_2 = 1200$ pm, $\Delta f_2 = -15$ Hz). **b**, Length distribution of OMeGNR on Au(111) measured on all visible OMeGNRs. **c**, *nc*-AFM topography image of OMeGNR adsorption in relation to HB on Au(111) ($A_2 = 1200$ pm, $\Delta f_2 = -16$ Hz). **d**, Illustration of OMeGNR adsorption to hcp region of HB.

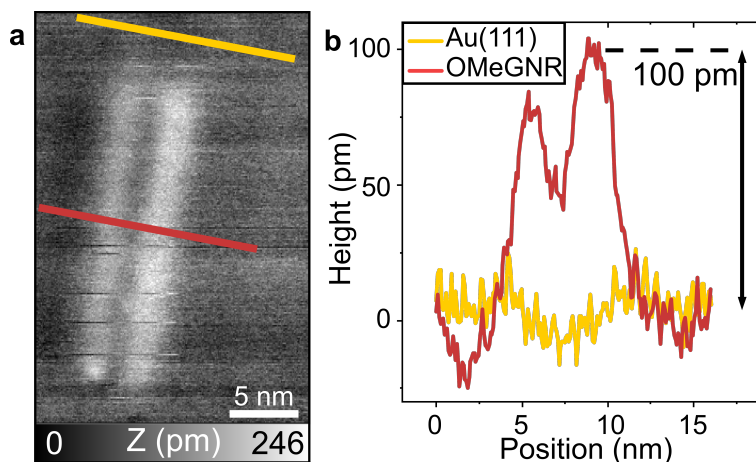


Figure 6.6: Single OMeGNR on Au(111). **a**, *nc*-AFM topography image of a single OMeGNR on Au(111) ($A_2 = 400$ pm, $\Delta f_2 = -30$ Hz). **b**, Height profile along red and yellow line, indicating the positioning over the HB and allowing consideration of its influence.

further illustrates the two lobed structure and reveals a height of up to 100 pm at the maximum of the higher lobe. The yellow line illustrates the HB reconstruction below

the ribbon, showing small influence on the lobe structure and height. The region assigned to the GNR core is measured with a height of about 50 pm. A relatively low flexibility of the ribbons is indicated by the observed uniform structure of the OMeGNR and the straight structure without any turns or wiggles. This fits well with the relatively broad GNR core and its rigid "cove"-type edge structure.

A similar structure was observed in a previous deposition of a "cove"-type GNR (structure in Figure 6.7a) as shown in the topography and torsional frequency shift images in Figures 6.7b and c [179]. There, multiple well-elongated CGNRs can be identified. In topography they exhibit a lobe structure similar to OMeGNRs. A clear identification of the GNR core is facilitated by the torsional frequency shift image in Figure 6.7c. By assigning GNRs from the torsional frequency shift image to the lobes visible in the topography image, further insight into the lobe structure can be obtained. Five GNR cores can be identified but only six lobes are visible. The isolated ribbon on the left side shows two lobes around it, similar to OMeGNR attributed to the side chains. The three GNRs close to the white arrow, however, are surrounded by only three lobes in total, indicating interdigitation of the alkyl side chains. This is supported by the right most GNR. At the white arrow it shows one lobe on its right and one lobe shared with the neighboring ribbons to its left. At the blue arrow, after a turn of the GNR, where no neighboring ribbons are present, lobes are present on both sides of the CGNR. Thus, the chains show one lobe for two ribbons if interdigitated and two lobes if not. Since, both OMeGNR and CGNR show very similar structures, this further supports the attribution of the lobes to the alkyl chains and of the lower area to the GNR core.

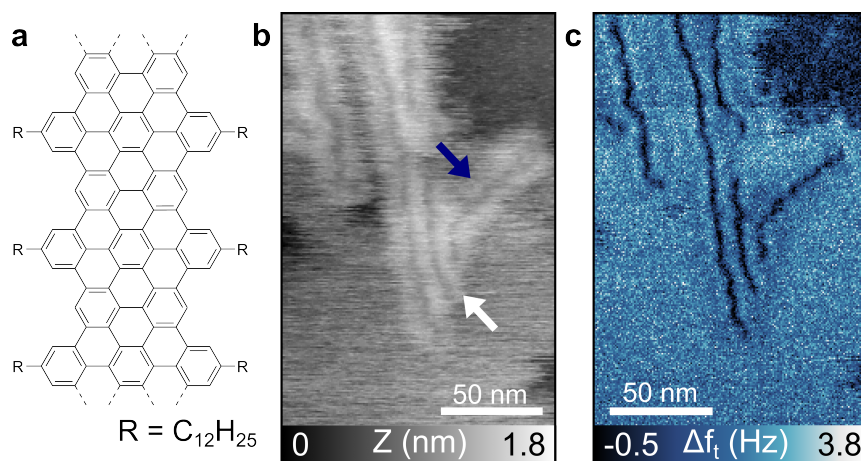


Figure 6.7: Two lobe structure of a "cove"-type GNR. *a*, Chemical structure of CGNR. *b*, nc-AFM topography image of CGNRs. ($A_1 = 2$ nm, $\Delta f_1 = -25$ Hz, $A_t = 80$ pm). *c*, Corresponding torsional frequency shift image. The dark ribbons correspond to the GNR cores, the lobes in the topography are assigned to the alkyl chains. Adapted from [179].

The OMeGNRs are, thus, distributed well over the surface with their structure preserved after ESD. Since an exact length specific synthesis is difficult for GNRs

and polymers, the wide distribution observed, further, indicates the power of ESD for depositing broadly length distributed molecules for fundamental studies.

6.2.2 Room Temperature Manipulation of Solution Synthesized GNR

Spatial control along with precise manipulation of molecules or ribbons, especially of single ones, is essential for applications in nanotechnology. Manipulations with SPM have been performed on a multitude of molecules and also nanoribbons since the first manipulations in 1990 [308–310]. At LT, thanks to low drift, single molecules, GNRs, or polymers have been moved, precisely repositioned by tip induced manipulation with STM [310–317]. For example this facilitates the positioning of GNRs on thin insulating layers on conducting surfaces [260,265,270]. RT manipulations, impressively, have also been performed down to single atom level both with STM and nc-AFM, but also on molecules and their assemblies [165,318–323].

Imaging of OMeGNRs at room temperature reveals a high mobility of the nanoribbons on Au(111) surfaces facilitating such tip induced manipulations. The tip induced manipulations are performed by scanning over an isolated OMeGNR with a relative small amplitude. This allows an unusually close average position of the tip in respect to the surface. In addition, to further decrease the distance, a second pass with an offset towards the surface is added in multipass. If no manipulation is achieved, the frequency shift set point can be further reduced to reduce the tip-sample distance. A schematic illustration is provided in Figure 6.9a.

Figure 6.8a shows a large scale nc-AFM topography image of OMeGNR, visible are an isolated OMeGNR and a step edge of the Au(111) forming a kink, which will in the following be used as a marker to quantify the movement of the GNR. In the initial state a separation from the kink of 25 nm is observed. A close-up topography image before the manipulation is presented in Figure 6.8b showing the expected double lobed structure and will serve as a comparison to verify preservation of the GNR structure upon manipulation.

In a first step, manipulation of the OMeGNR induced a repositioning in y -direction by 20 nm. The position of the nanoribbon after this manipulation is visible in the nc-AFM topography image in Figure 6.8c, where the distance to the kink is marked. After the manipulation imaging resolution is degraded, but the two lobed structure and the length of the GNR can still be distinguished to show the nanoribbon to be intact and of the same length in the close-up topography image in Figure 6.8d.

A second step of manipulation was induced by again scanning the tip over the GNR and approaching closer to reduce the tip-sample distance. During the scan, shown in Figure 6.8f, two events of manipulation, indicated by the red arrows, are visible. While performing the upwards performed scan, the ribbon was first moved to the right in x -direction by around 15 nm, where it was again observed adsorbed over the HB. Then, another displacement out of the scan frame occurred after most of the ribbon was scanned. This resulted in a manipulation of the GNR by another 25 nm in y -direction and 30 nm in x -direction, as visible in the large scale topography image in Figure 6.8e.

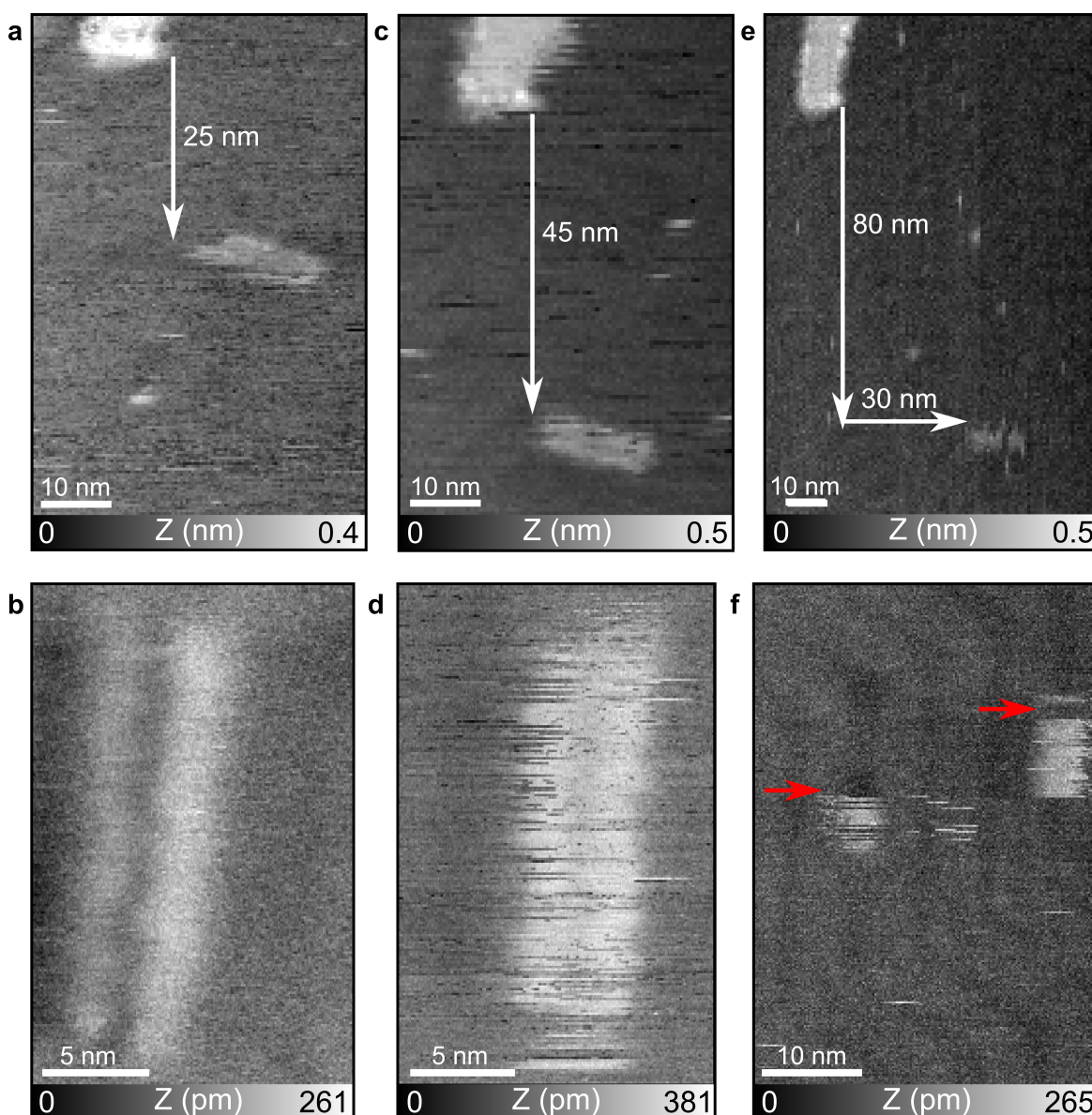


Figure 6.8: Tip induced manipulation of OMeGNR on Au(111). **a**, Large scale *nc-AFM* topography image of OMeGNR on Au(111) before tip induced manipulation steps. ($A_2 = 400$ pm, $\Delta f_2 = -26$ Hz). **b**, Close-up *nc-AFM* topography image of the OMeGNR before manipulation ($A_2 = 400$ pm, $\Delta f_2 = -30$ Hz). **c**, Large scale *nc-AFM* topography image of OMeGNR on Au(111) after first tip induced manipulation ($A_2 = 400$ pm, $\Delta f_2 = -26$ Hz). **d**, Close-up *nc-AFM* topography image after tip induced manipulation ($A_2 = 400$ pm, $\Delta f_2 = -30$ Hz). **e**, Large scale *nc-AFM* topography image of OMeGNR on Au(111) after second tip induced manipulation ($A_2 = 200$ pm, $\Delta f_2 = -25$ Hz). **f**, *nc-AFM* topography image during tip induced manipulation. Two manipulation events are marked by the red arrows ($A_2 = 200$ pm, $\Delta f_2 = -25$ Hz).

There, the nanoribbon and the marker step are visible with the separation marked.

A last manipulation occurred from the previous position, during the scan for the

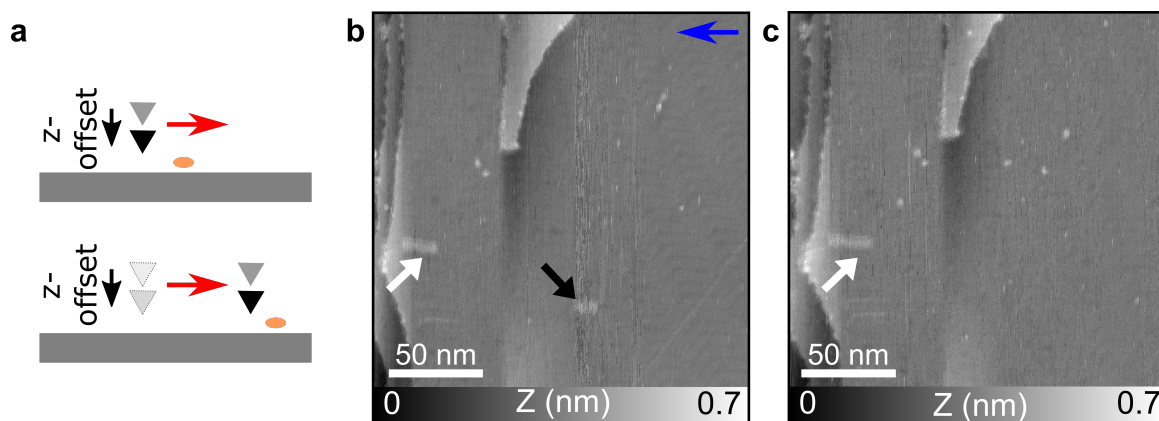


Figure 6.9: Large scale tip induced manipulation of OMeGNR on Au(111). **a**, Scheme illustrating the manipulation process. The red arrow indicates the fast scan axis. **b**, Large scale nc-AFM topography image of OMeGNR during manipulation. The slow scan axis is marked with a blue arrow, the manipulated OMeGNR with a black arrow and an unaffected GNR in white ($A_2 = 200$ pm, $\Delta f_2 = -25$ Hz). **c**, Large scale nc-AFM topography image of OMeGNR on Au(111) after the last tip induced manipulation. The manipulated OMeGNR is no longer observed in the scan area, the unaffected OMeGNR marked by a white arrow ($A_2 = 200$ pm, $\Delta f_2 = -25$ Hz).

large scale topography image in Figure 6.9b. The manipulated OMeGNR is marked by the black arrow. Of note, is the scan direction, the slow scan axis is oriented along the blue arrow going from right to left. Clearly visible are instabilities when scanning over the isolated OMeGNR along the fast scan axis. No such instabilities are observed for another OMeGNR visible at the steps on the left side of the image, marked by a white arrow. As can be seen in the next scan, shown in Figure 6.9c, the previously manipulated OMeGNR was moved outside of the large scan frame, indicating a displacement of at least 50 nm most likely along the scan axis. Further, manipulation steps were not performed on this GNR since later scans did not reveal its position. Since multiple scans were performed, it might have been moved further towards a step or adsorbed to the tip. As can be seen by the OMeGNR at the step, marked by the white arrows in Figures 6.9b and c, the ribbons are bound strongly at the steps, no manipulation occurred.

From the observations of the displacements, the precise mechanism of repositioning can not be ascertained. A strong indication is given by the two observed displacement events in Figure 6.8f. Since the ribbons are repositioned from one scan line to the next, likely a jump-wise manipulation occurred. This points to a somewhat weak adsorption to the surface, since the manipulations were performed with relatively large tip-sample distance, and a rigid structure of the ribbons. In combination with the adsorption along fcc/hcp bridge of the HB this could promote the jump-wise motion. Precise insight in the manipulation could be provided by MD simulations, which, unfortunately lie outside the scope of this work.

6.3 Fjord-GNR

FGNR, structure shown in Figure 6.1b, is a fjord-edged GNR equipped with *tert*-butyl groups. The fjord refers to the two benzene rings deep opening in the edge/structure of the GNR, each flanked by a *tert*-butyl on either side [10]. FGNR is designed to provide high flexibility thanks to its deep cut edge and importantly a twisted non-planar structure caused by steric hindrance of the *tert*-butyl groups. At the same time, the side groups help improve the solubility, facilitating ESD. As indicated above, such GNRs are of high interest thanks to their possible uses in non-linear optics, nanomechanics and asymmetric catalysis [10, 298, 299].

6.3.1 Fjord-trimer Precursor Molecule

The smallest subunit of FGNR, still containing a fjord-edge was studied on Au(111) to provide comparison to the completed FGNR and gain insight into the FGNR structure. In addition, on surface reactions and resulting structural changes can impressively show the challenges faced for on surface synthesis of ribbons or molecules with similar structures. The chemical structure of the precursor model, a fjord-trimer, is shown in Figure 6.10a.

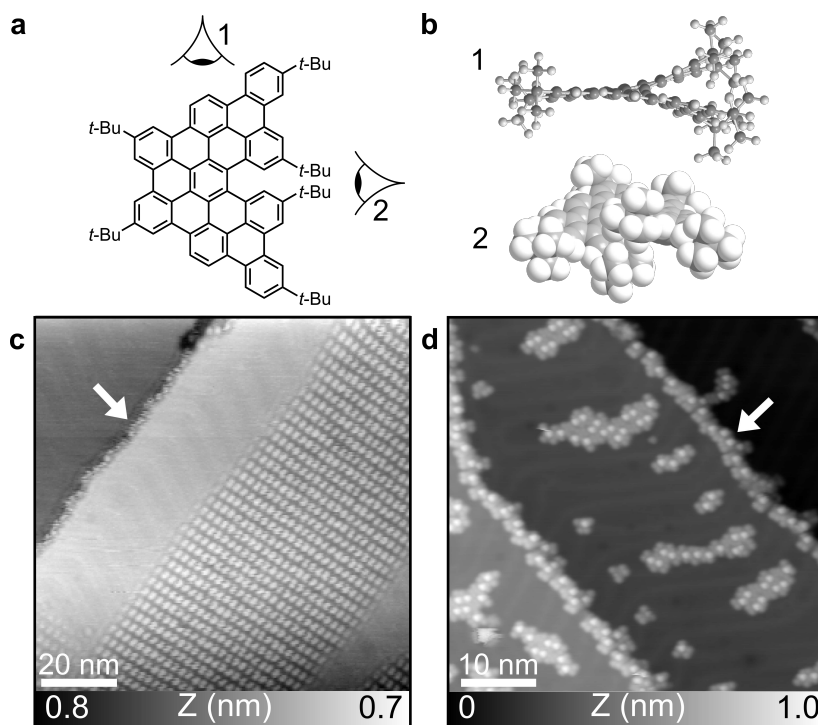


Figure 6.10: f-trimer on Au(111). **a**, Chemical structure of fjord-trimer. **b** Models illustrating the non-planar structure of f-trimer from the marked perspectives. **c**, Large scale nc-AFM topography images of f-trimer molecule assembly on Au(111) at 300 K ($A_1 = 3$ nm, $\Delta f_1 = -18$ Hz) and **d**, at 5 K. A preferential adsorption on the HB elbows is visible ($I = 1$ pA, $V_{Bias} = -200$ mV).

Chapter 6. Solution Synthesized Graphene Nanoribbons on Surfaces by ESD

Analogously to the completed GNR, each fjord is decorated by *tert*-butyl groups on either side. As illustrated in the models in Figures 6.10b, this is expected to induce tilting of the molecules around the fjord due to steric hindrance between the *tert*-butyl groups. The precursors are specifically designed as a model and are not equipped with halogens for on-surface synthesis, but are well suited for comparison to the completed FGNR.

Upon deposition by TE, the f-trimer molecules form large scale assemblies at 300 K when sufficient coverage is obtained. The nc-AFM topography image at RT in Figure 6.10c shows a large well-extended islands on the Au(111) surface terrace isolated from the step edges. The step edges are fully covered, as indicated by the white arrow. As explained above, they are preferential adsorption sites. Interestingly, the island forms at the elbows of the herringbone with the first nucleation likely occurring there [34, 171].

Similarly, also the STM topography image of lower coverage at 5 K shows islands on the terraces and covered step edges (white arrow) in Figure 6.10d. Here, also isolated molecules are visible situated on the elbows confirming them as the preferential adsorption sites. Zoomed nc-AFM topography images of an island at 300 K reveal a line structure in the assembly networks, as can be seen in Figure 6.11a.

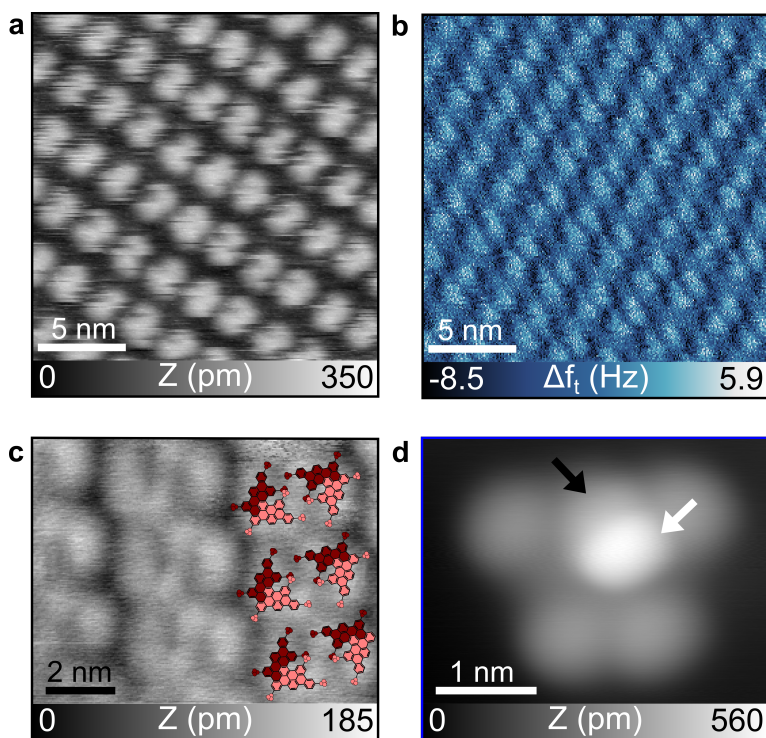


Figure 6.11: Adsorption of f-trimer. **a**, nc-AFM topography image of f-trimer network inside an island and **b**, corresponding torsional frequency shift image revealing a dimer structure ($A_1 = 2 \text{ nm}$, $\Delta f_1 = -30 \text{ Hz}$, $A_t = 80 \text{ pm}$). **c**, Close-up nc-AFM topography image zoomed on f-trimer assembly lines ($A_1 = 3 \text{ nm}$, $\Delta f_1 = -16 \text{ Hz}$). **d**, High-resolution STM topography image of a single f-trimer molecule at 5 K showing non-planarity ($I = 1 \text{ pA}$, $V_{Bias} = -200 \text{ mV}$).

The corresponding torsional frequency shift image (Figure 6.11b) reveals such lines to consist of f-trimer molecule dimers.

Zooming on a single line in such an assembly, as shown in Figure 6.11c, reveals the precise adsorption of the f-trimers in their dimers. The two molecules are positioned opposite of each other with a slight lateral shift. Their fjord-edges are, thereby, aligned inwards, towards a lobe of the other f-trimer. To illustrate this, molecule structures are superimposed over one dimer line.

In the molecules a first indication of the desired non-planarity can be observed. Along the molecule, as shown by the color scale in the superimposed structures, the height undergoes a slight increase.

This is confirmed by the high-resolution STM topography image of an isolated f-trimer molecule at 5 K shown in Figure 6.11d. There, the right side of the molecules shows a prominent increase in height. The higher domain of the molecule can be attributed to a twist of the right lobe of the molecule upwards and the *tert*-butyl fixed to its side of the fjord. This is, as expected from the model, due to steric hindrance of the *tert*-butyls of the fjord. One of them points upwards and the other one is pointing downwards, as marked by the arrows (white upwards, black downwards). The LT STM topography image also resolves the trapezoid shape of the f-trimer, showing its completeness and giving a nice comparison for the following studies of the completed FGNR.

To study possible on-surface reactions and ensuing structural changes of the f-trimer, especially as a stand-in for FGNR, an annealing step at around 200 °C was performed. Resulting molecules are shown in the LT STM topography image in Figure 6.12a.

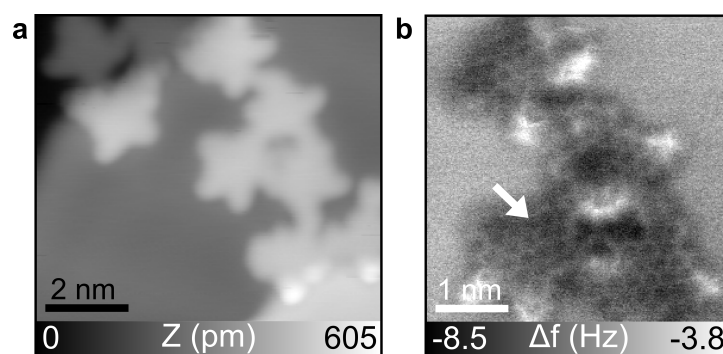


Figure 6.12: On-surface reaction of f-trimers. **a**, LT STM topography image of flattened f-trimers after annealing ($I = 1$ pA, $V_{Bias} = -350$ mV). **b**, Zoomed constant height AFM image revealing the resulting bond structure ($A = 140$ pm).

Notably, the molecules no longer show the previously observed twist-induced height difference, instead their structure shows a mostly flat butterfly-like structure. The AFM constant height image at LT, shown in Figure 6.12b, reveals the flat and bonded structure with the fjord closed, as indicated with the white arrow. The *tert*-butyl groups in the fjord dissociated and bonds were formed to close the fjord. This removes the steric hindrance inducing the twist and, therefore, results in the observed flattening of the molecule structure. Transferring this insight to the FGNR, impressively

Chapter 6. Solution Synthesized Graphene Nanoribbons on Surfaces by ESD

exemplifies the difficulties of forming ribbons with such a twisted non-planar structure by on-surface synthesis, where often times annealing up to 400 K is necessary for cyclodehydrogenation [107, 108, 300].

6.3.2 Adsorption of FGNR

FGNR upon deposition on Au(111) by ESD reveals similarly dispersed coverage to OMeGNR, isolated nanoribbons with different lengths are observed on multiple terraces, however, in contrast no aggregates are found. Each FGNR is isolated as visible in the large scale topography image in Figure 6.13a.

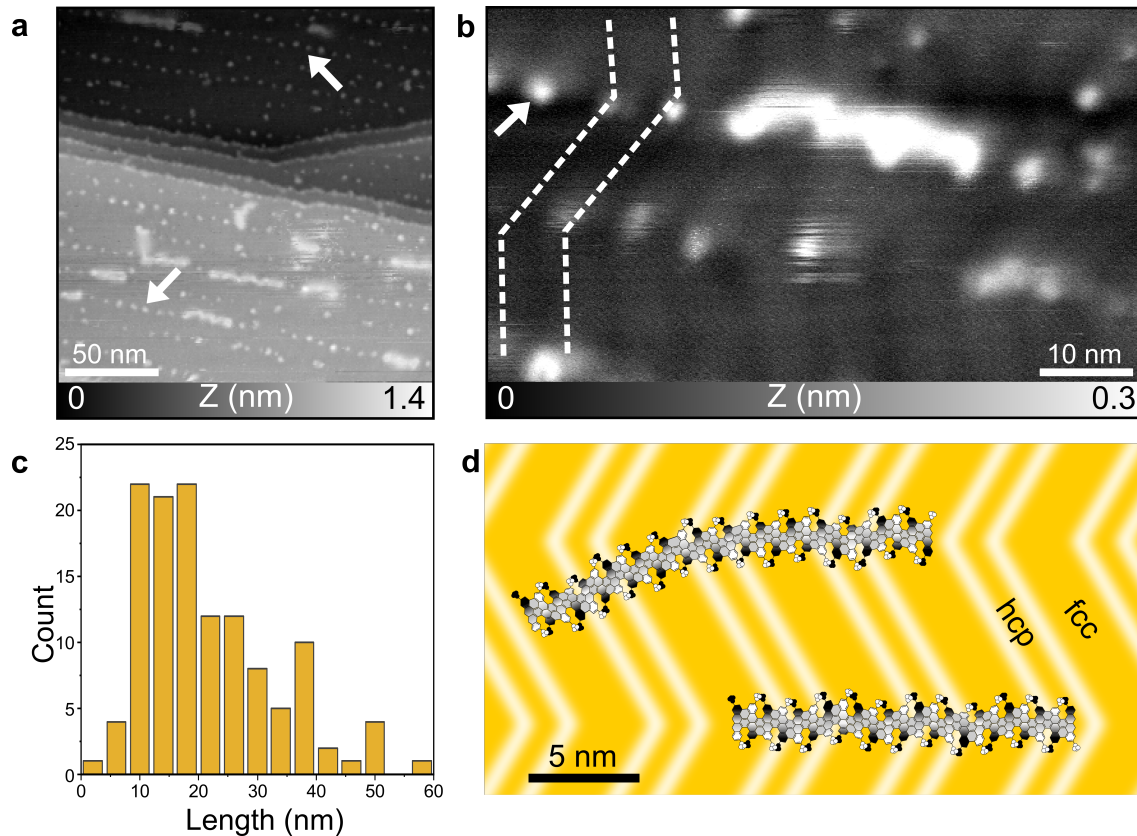


Figure 6.13: FGNR on Au(111). **a**, Large scale nc-AFM topography image of FGNR on Au(111) ($A_1 = 3$ nm, $\Delta f_1 = -20$ Hz). **b**, Adsorption of FGNR on HB elbows, contrast modified ($A_1 = 3$ nm, $\Delta f_1 = -20$ Hz). **c**, Length distribution of FGNR on Au(111). **d**, Illustration of adsorption of FGNR on Au(111) along HB elbows. The white areas are further from the surface, the black domains closer.

Already at this large scale a clear difference in the flexibility of the GNRs is revealed. Instead of the rigid uniformly straight and planar OMeGNR, a more wiggly structure is observed for FGNR. Interestingly, small dots, marked by the white arrows in Figures 6.13a and b, are visible on the surface forming line like structures. As reported for the spray depositions of C₆₀ on Au(111) and Ag(111) above (compare Section 3.5), these can be attributed to remaining solvent adsorbed to the elbows of the HB [34]. Since the FGNRs are generally aligned in line with the spotted lines, this indicates positioning along the elbows. A zoom on a single FGNR with modified contrast, presented in Figure 6.13b, confirms this. The wiggly nanoribbon is aligned with the elbows of the HB, indicated by the dotted line, and, thus, crosses over the

fcc and hcp regions. An illustration of this adsorption is provided in Figure 6.13d, where two FGNRs with their wiggly structure reproduced are positioned over the HB on an Au(111) surface. One is more straight as seen in Figure 6.13a, but still twisted, while the one in the bottom shows clear bending based on the FGNR in Figure 6.14a. The twisting structure of the ribbons is illustrated by the color scale. Higher areas are white while lower are marked as darker.

Analysis of the length of all detected FGNRs in all measurements provides the distribution shown in Figure 6.13c. A slightly more dispersed variation in length is observed for FGNR than for OMeGNR, reaching from few nanometers to up to 60 nm in length. The observed average length of 21 ± 11 nm corresponds well to measurements obtained after synthesis based on the molecular weight distribution, where 17 nm was found [10]. This indicates that no limitation of the length by the ESD occurred and each length of FGNR could be deposited and observed on the surface.

Close-up imaging allows resolving the wiggly structure of FGNR more clearly as can be seen in Figure 6.14a. The wiggly structure is prominently visible from the turns and kinks in the presented single FGNR. Bending of GNR has been previously observed, but the tight twists observed here indicate a significantly increased flexibility when compared to both OMeGNR and previously reported armchair GNR [324]. Some flexibility or mobility of the nanoribbon is observed by the slightly jumping lines in the scan over the GNR below the yellow line. The profile corresponding to that line, shown in Figure 6.14c, indicates a maximum height of 300 pm and a quite uniform profile with a core width of about 2 nm.

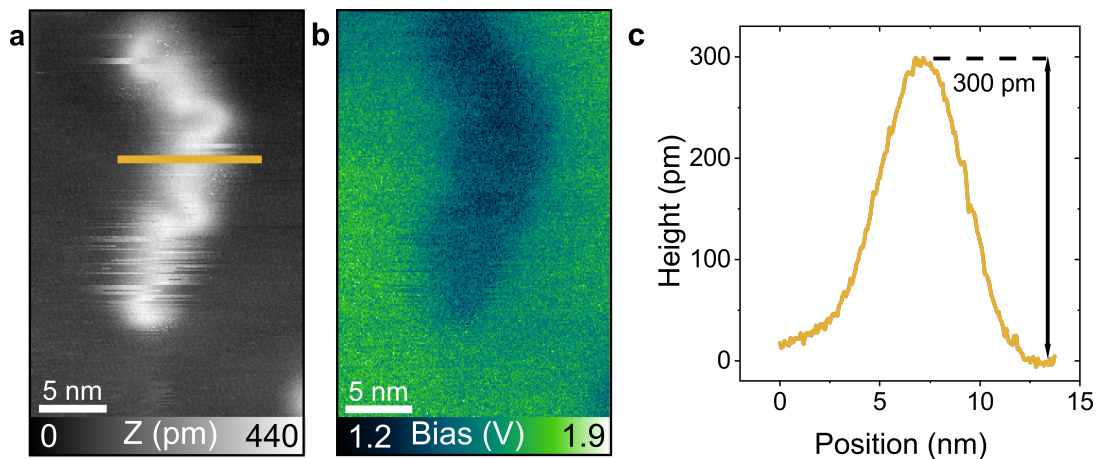


Figure 6.14: Single FGNR on Au(111). **a**, Zoomed *nc*-AFM topography image of a single FGNR on Au(111). The wiggly structure of the molecule indicates a flexible structure ($A_1 = 3$ nm, $\Delta f_1 = -20$ Hz). **b**, Corresponding CPD image revealing a more *p*-doped state of FGNR compared to pristine graphene. **c**, Height profile along yellow line.

CPD measurements (Figure 6.14b) obtained simultaneously by KPFM in sample bias, indicate a CPD difference between the Au(111) surface and the FGNR of about 500 mV. From this we can estimate the local work function of FGNR on Au(111) to be around 4.8 eV, which is consistent with the expected value of GNR on metal

surfaces [325]. This higher work function value compared to a graphene monolayer measured in similar condition points towards a more p-doped state of FGNR compared to pristine graphene [326,327].

6.3.3 Non-planarity of FGNR

Indicated by the flexible nature of FGNR predicted upon synthesis [10] and confirmed by imaging of its precursor molecules, high-resolution imaging in combination with multipass can reveal a twisted non-planar structure of FGNR on the surface. Figure 6.15a provides a high-resolution nc-AFM topography image of a FGNR obtained in the first pass of a multipass scan. The internal structure of the FGNR is revealed in the corresponding second pass frequency shift image shown in Figure 6.15b. There, repeating protrusions are visible alternating on both sides of the FGNR separated by about 850 pm along one side as indicated by the white arrow. This fits well with the distance between two fjord-groups of the FGNR and is, thus, attributed to the *tert*-butyls, attached to the sides of the fjord edges.

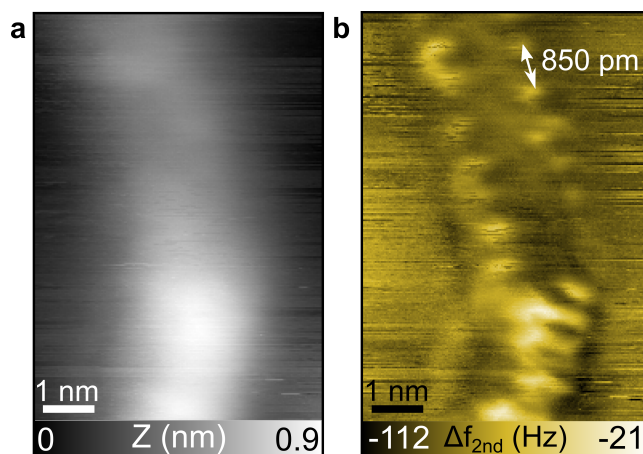


Figure 6.15: Non-planarity of FGNR. **a**, Close-up nc-AFM topography image of a single FGNR on Au(111) showing a height increase in the molecule ($A_1 = 5$ nm, $\Delta f_1 = -45$ Hz). **b**, Corresponding second pass frequency shift image showing the *tert*-butyls of the fjords and the non-planar structure.

Each protrusion, thereby, corresponds to one of the *tert*-butyls pointing upwards at the sides of fjords, the other one points downwards towards the surface as was shown for the f-trimer in Figure 6.11d. This also involves a twisting of the ribbons structure between each fjord-edge due to the aforementioned steric hindrance. The positioning of *tert*-butyls and this twist in FGNR is illustrated in the adsorption model in Figure 6.13d, where the color scale indicates different heights in the ribbons and direction of the *tert*-butyls in respect to the surface (white higher/upwards, black lower/downwards). In the lower part of the GNR a turn is visible. There, an increasing height is visible in the topography (Figure 6.15a). At the same time the protrusions start to become more elongated and their separation distance is increased (Figure 6.15b). In addition, the right side of the FGNR appears increasingly higher - the frequency

shift is more and more in the repulsive regime. We attribute this to a strong twist of FGNR in the turn on the surface. The core of the nanoribbon is turned upwards on one side leading to the *tert*-butyls no longer being presented upwards towards the tip and the internal structure becoming distorted. Thus, the non-planar nature of FGNR, as expected from synthesis and precursors, is confirmed with the internal structure of FGNR and the observed twisting of the ribbon in its turn.

6.4 Solution Synthesized GNRs on Non-metallic Surfaces

Deposition of molecules on non-metallic surfaces and especially insulating ones is of special interest due to the possibility to decouple the molecules electronically from the surface, which otherwise strongly influences their properties [48, 49].

This is especially interesting for GNRs which can show remarkable electronic properties [242–245], tunable by edge functionalization and the addition of heteroatoms as mentioned above [108, 252, 255, 256].

As shown in Chapter 3.5, ESD is, when taking into account possible surface modifications, generally not limited to any specific surface, as long as sufficient cleanliness can be guaranteed. This allows the deposition of the well-soluble FGNR on two non-metallic surfaces, the bulk insulator KBr(001) and the semi-metal HOPG.

ESD of FGNR on KBr(001) without any post-deposition annealing results in a typical KBr(001) surface, exhibiting large terraces separated by few monoatomic steps. Notably, elongated structures, the GNRs, are visible mostly isolated from the steps, which are partially covered, likely in remaining solvent, as shown in Figure 6.16a.

The FGNRs exhibit their previously observed wiggly structure already in the large scale topography image. In some areas at the steps and on top of the terraces, irregularly shaped islands with rounded edges are observed. Atop those, often times single or multiple GNRs are present. One such island is visible in the zoomed topography image in Figure 6.16b. There, FGNRs are visible both on the terrace itself and also on a small island in the top right corner. On the island, three FGNRs are present, all showing the distinct wiggly structure previously observed. The flexibility due to the fjord-edge, thus, seems to be maintained. Since the height of the islands is similar to that of KBr single steps, as shown in the profile in Figure 6.16c, and the islands are present even after an annealing step, they can be attributed to KBr, removed from the surface during deposition, as shown in previous chapters [21, 34]. The positioning of the FGNRs on the surface and islands is illustrated in Figure 6.16d. Notably, no craters or similar large scale modifications were observed in contrast to ESD with C₆₀ in Section 3.5, pointing towards a less intensive deposition procedure even with the much larger FGNRs.

Zoomed nc-AFM imaging of a single FGNR on a terrace, reveals the presence of further mobile species around each nanoribbon even after an annealing step. As can be seen in Figure 6.17a, the wiggly structure of FGNR is preserved on KBr(001), the ribbon exhibits two turns, similar to what was observed on Au(111) in Figure 6.14.

6.4. Solution Synthesized GNRs on Non-metallic Surfaces

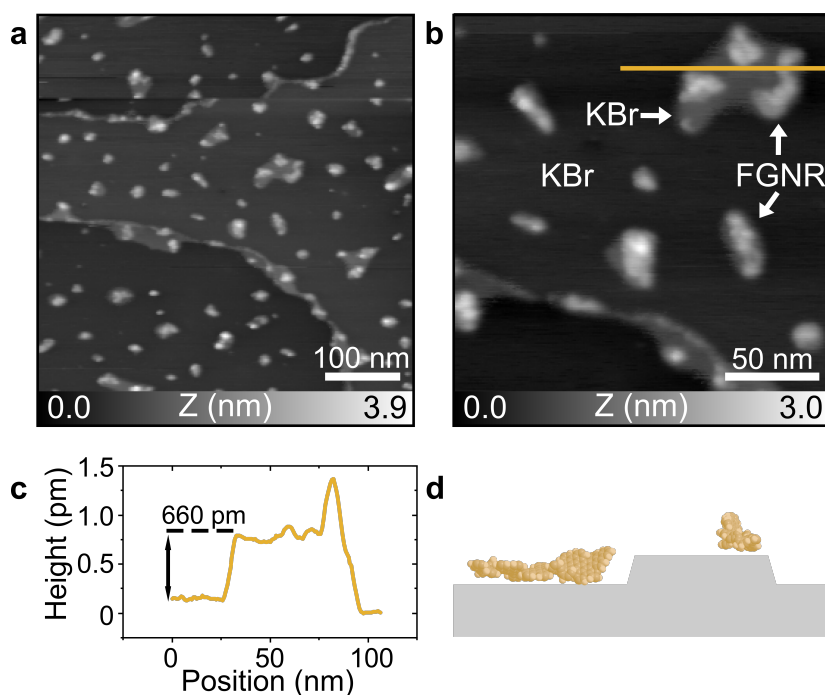


Figure 6.16: FGNR on KBr(001). *a*, Large scale nc-AFM topography image of FGNR on KBr(001). FGNRs are visible on terraces and small islands ($A_1 = 5$ nm, $\Delta f_1 = -8$ Hz). *b*, Zoomed nc-AFM topography image of FGNR on KBr island on KBr(001) ($A_1 = 5$ nm, $\Delta f_1 = -8$ Hz). *c*, Profile along yellow line over KBr island in *b*. *d*, Scheme of FGNR on KBr. FGNR is adsorbed both on the KBr island and on the terrace.

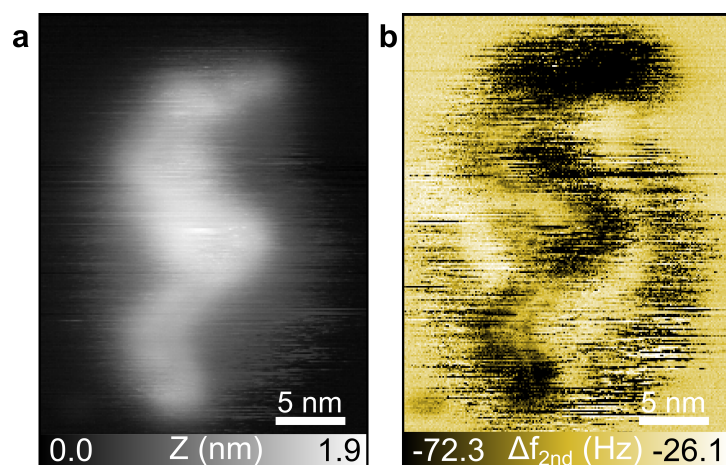


Figure 6.17: Single FGNR on KBr(001). *a*, Zoomed nc-AFM topography image of a single FGNR on KBr(001) showing the aforementioned wiggly structure. ($A_1 = 3$ nm, $\Delta f_1 = -20$ Hz, $A_t = 80$ pm). *b*, Corresponding second pass frequency shift image revealing mobile species around the FGNR.

Chapter 6. Solution Synthesized Graphene Nanoribbons on Surfaces by ESD

Of note, however, is the large instability and mobility at the edges of the FGNR. In the second pass frequency shift image in Figure 6.17b the presence of the nanoribbon is visible in the middle of a more unstable area. The mobile species is, also, attributed to KBr removed from the surface, since even after the annealing step the species is observed. If solvent was present, it would likely be reduced after the annealing, but this is not the case here [21].

The integrity of FGNR on KBr(001), even after an annealing at 250°C, is shown with high-resolution imaging of an aggregate of ribbons visible in Figure 6.18a. The elongated structure with strong bends is revealed to consist of at least two ribbons in the close-up torsional frequency shift image of the white marked area. As can be seen in Figure 6.18b, the ribbons, marked by the white arrows, are closely aligned to each other. At the yellow arrows periodic, slightly elongated, protrusions with a distance close to the expected *tert*-butyl/fjord separation are observed. These can again be attributed to the *tert*-butyls at the fjord-edges, indicating that the ribbons are deposited intact.

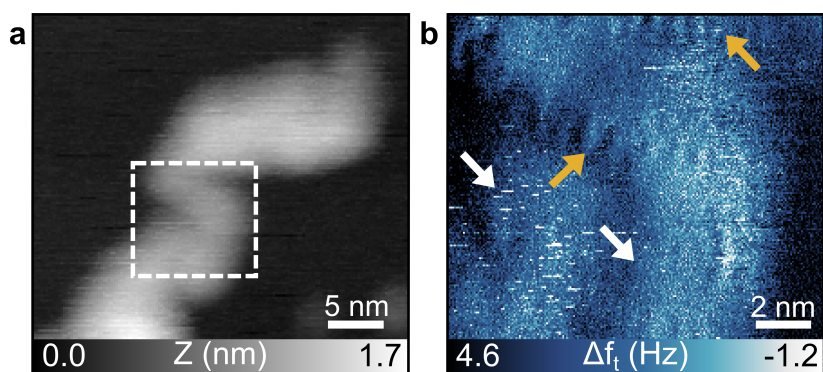


Figure 6.18: Submolecular resolution of a FGNR assembly on KBr(001). **a**, *nc*-AFM topography image of a FGNR aggregate on KBr(001). ($A_1 = 5$ nm, $\Delta f_1 = -10$ Hz). **b**, Zoomed torsional frequency shift image of the white marked area distinguishing two ribbons indicated by the white arrows. At the yellow arrows protrusions of the *tert*-butyls of the fjords are visible ($A_1 = 3$ nm, $\Delta f_1 = -26$ Hz, $A_t = 80$ pm).

Deposition of FGNR on KBr(001), therefore, results in the expected structure with only relatively minor modification of the surface and small presence of solvent, well suitable for high-resolution studies. Their even more pronounced wiggly structure follows from the lower interaction with the KBr surface.

On HOPG depositions were slightly less clean, but still successful. HOPG was chosen due to its semi-metallic properties and the carbon structure, graphene being a single 2D layer of graphite. After ESD, small clusters of multiple closely aligned FGNRs are observed on the HOPG surface in the large scale topography image in Figure 6.19a. Also, present are large and often high, unstable areas, likely from remaining solvent. These are prominently visible below the GNR cluster. A zoomed topography image on the FGNRs reveals the expected twisted and turning structure even in the clusters, but also points to close packing of the FGNRs together, as visible in Figure 6.19b.

6.4. Solution Synthesized GNRs on Non-metallic Surfaces

GNR separation is on the scale of less than 1 nm. Solvent pollution can more clearly be distinguished by the energy dissipation image in Figure 6.19c [55]. The yellow arrow points to the same area in dissipation and topography images. While a height difference and, thus, a structure is observed in the topography, no dissipation difference to the baseline of the surface can be observed. Since other regions show prominent signals, this indicates that the unstable topography areas stem from solvent, which is generally observed not to show a dissipation signal in contrast to larger molecules [55, 241, 328, 329].

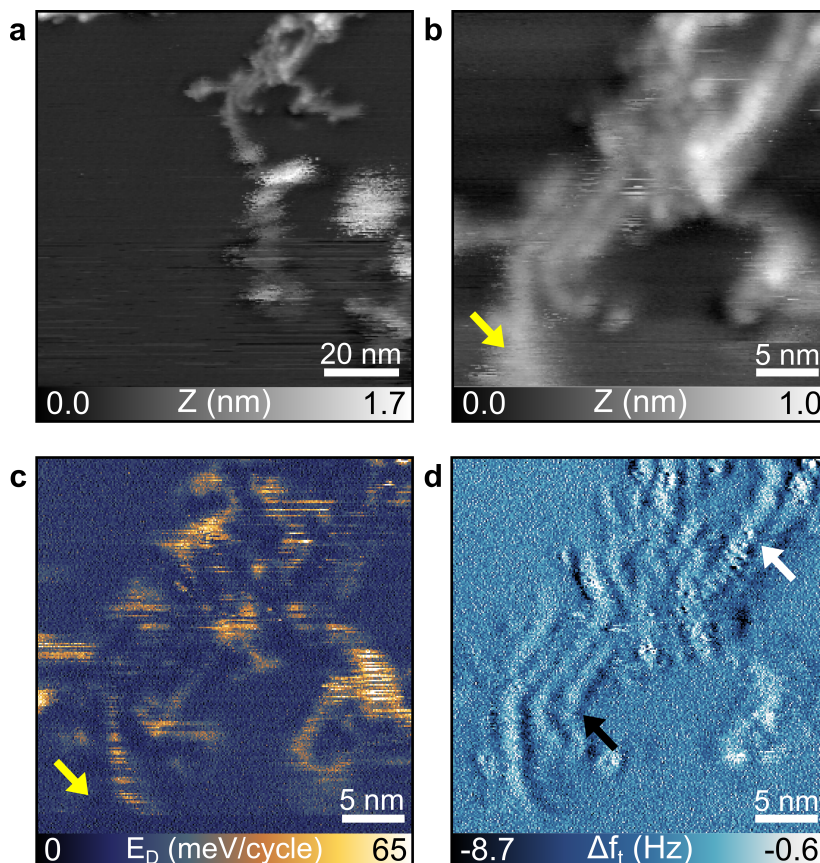


Figure 6.19: FGNR on HOPG. **a**, Large scale *nc*-AFM topography image of FGNR on HOPG. FGNRs and solvent pollution are visible. ($A_1 = 5$ nm, $\Delta f_1 = -10$ Hz). **b**, Zoomed *nc*-AFM topography image of FGNR on HOPG ($A_1 = 5$ nm, $\Delta f_1 = -20$ Hz, $A_t = 40$ pm). **c**, Corresponding dissipation image distinguishing solvent and FGNRs. **d**, Corresponding torsional frequency shift image revealing the internal structure of FGNR at the white arrow and an increase in height at the black arrow indicating non-planarity.

Confirmation of the molecular structure of the FGNRs is obtained from the corresponding torsional frequency shift image shown in Figure 6.19d. The elongated structures are resolved similar to in the topography image. At the turns of the GNRs, marked by the black arrow, a slight height difference is observed, the ribbons appear more clearly resolved at the bottom. This points towards the previously observed

non-planar structure of FGNR. Interestingly, the torsional frequency shift image also allows resolving the inner structure of the FGNR. At the white arrow in Figure 6.19d, protrusions with a distance around 850 pm, the aforementioned distance between two fjord-edges, are observed. The high sensitivity of the torsional mode to lateral forces on flat surfaces, suggests that these correspond to the fjord-edges and their *tert*-butyl groups and, thus, the completeness of the FGNR. ESD can therefore provide even the possibility of depositing large and well-elongated molecules inaccessible on non-metallic and especially insulating surfaces with a high degree of cleanliness sufficient for submolecular resolution studies. This can allow the study of new types of solution synthesized molecules, prominently GNRs, even with non-planar properties.

6.5 Summary

In this chapter, the adsorption and structural properties of two solution synthesized GNRs were studied after deposition by ESD. In a first part, two approaches to synthesis along with their limitations and possibilities were discussed. Then, a methoxy-functionalized CGNR was studied showing a rigid planar structure adsorbing along the HB of Au(111). A high mobility of the OMeGNR on Au(111) was investigated next by performing a multi step tip-induced manipulations on an isolated GNR.

In a second part, a fjord-edged GNR, predicted to exhibit a non-planar twisted structure was deposited. First, a subunit of the FGNR was deposited by TE, revealing an adsorption in islands forming from HB elbows on Au(111) at RT. High-resolution studies show a dimeric structure and confirm the non-planarity. STM/AFM investigations at LT reveal isolated molecules allowing precise confirmation of the twisted structure and possible on-surface reactions.

Then, the ESD of the FGNR was performed, on both metal and non-metallic surfaces. Studies on Au(111) reveal adsorption along the elbows of the HB in a wiggly flexible structure. High-resolution studies resolve the internal structure of the GNR and reveal the desired non-planar twisted structure. Investigations on the non-metallic surfaces, reveal the molecules to be complete on the surface with limited influence on the surface morphology, opening up the possibility of studies on previously not available surfaces and decoupling of the surfaces.

Conclusion

FUNCTIONAL materials formed by self-assemblies or structures of molecules deposited on atomically clean surfaces can provide important new properties and functionalities, when access to complex, larger molecule precursors is afforded. Due to their larger size, the possible inclusion of fragile functional groups and the ensuing greater risk of dissociation, such molecules require advanced deposition methods, like electrospray deposition.

In this thesis, ESD was used to deposit various large and complex molecules on surfaces in UHV to form two-dimensional supramolecular islands to study their properties and functional response to stimuli with nc-AFM and LT STM/AFM. Furthermore, solution synthesized GNRs and their newly accessible structures were investigated in high-resolution SPM studies after ESD on previously not reachable surfaces in UHV.

The experimental principles, methods and realizations of nc-AFM at RT and STM as well as AFM at LT in UHV facilitating this work were introduced in Chapters 1 and 2.

Thereupon, in Chapter 3 the electrospray deposition method was evaluated for its applicability to achieve similar molecular adsorption to the commonly used thermal evaporation method even with fragile functional molecules. It was shown that the adsorption of the C_{60} model molecules on metal surfaces, Au(111) and Ag(111), is quite comparable and only minor changes were observed. Additional nucleation sites allowed formation of molecular islands isolated on terraces. Differences were more pronounced on bulk insulator KBr(001) and NiO. Islands were smaller or only small clusters generated after deposition. Crater formation was furthermore visible on KBr(001).

This pointed to some influence of the ESD method on adsorption and surface morphology which had to be taken into account for the following studies of functionalized molecules and nanoribbons.

After this evaluation, the ESD method and a combination of nc-AFM at RT, STM and AFM at LT and MD simulations were employed to study the thermal response and associated tuning possibilities of alkyl chain functionalized molecules.

In Chapter 4 a mechanism of thermal expansion of two-dimensional supramolecular

Conclusion

networks was found based on mobility of alkyl chains. A giant thermal response of the lattice spacing of a spoked wheel molecule was shown by STM/AFM and nc-AFM at 5 K and 300 K after deposition by ESD. In combination with MD simulations of a triplet assembly of SW at LT the thermal expansion of the assemblies was shown to be solely driven by increasing alkyl chain mobility with temperature. The molecule cores underwent no significant diffusion. The increased movement of the alkyl chains facilitated by their weak interaction with the surface, the soft in-plane bending of the chains and the two-dimensional constraint on the fluctuations imposed by the surface, forces the network expansion to allow the increase in mobility in a step wise expansion. Loss of interaction energy was shown to be compensated by the increasing entropy of the alkyl chain fluctuations.

Applying this mechanism to HBC molecules equipped with three different alkyl chain lengths allowed tuning the thermal response of 2D supramolecular networks as described in Chapter 5. The butyl, octyl and dodecyl chain equipped molecules were deposited on Au(111) and Ag(111) to form equally sized islands of hexagonal molecular networks. STM/AFM and nc-AFM studies at 5 K and 300 K revealed an inversely proportional relation between alkyl chain length and CTE. The shortest chains showed the largest expansion, the longest the lowest. On Au(111) the expansion was generally increased in comparison to the molecules with the same chain length on Ag(111) but a limit reached for the shortest chains with no further increase of CTE being observed. The dependence of chain length and CTE was explained by a closer relative packing allowed at lower temperatures due to the shorter chains along with a decreased freedom of fluctuations leading to a stiffer in-plane bending and, thus, forcing large expansion.

The possibility to access new and interesting solution synthesized GNRs and to study their properties was shown in Chapter 6 by nc-AFM studies after ESD. The properties of two distinct GNRs, one methoxy "cove"-type edged GNR equipped with dodecyl chains and the other a twisted non-planar fjord-edged GNR decorated with *tert*-butyls, were studied at RT. A straight planar rigid structure formed by the ribbon core and two lobes arising from its alkyl chains was observed for OMeGNR, which adsorbed along the hcp domain of the herringbone reconstruction of Au(111). Its structure and adsorption likely contributed to large jump-wise displacements of OMeGNR observed by tip induced manipulations on the surface. In contrast, the FGNR showed a significantly increased flexibility in a wiggly, twisted structure on Au(111). High-resolution imaging revealed its internal structure, which confirmed the non-planar character driven by steric hindrance of the *tert*-butyl groups in the fjords, as shown for a model precursor molecule. With the deposition of FGNRs on KBr(001) and HOPG the access to previously inaccessible surfaces was opened even for fragile GNRs.

Concluding these findings, new functional molecular structures and resulting properties and functionalities were assessed in high-resolution SPM studies after deposition via ESD. This led to the explanation of a new mechanism of thermal response and the possibility of tuning the associated expansion with modification of the alkyl chain length by a combination of nc-AFM, STM/AFM and MD simulations at different temperatures. In addition, the adsorption properties and influence of the edge functionalization of previously inaccessible GNRs were studied on up to now not available surfaces.

In future works, functional moieties included in the cores of the deposited molecules could allow the build-up of precise thermal responsive devices, like thermal sensors, possibly also including light detectable groups, or the targeting of very low response to external stimuli, while still allowing self-assembly by van der Waals interactions due to alkyl chain interdigitation. Furthermore, interesting possible graphene nanoribbon structures, including more complex and three-dimensional structures, along with their self-alignment due to side chains might offer interesting possibilities for semi-conductor or non-linear optical applications and their device integration. This could involve the deposition on semi-conductor surfaces directly, even with their complex structures, and their direct device integration driven by interaction or anchoring of functional groups.

Bibliography

- [1] Barth, J. V., Costantini, G. & Kern, K. Engineering Atomic and Molecular Nanostructures at Surfaces. *Nature* **437**, 671–679 (2005). DOI: 10.1038/nature04166.
- [2] Barth, J. V. Molecular Architectonic on Metal Surfaces. *Annu. Rev. Phys. Chem.* **58**, 375–407 (2007). DOI: 10.1146/annurev.physchem.56.092503.141259.
- [3] Aida, T., Meijer, E. W. & Stupp, S. I. Functional Supramolecular Polymers. *Science* **335**, 813–817 (2012). DOI: 10.1126/science.1205962.
- [4] Kolesnichenko, I. V. & Anslyn, E. V. Practical Applications of Supramolecular Chemistry. *Chem. Soc. Rev.* **46**, 2385–2390 (2017). DOI: 10.1039/C7CS00078B.
- [5] Haines, C. S. *et al.* Artificial Muscles from Fishing Line and Sewing Thread. *Science* **343**, 868–872 (2014). DOI: 10.1126/science.1246906.
- [6] Yokota, T. *et al.* Ultraflexible, large-area, physiological temperature sensors for multi-point measurements. *PNAS* **112**, 14533–14538 (2015). DOI: 10.1073/pnas.1515650112.
- [7] Joh, H., Lee, S.-W., Seong, M., Lee, W. S. & Oh, S. J. Engineering the Charge Transport of Ag Nanocrystals for Highly Accurate, Wearable Temperature Sensors through All-Solution Processes. *Small* **13**, 1700247 (2017). DOI: 10.1002/smll.201700247.
- [8] Anguita, J. V. *et al.* Dimensionally and environmentally ultra-stable polymer composites reinforced with carbon fibres. *Nat. Mater.* **19**, 317–322 (2020). DOI: 10.1038/s41563-019-0565-3.
- [9] Zhu, S. *et al.* Anomalous thermally expanded polymer networks for flexible perceptual devices. *Matter* **4**, 1832–1862 (2021). DOI: 10.1016/j.matt.2021.03.010.
- [10] Yao, X. *et al.* Synthesis of Nonplanar Graphene Nanoribbon with Fjord Edges. *J. Am. Chem. Soc.* **143**, 5654–5658 (2021). DOI: 10.1021/jacs.1c01882.
- [11] Yang, X. *et al.* Two-Dimensional Graphene Nanoribbons. *J. Am. Chem. Soc.* **130**, 4216–4217 (2008). DOI: 10.1021/ja710234t.
- [12] Narita, A. *et al.* Synthesis of structurally well-defined and liquid-phase-processable graphene nanoribbons. *Nat. Chem.* **6**, 126–132 (2014). DOI: 10.1038/nchem.1819.
- [13] Narita, A., Wang, X.-Y., Feng, X. & Müllen, K. New Advances in Nanographene Chemistry. *Chem. Soc. Rev.* **44**, 6616–6643 (2015). DOI: 10.1039/c5cs00183h.

Bibliography

- [14] Fenn, J. B., Mann, M., Meng, C. K., Wong, S. F. & Whitehouse, C. M. Electrospray ionization for mass spectrometry of large biomolecules. *Science* **246**, 64–71 (1989). DOI: 10.1126/science.2675315.
- [15] Fenn, J. B. Electrospray Wings for Molecular Elephants (Nobel Lecture). *Angew. Chem. Int. Ed.* **42**, 3871–3894 (2003). DOI: 10.1002/anie.200300605.
- [16] Rauschenbach, S. *et al.* Electrospray Ion Beam Deposition of Clusters and Biomolecules. *Small* **2**, 540–547 (2006). DOI: 10.1002/smll.200500479.
- [17] Satterley, C. J. *et al.* Electrospray deposition of fullerenes in ultra-high vacuum: in situ scanning tunneling microscopy and photoemission spectroscopy. *Nanotechnology* **18**, 455304 (2007). DOI: 10.1088/0957-4484/18/45/455304.
- [18] Saywell, A. *et al.* Electrospray Deposition of C₆₀ on a Hydrogen-Bonded Supramolecular Network. *J. Phys. Chem. C* **112**, 7706–7709 (2008). DOI: 10.1021/jp7119944.
- [19] Hamann, C. *et al.* Ultrahigh Vacuum Deposition of Organic Molecules by Electrospray Ionization. *Rev. Sci. Instrum.* **82**, 033903 (2011). DOI: 10.1063/1.3553010.
- [20] Hauptmann, N., Hamann, C., Tang, H. & Berndt, R. Switching and charging of a ruthenium dye on Ag(111). *Phys. Chem. Chem. Phys.* **15**, 10326–10330 (2013). DOI: 10.1039/C3CP51023A.
- [21] Hinaut, A., Pawlak, R., Meyer, E. & Glatzel, T. Electrospray Deposition of Organic Molecules on Bulk Insulator Surfaces. *Beilstein J. Nanotechnol.* **6**, 1927–1934 (2015). DOI: 10.3762/bjnano.6.195.
- [22] Scherb, S. *et al.* Giant thermal expansion of a two-dimensional supramolecular network triggered by alkyl chain motion. *Commun. Mater.* **1**, 1–7 (2020). DOI: 10.1038/s43246-020-0009-2.
- [23] O’Shea, J. N. *et al.* Electrospray deposition of carbon nanotubes in vacuum. *Nanotechnology* **18**, 035707 (2007). DOI: 10.1088/0957-4484/18/3/035707.
- [24] Saywell, A. *et al.* Self-Assembled Aggregates Formed by Single-Molecule Magnets on a Gold Surface. *Nat. Commun.* **1**, 75 (2010). DOI: 10.1038/ncomms1075.
- [25] Rienzo, A. *et al.* X-ray absorption and photoemission spectroscopy of zinc protoporphyrin adsorbed on rutile TiO₂(110) prepared by in situ electrospray deposition. *J. Chem. Phys.* **132**, 084703 (2010). DOI: 10.1063/1.3336747.
- [26] Saywell, A. *et al.* Conformation and Packing of Porphyrin Polymer Chains Deposited Using Electrospray on a Gold Surface. *Angew. Chem. Int. Ed.* **49**, 9136–9139 (2010). DOI: 10.1002/anie.201004896.
- [27] Hinaut, A. *et al.* Electrospray Deposition of Structurally Complex Molecules Revealed by Atomic Force Microscopy. *Nanoscale* **10**, 1337–1344 (2018). DOI: 10.1039/C7NR06261C.
- [28] Warr, D. A. *et al.* Sequencing conjugated polymers by eye. *Sci. Adv.* **4**, eaas9543 (2018). DOI: 10.1126/sciadv.aas9543.

- [29] Wu, X. *et al.* Imaging single glycans. *Nature* **582**, 375–378 (2020). DOI: 10.1038/s41586-020-2362-1.
- [30] Temperton, R. H., Skowron, S. T., Gibson, A., Handrup, K. & O’Shea, J. N. Ultrafast charge transfer between fullerenes and a gold surface, as prepared by electrospray deposition. *Chem. Phys. Lett.* **747**, 137309 (2020). DOI: 10.1016/j.cplett.2020.137309.
- [31] Anggara, K. *et al.* Exploring the Molecular Conformation Space by Soft Molecule–Surface Collision. *J. Am. Chem. Soc.* (2020). DOI: 10.1021/jacs.0c09933.
- [32] Paschke, F., Erler, P., Gagnaniello, L., Dreiser, J. & Fonin, M. Electrospray Deposition and Magnetic Properties of Prototypical Molecular Magnets. *Quantum Materials Res.* **1** (2020). DOI: 10.20900/qmr20200002.
- [33] Stoiber, K. A. *Investigating Molecules at Surfaces - from Preparative Mass Spectrometry of Large Biomolecules to Complex Desorption Kinetics*. Doctoral thesis, Technical University of Munich, Munich (2021). URL <https://mediatum.ub.tum.de/doc/1602625/1602625.pdf>.
- [34] Hinaut, A. *et al.* Influence of electrospray deposition on C₆₀ molecular assemblies. *Beilstein J. Nanotechnol.* **12**, 552–558 (2021). DOI: 10.3762/bjnano.12.45.
- [35] Hou, I. C.-Y. *et al.* Synthesis of Giant Dendritic Polyphenylenes with 366 and 546 Carbon Atoms and Their High-vacuum Electrospray Deposition. *Chem.: Asian J.* **17**, e202200220 (2022). DOI: 10.1002/asia.202200220.
- [36] Binnig, G., Rohrer, H., Gerber, C. & Weibel, E. Tunneling through a controllable vacuum gap. *Appl. Phys. Lett.* **40**, 178–180 (1982). DOI: 10.1063/1.92999.
- [37] Binnig, G., Rohrer, H., Gerber, C. & Weibel, E. 7×7 Reconstruction on Si(111) Resolved in Real Space. *Phys. Rev. Lett.* **50**, 120–123 (1983). DOI: 10.1103/PhysRevLett.50.120.
- [38] Schardt, B. C., Yau, S.-L. & Rinaldi, F. Atomic Resolution Imaging of Adsorbates on Metal Surfaces in Air: Iodine Adsorption on Pt(111). *Science* **243**, 1050–1053 (1989). DOI: 10.1126/science.243.4894.1050.
- [39] Piednoir, A. *et al.* Atomic resolution on small three-dimensional metal clusters by STM. *Surf. Sci.* **391**, 19–26 (1997). DOI: 10.1016/S0039-6028(97)00419-6.
- [40] Slough, C. G., McNairy, W. W., Coleman, R. V., Drake, B. & Hansma, P. K. Charge-density waves studied with the use of a scanning tunneling microscope. *Phys. Rev. B* **34**, 994–1005 (1986). DOI: 10.1103/PhysRevB.34.994.
- [41] Hansma, P. K. *et al.* Tapping mode atomic force microscopy in liquids. *Appl. Phys. Lett.* **64**, 1738–1740 (1994). DOI: 10.1063/1.111795.
- [42] Putman, C. A. J., Van der Werf, K. O., De Grooth, B. G., Van Hulst, N. F. & Greve, J. Tapping mode atomic force microscopy in liquid. *Appl. Phys. Lett.* **64**, 2454–2456 (1994). DOI: 10.1063/1.111597.

Bibliography

- [43] Pfeiffer, O., Bennewitz, R., Baratoff, A., Meyer, E. & Grütter, P. Lateral-force measurements in dynamic force microscopy. *Phys. Rev. B* **65**, 161403 (2002). DOI: 10.1103/PhysRevB.65.161403.
- [44] Iwata, K. *et al.* Chemical Structure Imaging of a Single Molecule by Atomic Force Microscopy at Room Temperature. *Nat. Commun.* **6**, 7766 (2015). DOI: 10.1038/ncomms8766.
- [45] Nonnenmacher, M., O’Boyle, M. P. & Wickramasinghe, H. K. Kelvin probe force microscopy. *Appl. Phys. Lett.* **58**, 2921–2923 (1991). DOI: 10.1063/1.105227.
- [46] Giessibl, F. J. High-speed force sensor for force microscopy and profilometry utilizing a quartz tuning fork. *Appl. Phys. Lett.* **73**, 3956–3958 (1998). DOI: 10.1063/1.122948.
- [47] Gross, L., Mohn, F., Moll, N., Liljeroth, P. & Meyer, G. The Chemical Structure of a Molecule Resolved by Atomic Force Microscopy. *Science* **325**, 1110–1114 (2009). DOI: 10.1126/science.1176210.
- [48] Repp, J., Meyer, G., Olsson, F. E. & Persson, M. Controlling the Charge State of Individual Gold Adatoms. *Science* **305**, 493–495 (2004). DOI: 10.1126/science.1099557.
- [49] Repp, J., Meyer, G., Stojković, S. M., Gourdon, A. & Joachim, C. Molecules on Insulating Films: Scanning-Tunneling Microscopy Imaging of Individual Molecular Orbitals. *Phys. Rev. Lett.* **94**, 026803 (2005). DOI: 10.1103/PhysRevLett.94.026803.
- [50] Moreno, C., Stetsovych, O., Shimizu, T. K. & Custance, O. Imaging Three-Dimensional Surface Objects with Submolecular Resolution by Atomic Force Microscopy. *Nano Lett.* **15**, 2257–2262 (2015). DOI: 10.1021/nl504182w.
- [51] Moradi, M. *et al.* Supramolecular Architectures of Molecularly Thin yet Robust Free-Standing Layers. *Sci. Adv.* **5**, 4489 (2019). DOI: 10.1126/sciadv.aav4489.
- [52] Giessibl, F. J. The qPlus sensor, a powerful core for the atomic force microscope. *Rev. Sci. Instrum.* **90**, 011101 (2019). DOI: 10.1063/1.5052264.
- [53] Binnig, G., Quate, C. F. & Gerber, C. Atomic force microscope. *Phys. Rev. Lett.* **56**, 930 (1986). DOI: 10.1103/PhysRevLett.56.930.
- [54] Meyer, E., Gyalog, T., Overney, R. M. & Dransfeld, K. *Nanoscience: Friction and Rheology on the Nanometer Scale* (World Scientific, 1998). DOI: 10.1142/3026.
- [55] Kawai, S. *et al.* Energy dissipation in dynamic force microscopy on KBr(001) correlated with atomic-scale adhesion phenomena. *Phys. Rev. B* **86**, 245419 (2012). DOI: 10.1103/PhysRevB.86.245419.
- [56] Meyer, E., Bennewitz, R. & Hug, H. J. *Scanning Probe Microscopy: The Lab on a Tip*. Graduate Texts in Physics (Springer International Publishing, Cham, 2021). DOI: 10.1007/978-3-030-37089-3.
- [57] Albrecht, T. R., Grütter, P., Horne, D. & Rugar, D. Frequency modulation detection using high-Q cantilevers for enhanced force microscope sensitivity. *J. Appl. Phys.* **69**, 668–673 (1991). DOI: 10.1063/1.347347.

- [58] Giessibl, F. J. Atomic Force Microscopy-(7x7) Surface by Atomic Force Microscopy. *Science* **267**, 68–71 (1995). DOI: 10.5283/epub.33828.
- [59] Kitamura, S.-i. & Iwatsuki, M. Observation of 7×7 Reconstructed Structure on the Silicon (111) Surface using Ultrahigh Vacuum Noncontact Atomic Force Microscopy. *Jpn. J. Appl. Phys.* **34**, L145 (1995). DOI: 10.1143/JJAP.34.L145.
- [60] Ueyama, H., Ohta, M., Sugawara, Y. & Morita, S. M. S. Atomically Resolved InP(110) Surface Observed with Noncontact Ultrahigh Vacuum Atomic Force Microscope. *Jpn. J. Appl. Phys.* **34**, L1086 (1995). DOI: 10.1143/JJAP.34.L1086.
- [61] Meyer, E. Atomic force microscopy. *Prog. Surf. Sci.* **41**, 3–49 (1992). DOI: 10.1016/0079-6816(92)90009-7.
- [62] Giessibl, F. J. Advances in atomic force microscopy. *Rev. Mod. Phys.* **75**, 949 (2003). DOI: 10.1103/RevModPhys.75.949.
- [63] Pérez, R., Payne, M. C., Štich, I. & Terakura, K. Role of Covalent Tip-Surface Interactions in Noncontact Atomic Force Microscopy on Reactive Surfaces. *Phys. Rev. Lett.* **78**, 678–681 (1997). DOI: 10.1103/PhysRevLett.78.678.
- [64] Hudlet, S., Saint Jean, M., Guthmann, C. & Berger, J. Evaluation of the capacitive force between an atomic force microscopy tip and a metallic surface. *Eur. Phys. J. B* **2**, 5–10 (1998). DOI: 10.1007/s100510050219.
- [65] Zerweck, U., Loppacher, C., Otto, T., Grafström, S. & Eng, L. M. Accuracy and resolution limits of Kelvin probe force microscopy. *Phys. Rev. B* **71**, 125424 (2005). DOI: 10.1103/PhysRevB.71.125424.
- [66] Sadewasser, S. & Glatzel, T. (eds.) *Kelvin Probe Force Microscopy*, vol. 48 of *Springer Series in Surface Sciences* (Springer Berlin Heidelberg, Berlin, Heidelberg, 2012). DOI: 10.1007/978-3-642-22566-6.
- [67] Sadewasser, S. & Glatzel, T. (eds.) *Kelvin Probe Force Microscopy: From Single Charge Detection to Device Characterization*, vol. 65 of *Springer Series in Surface Sciences* (Springer International Publishing, Cham, 2018). DOI: 10.1007/978-3-319-75687-5.
- [68] Sadewasser, S. & Lux-Steiner, M. C. Correct Height Measurement in Noncontact Atomic Force Microscopy. *Phys. Rev. Lett.* **91**, 266101 (2003). DOI: 10.1103/PhysRevLett.91.266101.
- [69] Barth, C. & Henry, C. R. Kelvin probe force microscopy on surfaces of UHV cleaved ionic crystals. *Nanotechnology* **17**, S155 (2006). DOI: 10.1088/0957-4484/17/7/S09.
- [70] Filleter, T., Emtsev, K. V., Seyller, T. & Bennewitz, R. Local work function measurements of epitaxial graphene. *Appl. Phys. Lett.* **93**, 133117 (2008). DOI: 10.1063/1.2993341.
- [71] Hamaker, H. C. The London—van der Waals attraction between spherical particles. *Physica* **4**, 1058–1072 (1937). DOI: 10.1016/S0031-8914(37)80203-7.
- [72] Guggisberg, M. *et al.* Separation of interactions by noncontact force microscopy. *Phys. Rev. B* **61**, 11151–11155 (2000). DOI: 10.1103/PhysRevB.61.11151.

Bibliography

- [73] Israelachvili, J. N. 6 - Van der Waals Forces. In Israelachvili, J. N. (ed.) *Intermolecular and Surface Forces (Third Edition)*, 107–132 (Academic Press, San Diego, 2011). DOI: 10.1016/B978-0-12-375182-9.10006-5.
- [74] Livshits, A. I., Shluger, A. L., Rohl, A. L. & Foster, A. S. Model of noncontact scanning force microscopy on ionic surfaces. *Phys. Rev. B* **59**, 2436–2448 (1999). DOI: 10.1103/PhysRevB.59.2436.
- [75] Sugimoto, Y. *et al.* Chemical identification of individual surface atoms by atomic force microscopy. *Nature* **446**, 64–67 (2007). DOI: 10.1038/nature05530.
- [76] Giessibl, F. J. Forces and frequency shifts in atomic-resolution dynamic-force microscopy. *Phys. Rev. B* **56**, 16010 (1997). DOI: 10.1103/PhysRevB.56.16010.
- [77] Israelachvili, J. N. 7 - Repulsive Steric Forces, Total Intermolecular Pair Potentials, and Liquid Structure. In Israelachvili, J. N. (ed.) *Intermolecular and Surface Forces (Third Edition)*, 133–149 (Academic Press, San Diego, 2011). DOI: 10.1016/B978-0-12-375182-9.10007-7.
- [78] Huang, L. & Su, C. A torsional resonance mode AFM for in-plane tip surface interactions. *Ultramicroscopy* **100**, 277–285 (2004). DOI: 10.1016/j.ultramic.2003.11.010.
- [79] Kawai, S., Kitamura, S.-i., Kobayashi, D., Meguro, S. & Kawakatsu, H. An ultrasmall amplitude operation of dynamic force microscopy with second flexural mode. *Appl. Phys. Lett.* **86**, 193107 (2005). DOI: 10.1063/1.1923200.
- [80] Martinez, N. F., Patil, S., Lozano, J. R. & Garcia, R. Enhanced compositional sensitivity in atomic force microscopy by the excitation of the first two flexural modes. *Appl. Phys. Lett.* **89**, 153115 (2006). DOI: 10.1063/1.2360894.
- [81] Kawai, S., Kitamura, S.-i., Kobayashi, D. & Kawakatsu, H. Dynamic lateral force microscopy with true atomic resolution. *Appl. Phys. Lett.* **87**, 173105 (2005). DOI: 10.1063/1.2112203.
- [82] Kawai, S. *et al.* Systematic Achievement of Improved Atomic-Scale Contrast via Bimodal Dynamic Force Microscopy. *Phys. Rev. Lett.* **103**, 220801 (2009). DOI: 10.1103/PhysRevLett.103.220801.
- [83] Kawai, S. *et al.* Ultrasensitive detection of lateral atomic-scale interactions on graphite (0001) via bimodal dynamic force measurements. *Phys. Rev. B* **81**, 085420 (2010). DOI: 10.1103/PhysRevB.81.085420.
- [84] Cai, W. & Yao, N. Dynamic nano-triboelectrification using torsional resonance mode atomic force microscopy. *Sci. Rep.* **6**, srep27874 (2016). DOI: 10.1038/srep27874.
- [85] Kawai, S. *et al.* Measuring Electric Field Induced Subpicometer Displacement of Step Edge Ions. *Phys. Rev. Lett.* **109**, 146101 (2012). DOI: 10.1103/PhysRevLett.109.146101.
- [86] Freund, S. *et al.* Transoid-to-Cisoid Conformation Changes of Single Molecules on Surfaces Triggered by Metal Coordination. *ACS Omega* **3**, 12851–12856 (2018). DOI: 10.1021/acsomega.8b01792.

- [87] Freund, S. *et al.* Anchoring of a dye precursor on NiO(001) studied by non-contact atomic force microscopy. *Beilstein J. Nanotechnol.* **9**, 242–249 (2018). DOI: 10.3762/bjnano.9.26.
- [88] Müller, V. *et al.* A Two-Dimensional Polymer Synthesized at the Air/Water Interface. *Angew. Chem. Int. Ed.* **57**, 10584–10588 (2018). DOI: 10.1002/anie.201804937.
- [89] Ishida, N. *et al.* Direct visualization of the N impurity state in dilute GaNAs using scanning tunneling microscopy. *Nanoscale* **7**, 16773–16780 (2015). DOI: 10.1039/C5NR04193G.
- [90] Weaver, J. M. R. High resolution atomic force microscopy potentiometry. *J. Vac. Sci. Technol. B* **9**, 1559 (1991). DOI: 10.1116/1.585423.
- [91] Kikukawa, A., Hosaka, S. & Imura, R. Vacuum compatible high-sensitive Kelvin probe force microscopy. *Rev. Sci. Instrum.* **67**, 1463–1467 (1996). DOI: 10.1063/1.1146874.
- [92] Kitamura, S. & Iwatsuki, M. High-resolution imaging of contact potential difference with ultrahigh vacuum noncontact atomic force microscope. *Appl. Phys. Lett.* **72**, 3154–3156 (1998). DOI: 10.1063/1.121577.
- [93] Glatzel, T., Sadewasser, S. & Lux-Steiner, M. Amplitude or frequency modulation-detection in Kelvin probe force microscopy. *Appl. Surf. Sci.* **210**, 84–89 (2003). DOI: 10.1016/S0169-4332(02)01484-8.
- [94] Loppacher, C. *et al.* FM demodulated Kelvin probe force microscopy for surface photovoltage tracking. *Nanotechnology* **16**, S1–S6 (2005). DOI: 10.1088/0957-4484/16/3/001.
- [95] Giessibl, F. J. Atomic resolution on Si (111)-(7x7) by noncontact atomic force microscopy with a force sensor based on a quartz tuning fork. *Appl. Phys. Lett.* **76**, 1470–1472 (2000). DOI: 10.1063/1.126067.
- [96] Gross, L. *et al.* Atomic Force Microscopy for Molecular Structure Elucidation. *Angew. Chem. Int. Ed.* **57**, 3888–3908 (2018). DOI: 10.1002/anie.201703509.
- [97] Bartels, L., Meyer, G. & Rieder, K.-H. Controlled vertical manipulation of single CO molecules with the scanning tunneling microscope: A route to chemical contrast. *Appl. Phys. Lett.* **71**, 213–215 (1997). DOI: 10.1063/1.119503.
- [98] Gross, L. *et al.* Atomic Resolution on Molecules with Functionalized Tips. In Morita, S., Giessibl, F. J., Meyer, E. & Wiesendanger, R. (eds.) *Noncontact Atomic Force Microscopy: Volume 3*, NanoScience and Technology, 223–246 (Springer International Publishing, Cham, 2015). DOI: 10.1007/978-3-319-15588-3_12.
- [99] Fessler, G. *Structural Friction Anisotropy on the Nanometer Scale*. Thesis, University of Basel (2013). URL http://edoc.unibas.ch/diss/DissB_10652. DOI: 10.5451/unibas-006214593.
- [100] Jöhr, R. *Interaction of Single Metallo-Porphyrins with Titania Surfaces : Advanced Atomic Force Microscopy Studies*. Thesis, University of Basel (2016). URL http://edoc.unibas.ch/diss/DissB_12122. DOI: 10.5451/unibas-006699943.

Bibliography

- [101] Biegelsen, D. K., Ponce, F. A., Tramontana, J. C. & Koch, S. M. Ion milled tips for scanning tunneling microscopy. *Appl. Phys. Lett.* **50**, 696–698 (1987). DOI: 10.1063/1.98070.
- [102] Drechsel, C. *Atomic and Molecular Adsorption on Superconducting Pb as Basis for the Realization of Qubits*. Doctoral thesis, University of Basel, Basel (2021).
- [103] Hasegawa, Y. & Avouris, P. Manipulation of the Reconstruction of the Au(111) Surface with the STM. *Science* **258**, 1763–1765 (1992). DOI: 10.1126/science.258.5089.1763.
- [104] Narasimhan, S. & Vanderbilt, D. Elastic stress domains and the herringbone reconstruction on Au(111). *Phys. Rev. Lett.* **69**, 1564–1567 (1992). DOI: 10.1103/PhysRevLett.69.1564.
- [105] Koma, A. Molecular beam epitaxial growth of organic thin films. *Prog. Cryst. Growth Charact. Mater.* **30**, 129–152 (1995). DOI: 10.1016/0960-8974(95)00009-V.
- [106] Torsney, S. P. *Toward Molecular Quantum-Dot Cellular Automata: A Scanning Tunneling Microscopy Investigation*. Doctoral thesis, Trinity College Dublin, Dublin (2018). URL <http://www.tara.tcd.ie/handle/2262/84973>.
- [107] Cai, J. *et al.* Atomically precise bottom-up fabrication of graphene nanoribbons. *Nature* **466**, 470–473 (2010). DOI: 10.1038/nature09211.
- [108] Houtsma, R. S. K., de la Rie, J. & Stöhr, M. Atomically precise graphene nanoribbons: Interplay of structural and electronic properties. *Chem. Soc. Rev.* (2021). DOI: 10.1039/D0CS01541E.
- [109] Kolmer, M. *et al.* Rational synthesis of atomically precise graphene nanoribbons directly on metal oxide surfaces. *Science* **369**, 571–575 (2020). DOI: 10.1126/science.abb8880.
- [110] Fantuzzi, P. *et al.* Fabrication of three terminal devices by ElectroSpray deposition of graphene nanoribbons. *Carbon* **104**, 112–118 (2016). DOI: 10.1016/j.carbon.2016.03.052.
- [111] Fantuzzi, P. *Fabrication and Characterization of Graphene-Based Nanodevices through Electron Beam Lithography and Electrospray*. Doctoral thesis, Università Modena und Reggio Emilia, Modena (2018). URL <https://morethesis.unimore.it/theses/available/etd-11212017-172152/>.
- [112] Manandhar, K. *et al.* A scanning tunneling microscopy study on the effect of post-deposition annealing of copper phthalocyanine thin films. *Surf. Sci.* **601**, 3623–3631 (2007). DOI: 10.1016/j.susc.2007.07.007.
- [113] Rapenne, G. *et al.* Launching and landing single molecular wheelbarrows on a Cu(100) surface. *Chem. Phys. Lett.* **431**, 219–222 (2006). DOI: 10.1016/j.cplett.2006.09.080.
- [114] Beuhler, R. J., Flanigan, E., Greene, L. J. & Friedman, L. Proton transfer mass spectrometry of peptides. Rapid heating technique for underivatized peptides containing arginine. *J. Am. Chem. Soc.* **96**, 3990–3999 (1974). DOI: 10.1021/ja00819a043.

- [115] Räder, H. J. *et al.* Processing of giant graphene molecules by soft-landing mass spectrometry. *Nat. Mater.* **5**, 276–280 (2006). DOI: 10.1038/nmat1597.
- [116] Albrecht, P. M. & Lyding, J. W. Ultrahigh-vacuum scanning tunneling microscopy and spectroscopy of single-walled carbon nanotubes on hydrogen-passivated Si(100) surfaces. *Appl. Phys. Lett.* **83**, 5029–5031 (2003). DOI: 10.1063/1.1633014.
- [117] Clair, S., Rabot, C., Kim, Y. & Kawai, M. Adsorption mechanism of aligned single wall carbon nanotubes at well defined metal surfaces. *J. Vac. Sci. Technol. B* **25**, 1143 (2007). DOI: 10.1116/1.2743652.
- [118] Chen, S. *et al.* On-Surface Synthesis of 2D Porphyrin-Based Covalent Organic Frameworks Using Terminal Alkynes. *Chem. Mater.* **33**, 8677–8684 (2021). DOI: 10.1021/acs.chemmater.1c02564.
- [119] McCurdy, R. D. *et al.* Synergetic Bottom-Up Synthesis of Graphene Nanoribbons by Matrix-Assisted Direct Transfer. *J. Am. Chem. Soc.* **143**, 4174–4178 (2021). DOI: 10.1021/jacs.1c01355.
- [120] Tanaka, H. & Kawai, T. Scanning tunneling microscopy imaging and manipulation of DNA oligomer adsorbed on Cu(111) surfaces by a pulse injection method. *J. Vac. Sci. Technol. B* **15**, 602–604 (1997). DOI: 10.1116/1.589299.
- [121] Kanno, T., Tanaka, H., Nakamura, T., Tabata, H. & Kawai, T. Real Space Observation of Double-Helix DNA Structure Using a Low Temperature Scanning Tunneling Microscopy. *Jpn. J. Appl. Phys.* **38**, L606–L607 (1999). DOI: 10.1143/JJAP.38.L606.
- [122] Terada, Y., Choi, B.-K., Heike, S., Fujimori, M. & Hashizume, T. Injection of molecules onto hydrogen-terminated Si(100) surfaces via a pulse valve. *J. Appl. Phys.* **93**, 10014–10017 (2003). DOI: 10.1063/1.1572972.
- [123] Terada, Y., Choi, B.-K., Heike, S., Fujimori, M. & Hashizume, T. Placing Conducting Polymers onto a H-Terminated Si(100) Surface via a Pulse Valve. *Nano Lett.* **3**, 527–531 (2003). DOI: 10.1021/nl0259737.
- [124] Bernard, R. *et al.* Ultrahigh vacuum deposition of CdSe nanocrystals on surfaces by pulse injection. *J. Phys.: Condens. Matter* **16**, 7565–7579 (2004). DOI: 10.1088/0953-8984/16/43/001.
- [125] Rinke, G. *et al.* Soft-landing electrospray ion beam deposition of sensitive oligoynes on surfaces in vacuum. *Int. J. Mass Spectrom.* **377**, 228–234 (2015). DOI: 10.1016/j.ijms.2014.06.026.
- [126] Siuzdak, G. *et al.* Mass spectrometry and viral analysis. *Chem. Biol.* **3**, 45–48 (1996). DOI: 10.1016/S1074-5521(96)90083-6.
- [127] Swarbrick, J. C., Taylor, J. B. & O’Shea, J. N. Electrospray deposition in vacuum. *Appl. Surf. Sci.* **252**, 5622–5626 (2006). DOI: 10.1016/j.apsusc.2005.12.025.
- [128] Jaworek, A. & Krupa, A. CLASSIFICATION OF THE MODES OF EHD SPRAYING. *J. Aerosol Sci.* **30**, 873–893 (1999). DOI: 10.1016/S0021-8502(98)00787-3.

Bibliography

- [129] Taylor, G. I. Disintegration of water drops in an electric field. *Proc. R. Soc. Lond. A* **280**, 383–397 (1964). DOI: 10.1098/rspa.1964.0151.
- [130] Zeleny, J. The Electrical Discharge from Liquid Points, and a Hydrostatic Method of Measuring the Electric Intensity at Their Surfaces. *Phys. Rev.* **3**, 69–91 (1914). DOI: 10.1103/PhysRev.3.69.
- [131] Zeleny, J. Instability of Electrified Liquid Surfaces. *Phys. Rev.* **10**, 1–6 (1917). DOI: 10.1103/PhysRev.10.1.
- [132] Fernández de la Mora, J. The Fluid Dynamics of Taylor Cones. *Annu. Rev. Fluid Mech.* **39**, 217–243 (2007). DOI: 10.1146/annurev.fluid.39.050905.110159.
- [133] Cloupeau, M. & Prunet-Foch, B. Electrostatic spraying of liquids: Main functioning modes. *J. Electrostat.* **25**, 165–184 (1990). DOI: 10.1016/0304-3886(90)90025-Q.
- [134] Rayleigh, L. XX. On the equilibrium of liquid conducting masses charged with electricity. *London, Edinburgh Dublin Philos. Mag. J. Sci.* **14**, 184–186 (1882). DOI: 10.1080/14786448208628425.
- [135] Oberacker, V. E., Pinkston, W. T. & Kruse, H. G. W. Coulomb fission. *Rep. Prog. Phys.* **48**, 327–374 (1985). DOI: 10.1088/0034-4885/48/3/002.
- [136] Duft, D., Achtzehn, T., Müller, R., Huber, B. A. & Leisner, T. Rayleigh jets from levitated microdroplets. *Nature* **421**, 128–128 (2003). DOI: 10.1038/421128a.
- [137] Gomez, A. & Tang, K. Charge and fission of droplets in electrostatic sprays. *Phys. Fluids* **6**, 404–414 (1994). DOI: 10.1063/1.868037.
- [138] Konermann, L., Ahadi, E., Rodriguez, A. D. & Vahidi, S. Unraveling the Mechanism of Electrospray Ionization. *Anal. Chem.* **85**, 2–9 (2013). DOI: 10.1021/ac302789c.
- [139] Nguyen, S. & Fenn, J. B. Gas-phase ions of solute species from charged droplets of solutions. *PNAS* **104**, 1111–1117 (2007). DOI: 10.1073/pnas.0609969104.
- [140] Iribarne, J. V. & Thomson, B. A. On the evaporation of small ions from charged droplets. *J. Chem. Phys.* **64**, 2287–2294 (1976). DOI: 10.1063/1.432536.
- [141] Thomson, B. A. & Iribarne, J. V. Field induced ion evaporation from liquid surfaces at atmospheric pressure. *J. Chem. Phys.* **71**, 4451–4463 (1979). DOI: 10.1063/1.438198.
- [142] Ahadi, E. & Konermann, L. Ejection of Solvated Ions from Electrosprayed Methanol/Water Nanodroplets Studied by Molecular Dynamics Simulations. *J. Am. Chem. Soc.* **133**, 9354–9363 (2011). DOI: 10.1021/ja111492s.
- [143] Ahadi, E. & Konermann, L. Modeling the Behavior of Coarse-Grained Polymer Chains in Charged Water Droplets: Implications for the Mechanism of Electrospray Ionization. *J. Phys. Chem. B* **116**, 104–112 (2012). DOI: 10.1021/jp209344z.
- [144] Konermann, L., Rodriguez, A. D. & Liu, J. On the Formation of Highly Charged Gaseous Ions from Unfolded Proteins by Electrospray Ionization. *Anal. Chem.* **84**, 6798–6804 (2012). DOI: 10.1021/ac301298g.

- [145] Dole, M. *et al.* Molecular Beams of Macroions. *J. Chem. Phys.* **49**, 2240–2249 (1968). DOI: 10.1063/1.1670391.
- [146] Rodriguez-Cruz, S. E., Klassen, J. S. & Williams, E. R. Hydration of gas-phase ions formed by electrospray ionization. *J. Am. Soc. Mass Spectrom.* **10**, 958–968 (1999). DOI: 10.1016/S1044-0305(99)00068-9.
- [147] Ikonomou, M. G., Blades, A. T. & Kebarle, P. Investigations of the electrospray interface for liquid chromatography/mass spectrometry. *Anal. Chem.* **62**, 957–967 (1990). DOI: 10.1021/ac00208a012.
- [148] Perdigão, L. M. A. *et al.* Bimolecular Networks and Supramolecular Traps on Au(111). *J. Phys. Chem. B* **110**, 12539–12542 (2006). DOI: 10.1021/jp060062x.
- [149] Staniec, P. A., Perdigão, L. M. A., Saywell, A., Champness, N. R. & Beton, P. H. Hierarchical Organisation on a Two-Dimensional Supramolecular Network. *ChemPhysChem* **8**, 2177–2181 (2007). DOI: 10.1002/cphc.200700513.
- [150] Pawlak, R. *et al.* Conformations and Cryo-Force Spectroscopy of Spray-Deposited Single-Strand DNA on Gold. *Nat. Commun.* **10**, 685 (2019). DOI: 10.1038/s41467-019-08531-4.
- [151] Kolodziej, J. J. *et al.* Frenkel defect interactions at surfaces of irradiated alkali halides studied by non-contact atomic-force microscopy. *Surf. Sci.* **482–485**, 903–909 (2001). DOI: 10.1016/S0039-6028(01)00936-0.
- [152] Motai, K. *et al.* C₆₀ Grown on the Cu(111)1×1 Surface. *Jpn. J. Appl. Phys.* **32**, L450 (1993). DOI: 10.1143/JJAP.32.L450.
- [153] Lu, X., Grobis, M., Khoo, K. H., Louie, S. G. & Crommie, M. F. Charge transfer and screening in individual C₆₀ molecules on metal substrates: A scanning tunneling spectroscopy and theoretical study. *Phys. Rev. B* **70**, 115418 (2004). DOI: 10.1103/PhysRevB.70.115418.
- [154] Mativetsky, J. M., Burke, S. A., Hoffmann, R., Sun, Y. & Grutter, P. Molecular resolution imaging of C₆₀ on Au(111) by non-contact atomic force microscopy. *Nanotechnology* **15**, S40–S43 (2004). DOI: 10.1088/0957-4484/15/2/009.
- [155] Gardener, J. A., Briggs, G. A. D. & Castell, M. R. Scanning tunneling microscopy studies of C₆₀ monolayers on Au(111). *Phys. Rev. B* **80**, 235434 (2009). DOI: 10.1103/PhysRevB.80.235434.
- [156] Pawlak, R., Kawai, S., Fremy, S., Glatzel, T. & Meyer, E. Atomic-Scale Mechanical Properties of Orientated C₆₀ Molecules Revealed by Noncontact Atomic Force Microscopy. *ACS Nano* **5**, 6349–6354 (2011). DOI: 10.1021/nn201462g.
- [157] Pawlak, R., Kawai, S., Fremy, S., Glatzel, T. & Meyer, E. High-resolution imaging of C₆₀ molecules using tuning-fork-based non-contact atomic force microscopy. *J. Phys.: Condens. Matter* **24**, 084005 (2012). DOI: 10.1088/0953-8984/24/8/084005.
- [158] Shin, H. *et al.* Structure and dynamics of C₆₀ molecules on Au (111). *Phys. Rev. B* **89**, 245428 (2014). DOI: 10.1103/PhysRevB.89.245428.

Bibliography

- [159] Loske, F. & Kühnle, A. Manipulation of C₆₀ islands on the rutile TiO₂(110) surface using noncontact atomic force microscopy. *Appl. Phys. Lett.* **95**, 043110 (2009). DOI: 10.1063/1.3184784.
- [160] Loske, F. *et al.* Growth of ordered C₆₀ islands on TiO₂(110). *Nanotechnology* **20**, 065606 (2009). DOI: 10.1088/0957-4484/20/6/065606.
- [161] Burke, S. A., Mativetsky, J. M., Hoffmann, R. & Grütter, P. Nucleation and Submonolayer Growth of C₆₀ on KBr. *Phys. Rev. Lett.* **94**, 096102 (2005). DOI: 10.1103/PhysRevLett.94.096102.
- [162] Burke, S. A., Mativetsky, J. M., Fostner, S. & Grütter, P. C₆₀ on alkali halides: Epitaxy and morphology studied by noncontact AFM. *Phys. Rev. B* **76**, 035419 (2007). DOI: 10.1103/PhysRevB.76.035419.
- [163] Rahe, P., Lindner, R., Kittelmann, M., Nimmrich, M. & Kühnle, A. From dewetting to wetting molecular layers: C₆₀ on CaCO₃(104) as a case study. *Phys. Chem. Chem. Phys.* **14**, 6544–6548 (2012). DOI: 10.1039/C2CP40172J.
- [164] Hoff, B., Henry, C. R. & Barth, C. Charging C₆₀ islands with the AFM tip. *Nanoscale* **8**, 411–419 (2015). DOI: 10.1039/C5NR04541J.
- [165] Freund, S. *et al.* Morphology Change of C₆₀ Islands on Organic Crystals Observed by Atomic Force Microscopy. *ACS Nano* **10**, 5782–5788 (2016). DOI: 10.1021/acsnano.5b07971.
- [166] Bammerlin, M. *et al.* Dynamic SFM with true atomic resolution on alkali halide surfaces. *Appl. Phys. A* **66**, S293–S294 (1998). DOI: 10.1007/s003390051148.
- [167] Such, B. *et al.* Functionalized Truxenes: Adsorption and Diffusion of Single Molecules on the KBr(001) Surface. *ACS Nano* **4**, 3429–3439 (2010). DOI: 10.1021/nn100424g.
- [168] Hinaut, A. *et al.* NC-AFM Study of the Adsorption of Hexamethoxytriphenylene on KBr(001). *J. Phys. Chem. C* **115**, 13338–13342 (2011). DOI: 10.1021/jp202873f.
- [169] Freund, S. *Anchoring of Dye Molecules on a Nickel Oxide Surface : An Atomic Force Microscopy Study*. Thesis, University of Basel (2018). URL http://edoc.unibas.ch/diss/Diss_B_13090. DOI: 10.5451/unibas-007094484.
- [170] Schull, G., Néel, N., Becker, M., Kröger, J. & Berndt, R. Spatially resolved conductance of oriented C₆₀. *New J. Phys.* **10**, 065012 (2008). DOI: 10.1088/1367-2630/10/6/065012.
- [171] Meyer, J. A., Baikie, I. D., Kopatzki, E. & Behm, R. J. Preferential island nucleation at the elbows of the Au(111) herringbone reconstruction through place exchange. *Surf. Sci.* **365**, L647–L651 (1996). DOI: 10.1016/0039-6028(96)00852-7.
- [172] Pawlak, R. *et al.* Design and Characterization of an Electrically Powered Single Molecule on Gold. *ACS Nano* **11**, 9930–9940 (2017). DOI: 10.1021/acsnano.7b03955.
- [173] Burke, S. A. *Building Foundations for Molecular Electronics: Growth of Organic Molecules on Alkali Halides as Prototypical Insulating Substrates*. Doctoral thesis, McGill University, Montreal (2008). URL <https://escholarship.mcgill.ca/concern/theses/qz20sv59p>.

- [174] Barth, C., Claeys, C. & Henry, C. R. Surface preparation of hard ionic crystals by ultra-high vacuum cleavage. *Rev. Sci. Instrum.* **76**, 083907 (2005). DOI: 10.1063/1.2001669.
- [175] Szymonski, M. *et al.* Nano-scale modification of ionic surfaces induced by electronic transitions. *Prog. Surf. Sci.* **67**, 123–138 (2001). DOI: 10.1016/S0079-6816(01)00019-3.
- [176] Szymonski, M., Droba, A., Goryl, M., Kolodziej, J. J. & Krok, F. Alkali halide decomposition and desorption by photons—the role of excited point defects and surface topographies. *J. Phys.: Condens. Matter* **18**, S1547–S1562 (2006). DOI: 10.1088/0953-8984/18/30/S09.
- [177] Hinaut, A. *et al.* Nanostructuring of an alkali halide surface by low temperature plasma exposure. *Phys. Chem. Chem. Phys.* **19**, 16251–16256 (2017). DOI: 10.1039/C7CP02592K.
- [178] Maier, S. *et al.* Asymmetry in the reciprocal epitaxy of NaCl and KBr. *Phys. Rev. B* **75**, 195408 (2007). DOI: 10.1103/PhysRevB.75.195408.
- [179] Scherb, S. *UHV AFM and STM Studies of Electrospray Deposited Graphene-like Molecules*. Master’s thesis, University of Basel, Basel (2018).
- [180] Nony, L. *et al.* Observation of Individual Molecules Trapped on a Nanostructured Insulator. *Nano Lett.* **4**, 2185–2189 (2004). DOI: 10.1021/nl048693v.
- [181] Mativetsky, J. M., Miyahara, Y., Fostner, S., Burke, S. A. & Grutter, P. Use of an electron-beam evaporator for the creation of nanostructured pits in an insulating surface. *Appl. Phys. Lett.* **88**, 233121 (2006). DOI: 10.1063/1.2210288.
- [182] Mativetsky, J. M., Burke, S. A., Fostner, S. & Grutter, P. Nanoscale Pits as Templates for Building a Molecular Device. *Small* **3**, 818–821 (2007). DOI: 10.1002/smll.200600699.
- [183] Freund, S. *et al.* Comparing a porphyrin- and a coumarin-based dye adsorbed on NiO(001). *Beilstein J. Nanotechnol.* **10**, 874–881 (2019). DOI: 10.3762/bjnano.10.88.
- [184] Liu, Z. *et al.* Negative Thermal Expansion in Molecular Materials. *Chem. Commun.* **54**, 5164–5176 (2018). DOI: 10.1039/C8CC01153B.
- [185] Lei, S. *et al.* One building block, two different supramolecular surface-confined patterns: Concentration in control at the solid–liquid interface. *Angew. Chem. Int. Ed.* **47**, 2964–2968 (2008). DOI: 10.1002/anie.200705322.
- [186] Gutzler, R. *et al.* Reversible Phase Transitions in Self-Assembled Monolayers at the Liquid-Solid Interface: Temperature-Controlled Opening and Closing of Nanopores. *J. Am. Chem. Soc.* **132**, 5084–5090 (2010). DOI: 10.1021/ja908919r.
- [187] Shen, Y.-T. *et al.* Switchable Ternary Nanoporous Supramolecular Network on Photo-Regulation. *Nano Lett.* **11**, 3245–3250 (2011). DOI: 10.1021/nl201504x.
- [188] González-Benito, J., Castillo, E. & Cruz-Caldito, J. F. Determination of the linear coefficient of thermal expansion in polymer films at the nanoscale: Influence of the composition of EVA copolymers and the molecular weight of PMMA. *Phys. Chem. Chem. Phys.* **17**, 18495–18500 (2015). DOI: 10.1039/C5CP02384J.

Bibliography

- [189] Bonacchi, S. *et al.* Surface-Induced Selection During In Situ Photoswitching at the Solid/Liquid Interface. *Angew. Chem. Int. Ed.* **54**, 4865–4869 (2015). DOI: 10.1002/anie.201412215.
- [190] Mali, K. S., Pearce, N., De Feyter, S. & Champness, N. R. Frontiers of Supramolecular Chemistry at Solid Surfaces. *Chem. Soc. Rev.* **46**, 2520–2542 (2017). DOI: 10.1039/C7CS00113D.
- [191] Chaikasetsin, S. *et al.* Thermal expansion characterization of thin films using harmonic Joule heating combined with atomic force microscopy. *Appl. Phys. Lett.* **118**, 194101 (2021). DOI: 10.1063/5.0049160.
- [192] Velpula, G. *et al.* “Concentration-in-Control” self-assembly concept at the liquid–solid interface challenged. *Chem. Sci.* (2021). DOI: 10.1039/D1SC02950A.
- [193] Park, S.-A. *et al.* Sustainable and recyclable super engineering thermoplastic from biorenewable monomer. *Nat. Commun.* **10** (2019). DOI: 10.1038/s41467-019-10582-6.
- [194] Meissner, M. *et al.* Flexible 2D Crystals of Polycyclic Aromatics Stabilized by Static Distortion Waves. *ACS Nano* **10**, 6474–6483 (2016). DOI: 10.1021/acsnano.6b00935.
- [195] Mary, T. A., Evans, J. S. O., Vogt, T. & Sleight, A. W. Negative Thermal Expansion from 0.3 to 1050 Kelvin in ZrW_2O_8 . *Science* **272**, 90–92 (1996). DOI: 10.1126/science.272.5258.90.
- [196] Miller, W., Smith, C. W., Mackenzie, D. S. & Evans, K. E. Negative Thermal Expansion: A Review. *J. Mater. Sci.* **44**, 5441–5451 (2009). DOI: 10.1007/s10853-009-3692-4.
- [197] Wu, C. & Zhou, S. Laser Light Scattering Study of the Phase Transition of Poly(N-isopropylacrylamide) in Water. 1. Single Chain. *Macromolecules* **28**, 8381–8387 (1995). DOI: 10.1021/ma00128a056.
- [198] Wu, C. & Wang, X. Globule-to-Coil Transition of a Single Homopolymer Chain in Solution. *Phys. Rev. Lett.* **80**, 4092–4094 (1998). DOI: 10.1103/PhysRevLett.80.4092.
- [199] Shen, X., Viney, C., Johnson, E. R., Wang, C. & Lu, J. Q. Large Negative Thermal Expansion of a Polymer Driven by a Submolecular Conformational Change. *Nat. Chem.* **5**, 1035 (2013). DOI: 10.1038/nchem.1780.
- [200] Shen, X. *et al.* Adjusting Local Molecular Environment for Giant Ambient Thermal Contraction. *Macromol. Rapid Commun.* **37**, 1904–1911 (2016). DOI: 10.1002/marc.201600045.
- [201] Goodwin, A. L. *et al.* Colossal Positive and Negative Thermal Expansion in the Framework Material $\text{Ag}_3[\text{Co}(\text{CN})_6]$. *Science* (2008). DOI: 10.1126/science.1151442.
- [202] Fortes, A. D., Suard, E. & Knight, K. S. Negative linear compressibility and massive anisotropic thermal expansion in methanol monohydrate. *Science* **331**, 742–746 (2011). DOI: 10.1126/science.1198640.
- [203] DeVries, L. D., Barron, P. M., Hurley, E. P., Hu, C. & Choe, W. “Nanoscale Lattice Fence” in a Metal–Organic Framework: Interplay between Hinged Topology and Highly Anisotropic Thermal Response. *J. Am. Chem. Soc.* **133**, 14848–14851 (2011). DOI: 10.1021/ja2032822.

- [204] Wei, Y.-S. *et al.* Turning on the flexibility of isoreticular porous coordination frameworks for drastically tunable framework breathing and thermal expansion. *Chem. Sci.* **4**, 1539–1546 (2013). DOI: 10.1039/C3SC22222E.
- [205] Huang, Y.-G. *et al.* Superior thermoelasticity and shape-memory nanopores in a porous supramolecular organic framework. *Nat. Commun.* **7**, 11564 (2016). DOI: 10.1038/ncomms11564.
- [206] Liu, Z., Liu, C., Li, Q., Chen, J. & Xing, X. Spring-like motion caused large anisotropic thermal expansion in nonporous $M(\text{eim})_2$ ($M = \text{Zn}, \text{Cd}$). *Phys. Chem. Chem. Phys.* **19**, 24436–24439 (2017). DOI: 10.1039/C7CP03937A.
- [207] Zhang, J.-P., Zhou, H.-L., Zhou, D.-D., Liao, P.-Q. & Chen, X.-M. Controlling flexibility of metal–organic frameworks. *Natl. Sci. Rev.* **5**, 907–919 (2018). DOI: 10.1093/nsr/nwx127.
- [208] Goodwin, A. L., Chapman, K. W. & Kepert, C. J. Guest-Dependent Negative Thermal Expansion in Nanoporous Prussian Blue Analogues $M^{\text{II}}\text{Pt}^{\text{IV}}(\text{CN})_6x\{\text{H}_2\text{O}\}$ ($0 \leq x \leq 2$; $M = \text{Zn}, \text{Cd}$). *J. Am. Chem. Soc.* **127**, 17980–17981 (2005). DOI: 10.1021/ja056460f.
- [209] Phillips, A. E., Goodwin, A. L., Halder, G. J., Southon, P. D. & Kepert, C. J. Nanoporosity and Exceptional Negative Thermal Expansion in Single-Network Cadmium Cyanide. *Angew. Chem. Int. Ed.* **47**, 1396–1399 (2008). DOI: 10.1002/anie.200704421.
- [210] Yang, C., Wang, X. & Omary, M. A. Crystallographic Observation of Dynamic Gas Adsorption Sites and Thermal Expansion in a Breathable Fluorous Metal–Organic Framework. *Angew. Chem. Int. Ed.* **48**, 2500–2505 (2009). DOI: 10.1002/anie.200804739.
- [211] Zhou, H.-L. *et al.* Direct visualization of a guest-triggered crystal deformation based on a flexible ultramicroporous framework. *Nat. Commun.* **4**, 2534 (2013). DOI: 10.1038/ncomms3534.
- [212] Zhou, H.-L., Zhang, Y.-B., Zhang, J.-P. & Chen, X.-M. Supramolecular-Jack-like Guest in Ultramicroporous Crystal for Exceptional Thermal Expansion Behaviour. *Nat. Commun.* **6**, 6917 (2015). DOI: 10.1038/ncomms7917.
- [213] Chen, J. *et al.* Tunable thermal expansion in framework materials through redox intercalation. *Nat. Commun.* **8**, 14441 (2017). DOI: 10.1038/ncomms14441.
- [214] Gao, Q. *et al.* Switching Between Giant Positive and Negative Thermal Expansions of a $\text{YFe}(\text{CN})_6$ -based Prussian Blue Analogue Induced by Guest Species. *Angew. Chem. Int. Ed.* **56**, 9023–9028 (2017). DOI: 10.1002/anie.201702955.
- [215] Das, D., Jacobs, T. & Barbour, L. J. Exceptionally Large Positive and Negative Anisotropic Thermal Expansion of an Organic Crystalline Material. *Nat. Mater.* **9**, 36–39 (2010). DOI: 10.1038/nmat2583.
- [216] Bhattacharya, S. & Saha, B. K. Steric guided anomalous thermal expansion in a dimorphic organic system. *CrystEngComm* **16**, 2340–2343 (2014). DOI: 10.1039/C3CE41869C.

Bibliography

- [217] Panda, M. K. *et al.* Colossal positive and negative thermal expansion and thermosalient effect in a pentamorphic organometallic martensite. *Nat. Commun.* **5**, 4811 (2014). DOI: 10.1038/ncomms5811.
- [218] Jones, R. H. *et al.* Colossal thermal expansion and negative thermal expansion in simple halogen bonded complexes. *CrystEngComm* **16**, 237–243 (2014). DOI: 10.1039/C3CE41909F.
- [219] Liu, Y. *et al.* A Shape-Persistent Polyphenylene Spoked Wheel. *J. Am. Chem. Soc.* **138**, 15539–15542 (2016). DOI: 10.1021/jacs.6b10369.
- [220] Piot, L., Marchenko, A., Wu, J., Müllen, K. & Fichou, D. Structural Evolution of Hexa-peri-hexabenzocoronene Adlayers in Heteroepitaxy on n-Pentacontane Template Monolayers. *J. Am. Chem. Soc.* **127**, 16245–16250 (2005). DOI: 10.1021/ja0548844.
- [221] Marie, C., Silly, F., Tortech, L., Müllen, K. & Fichou, D. Tuning the Packing Density of 2D Supramolecular Self-Assemblies at the Solid-Liquid Interface Using Variable Temperature. *ACS Nano* **4**, 1288–1292 (2010). DOI: 10.1021/nm901717k.
- [222] Son, D. *et al.* Multifunctional wearable devices for diagnosis and therapy of movement disorders. *Nat. Nanotechnol.* **9**, 397–404 (2014). DOI: 10.1038/nano.2014.38.
- [223] Haines, C. S. *et al.* New twist on artificial muscles. *PNAS* **113**, 11709–11716 (2016). DOI: 10.1073/pnas.1605273113.
- [224] Pisula, W. *et al.* Relationship between Core Size, Side Chain Length, and the Supramolecular Organization of Polycyclic Aromatic Hydrocarbons. *Chem. Mater.* **17**, 4296–4303 (2005). DOI: 10.1021/cm050251c.
- [225] Wagner, C. *et al.* Repulsion between molecules on a metal: Monolayers and submonolayers of hexa-peri-hexabenzocoronene on Au(111). *Phys. Rev. B* **81**, 035423 (2010). DOI: 10.1103/PhysRevB.81.035423.
- [226] Liu, W., Tkatchenko, A. & Scheffler, M. Modeling Adsorption and Reactions of Organic Molecules at Metal Surfaces. *Acc. Chem. Res.* **47**, 3369–3377 (2014). DOI: 10.1021/ar500118y.
- [227] Mateo Marti, E., Barlow, S. M., Haq, S. & Raval, R. Bonding and assembly of the chiral amino acid S-proline on Cu(110): The influence of structural rigidity. *Surf. Sci.* **501**, 191–202 (2002). DOI: 10.1016/S0039-6028(01)02026-X.
- [228] Raval, R. Creating chiral architectures at metal surfaces. *J. Phys.: Condens. Matter* **14**, 4119–4132 (2002). DOI: 10.1088/0953-8984/14/16/305.
- [229] Cortés, R. *et al.* Coexistence of Racemic and Homochiral Two-Dimensional Lattices Formed by a Prochiral Molecule: Dicarboxystilbene on Cu(110). *Nano Lett.* **8**, 4162–4167 (2008). DOI: 10.1021/nl801592c.
- [230] Trant, A. G. & Baddeley, C. J. Chiral Recognition at One-Dimensional Metal-Organic Coordination Networks Initiates the Ordering of Prochiral Catalytic Reagent Methylacetoacetate on Au(111). *Langmuir* **27**, 1788–1795 (2011). DOI: 10.1021/la1040097.

- [231] Hauptmann, N. *et al.* Surface Control of Alkyl Chain Conformations and 2D Chiral Amplification. *J. Am. Chem. Soc.* **135**, 8814–8817 (2013). DOI: 10.1021/ja4036187.
- [232] Madden, D. C., Bentley, M. L., Jenkins, S. J. & Driver, S. M. On the role of molecular chirality in amino acid self-organisation on Cu(311). *Surf. Sci.* **629**, 81–87 (2014). DOI: 10.1016/j.susc.2014.03.025.
- [233] Ernst, K.-H. Stereochemistry of 2D Molecular Crystallization. *CHIMIA* **68**, 49–49 (2014). DOI: 10.2533/chimia.2014.49.
- [234] Seljamäe-Green, R. T. *et al.* Assembly of a Chiral Amino Acid on an Unreactive Surface: (S)-Proline on Au(111). *Langmuir* **30**, 3495–3501 (2014). DOI: 10.1021/la500336c.
- [235] Zaera, F. Chirality in adsorption on solid surfaces. *Chem. Soc. Rev.* **46**, 7374–7398 (2017). DOI: 10.1039/C7CS00367F.
- [236] Mairena, A. *et al.* Heterochiral recognition among functionalized heptahelicenes on noble metal surfaces. *Chem. Commun.* **55**, 10595–10598 (2019). DOI: 10.1039/C9CC05317D.
- [237] Verstraete, L. *et al.* Chiral Adsorption Conformations of Long-Chain n-Alkanes Induced by Lattice Mismatch. *J. Phys. Chem. C* **125**, 1557–1563 (2021). DOI: 10.1021/acs.jpcc.0c09825.
- [238] Böhringer, M., Morgenstern, K., Schneider, W.-D. & Berndt, R. Separation of a Racemic Mixture of Two-Dimensional Molecular Clusters by Scanning Tunneling Microscopy. *Angew. Chem. Int. Ed.* **38**, 821–823 (1999). DOI: 10.1002/(SICI)1521-3773(19990315)38%3A6;821%3A%3AAID-ANIE821;3.0.CO%3B2-A.
- [239] Yang, B. *et al.* Direct Observation of Enantiospecific Substitution in a Two-Dimensional Chiral Phase Transition. *J. Am. Chem. Soc.* **132**, 10440–10444 (2010). DOI: 10.1021/ja102989y.
- [240] Shiotari, A. *et al.* Chiral Discrimination and Manipulation of Individual Heptahelicene Molecules on Cu(001) by Noncontact Atomic Force Microscopy. *J. Phys. Chem. C* (2018). DOI: 10.1021/acs.jpcc.8b00487.
- [241] Koch, S. *Investigation of Hexagonal 2D Super Structures by Dynamic Force Spectroscopy: Boron Nitride and Graphene on Transition Metals*. Ph.D. thesis, University of Basel, Basel (2012). URL http://edoc.unibas.ch/diss/DissB_9932. DOI: 10.5451/unibas-005976956.
- [242] Chen, Z., Lin, Y.-M., Rooks, M. J. & Avouris, P. Graphene nano-ribbon electronics. *Phys. E: Low-Dimens. Syst. Nanostructures* **40**, 228–232 (2007). DOI: 10.1016/j.physe.2007.06.020.
- [243] Ruffieux, P. *et al.* Electronic Structure of Atomically Precise Graphene Nanoribbons. *ACS Nano* **6**, 6930–6935 (2012). DOI: 10.1021/nn3021376.
- [244] Magda, G. Z. *et al.* Room-temperature magnetic order on zigzag edges of narrow graphene nanoribbons. *Nature* **514**, 608–611 (2014). DOI: 10.1038/nature13831.

Bibliography

- [245] El Abbassi, M. *et al.* Controlled Quantum Dot Formation in Atomically Engineered Graphene Nanoribbon Field-Effect Transistors. *ACS Nano* **14**, 5754–5762 (2020). DOI: 10.1021/acsnano.0c00604.
- [246] Barone, V., Hod, O. & Scuseria, G. E. Electronic Structure and Stability of Semiconducting Graphene Nanoribbons. *Nano Lett.* **6**, 2748–2754 (2006). DOI: 10.1021/nl0617033.
- [247] Son, Y.-W., Cohen, M. L. & Louie, S. G. Energy Gaps in Graphene Nanoribbons. *Phys. Rev. Lett.* **97**, 216803 (2006). DOI: 10.1103/PhysRevLett.97.216803.
- [248] Han, M. Y., Özyilmaz, B., Zhang, Y. & Kim, P. Energy band-gap engineering of graphene nanoribbons. *Phys. Rev. Lett.* **98**, 206805 (2007). DOI: 10.1103/PhysRevLett.98.206805.
- [249] Tao, C. *et al.* Spatially resolving edge states of chiral graphene nanoribbons. *Nat. Phys.* **7**, 616–620 (2011). DOI: 10.1038/nphys1991.
- [250] Baringhaus, J. *et al.* Exceptional ballistic transport in epitaxial graphene nanoribbons. *Nature* **506**, 349–354 (2014). DOI: 10.1038/nature12952.
- [251] Aprojanz, J. *et al.* Ballistic tracks in graphene nanoribbons. *Nat. Commun.* **9**, 4426 (2018). DOI: 10.1038/s41467-018-06940-5.
- [252] Liu, J. *et al.* Toward Cove-Edged Low Band Gap Graphene Nanoribbons. *J. Am. Chem. Soc.* **137**, 6097–6103 (2015). DOI: 10.1021/jacs.5b03017.
- [253] Gemayel, M. E. *et al.* Graphene nanoribbon blends with P3HT for organic electronics. *Nanoscale* **6**, 6301–6314 (2014). DOI: 10.1039/C4NR00256C.
- [254] Gröning, O. *et al.* Engineering of robust topological quantum phases in graphene nanoribbons. *Nature* **560**, 209–213 (2018). DOI: 10.1038/s41586-018-0375-9.
- [255] Fu, Y. *et al.* On-Surface Synthesis of NBN-Doped Zigzag-Edged Graphene Nanoribbons. *Angew. Chem. Int. Ed.* **59**, 8873–8879 (2020). DOI: 10.1002/anie.202000488.
- [256] Zhou, X. & Yu, G. Modified Engineering of Graphene Nanoribbons Prepared via On-Surface Synthesis. *Adv. Mater.* **32**, 1905957 (2020). DOI: 10.1002/adma.201905957.
- [257] Götz, A. *et al.* Band structure modulation by methoxy-functionalization of graphene nanoribbons. *J. Mater. Chem. C* **10**, 4173–4181 (2022). DOI: 10.1039/D1TC05695F.
- [258] Grill, L. *et al.* Nano-architectures by covalent assembly of molecular building blocks. *Nat. Nanotechnol.* **2**, 687–691 (2007). DOI: 10.1038/nnano.2007.346.
- [259] van der Lit, J. *et al.* Suppression of electron–vibron coupling in graphene nanoribbons contacted via a single atom. *Nat. Commun.* **4**, 2023 (2013). DOI: 10.1038/ncomms3023.
- [260] Ruffieux, P. *et al.* On-surface synthesis of graphene nanoribbons with zigzag edge topology. *Nature* **531**, 489–492 (2016). DOI: 10.1038/nature17151.
- [261] Pizzochero, M. *et al.* Edge Disorder in Bottom-Up Zigzag Graphene Nanoribbons: Implications for Magnetism and Quantum Electronic Transport. *J. Phys. Chem. Lett.* 4692–4696 (2021). DOI: 10.1021/acs.jpcllett.1c00921.

- [262] Yang, Y., Wang, L., Zhang, Z. & Cui, P. Prediction of a Kinetic Pathway for Fabricating the Narrowest Zigzag Graphene Nanoribbons on Cu(111). *J. Phys. Chem. C* **125**, 21933–21942 (2021). DOI: 10.1021/acs.jpcc.1c05660.
- [263] Chen, Y.-C. *et al.* Tuning the Band Gap of Graphene Nanoribbons Synthesized from Molecular Precursors. *ACS Nano* **7**, 6123–6128 (2013). DOI: 10.1021/nm401948e.
- [264] Kawai, S. *et al.* Atomically controlled substitutional boron-doping of graphene nanoribbons. *Nat. Commun.* **6**, 8098 (2015). DOI: 10.1038/ncomms9098.
- [265] Wang, S. *et al.* Giant edge state splitting at atomically precise graphene zigzag edges. *Nat. Commun.* **7**, 11507 (2016). DOI: 10.1038/ncomms11507.
- [266] Sun, Q. *et al.* Coupled Spin States in Armchair Graphene Nanoribbons with Asymmetric Zigzag Edge Extensions. *Nano Lett.* **20**, 6429–6436 (2020). DOI: 10.1021/acs.nanolett.0c02077.
- [267] Schneider, S. & Hoffmann-Vogel, R. Electrostatic forces above graphene nanoribbons and edges interpreted as partly hydrogen-free. *Nanoscale* **12**, 17895–17901 (2020). DOI: 10.1039/D0NR03348K.
- [268] Friedrich, N. *et al.* Magnetism of Topological Boundary States Induced by Boron Substitution in Graphene Nanoribbons. *Phys. Rev. Lett.* **125**, 146801 (2020). DOI: 10.1103/PhysRevLett.125.146801.
- [269] Pawlak, R. *et al.* Bottom-up Synthesis of Nitrogen-Doped Porous Graphene Nanoribbons. *J. Am. Chem. Soc.* **142**, 12568–12573 (2020). DOI: 10.1021/jacs.0c03946.
- [270] Lawrence, J. *et al.* Probing the Magnetism of Topological End States in 5-Armchair Graphene Nanoribbons. *ACS Nano* **14**, 4499–4508 (2020). DOI: 10.1021/acsnano.9b10191.
- [271] Qiu, Z. *et al.* Exploring Intramolecular Methyl–Methyl Coupling on a Metal Surface for Edge-Extended Graphene Nanoribbons. *Organic Materials* **03**, 128–133 (2021). DOI: 10.1055/s-0041-1726295.
- [272] Yang, H. *et al.* Fabrication of sulfur-doped cove-edged graphene nanoribbons on Au(111). *Chinese Phys. B* (2021). DOI: 10.1088/1674-1056/abfbd0.
- [273] Rizzo, D. J. *et al.* Rationally Designed Topological Quantum Dots in Bottom-Up Graphene Nanoribbons. *ACS Nano* **15**, 20633–20642 (2021). DOI: 10.1021/acsnano.1c09503.
- [274] Berdonces-Layunta, A. *et al.* Chemical Stability of (3,1)-Chiral Graphene Nanoribbons. *ACS Nano* **15**, 5610–5617 (2021). DOI: 10.1021/acsnano.1c00695.
- [275] Pawlak, R. *et al.* On-Surface Synthesis of Nitrogen-Doped Kagome Graphene. *Angew. Chem.* **133**, 8451–8456 (2021). DOI: 10.1002/ange.202016469.
- [276] Sun, Q. *et al.* Evolution of the Topological Energy Band in Graphene Nanoribbons. *J. Phys. Chem. Lett.* **12**, 8679–8684 (2021). DOI: 10.1021/acs.jpcl.1c02541.

Bibliography

- [277] Kawai, S. *et al.* Three-dimensional graphene nanoribbons as a framework for molecular assembly and local probe chemistry. *Sci. Adv.* **6**, eaay8913 (2020). DOI: 10.1126/sciadv.aay8913.
- [278] Kittelmann, M., Nimmrich, M., Lindner, R., Gourdon, A. & Kühnle, A. Sequential and Site-Specific On-Surface Synthesis on a Bulk Insulator. *ACS Nano* **7**, 5614–5620 (2013). DOI: 10.1021/nn402018w.
- [279] Ma, C. *et al.* Controllable conversion of quasi-freestanding polymer chains to graphene nanoribbons. *Nat. Commun.* **8**, 14815 (2017). DOI: 10.1038/ncomms14815.
- [280] Deniz, O. *et al.* Revealing the Electronic Structure of Silicon Intercalated Armchair Graphene Nanoribbons by Scanning Tunneling Spectroscopy. *Nano Lett.* **17**, 2197–2203 (2017). DOI: 10.1021/acs.nanolett.6b04727.
- [281] Jacobse, P. H., Mangnus, M. J. J., Zevenhuizen, S. J. M. & Swart, I. Mapping the Conductance of Electronically Decoupled Graphene Nanoribbons. *ACS Nano* **12**, 7048–7056 (2018). DOI: 10.1021/acsnano.8b02770.
- [282] Narita, A., Chen, Z., Chen, Q. & Müllen, K. Solution and on-surface synthesis of structurally defined graphene nanoribbons as a new family of semiconductors. *Chem. Sci.* **10**, 964–975 (2019). DOI: 10.1039/C8SC03780A.
- [283] Yokoyama, A. *et al.* Chain-Growth Polymerization for the Synthesis of Polyfluorene via Suzuki–Miyaura Coupling Reaction from an Externally Added Initiator Unit. *J. Am. Chem. Soc.* **129**, 7236–7237 (2007). DOI: 10.1021/ja070313v.
- [284] Vo, T. H. *et al.* Large-scale solution synthesis of narrow graphene nanoribbons. *Nat. Commun.* **5**, 3189 (2014). DOI: 10.1038/ncomms4189.
- [285] Li, G., Yoon, K.-Y., Zhong, X., Zhu, X. & Dong, G. Efficient Bottom-Up Preparation of Graphene Nanoribbons by Mild Suzuki–Miyaura Polymerization of Simple Triaryl Monomers. *Eur. J. Chem.* **22**, 9116–9120 (2016). DOI: 10.1002/chem.201602007.
- [286] Yoon, K.-Y. & Dong, G. Liquid-phase bottom-up synthesis of graphene nanoribbons. *Mater. Chem. Front.* **4**, 29–45 (2019). DOI: 10.1039/C9QM00519F.
- [287] Qiu, Z., Narita, A. & Müllen, K. Carbon Nanostructures by Macromolecular Design – From Branched Polyphenylenes to Nanographenes and Graphene Nanoribbons. *Faraday Discuss.* (2020). DOI: 10.1039/D0FD00023J.
- [288] S. Jassas, R. *et al.* Scholl reaction as a powerful tool for the synthesis of nanographenes: A systematic review. *RSC Adv.* **11**, 32158–32202 (2021). DOI: 10.1039/D1RA05910F.
- [289] Preis, T. *et al.* Graphene nanoribbons on hexagonal boron nitride: Deposition and transport characterization. *Appl. Phys. Lett.* **114**, 173101 (2019). DOI: 10.1063/1.5065568.
- [290] Jolly, A., Miao, D., Daigle, M. & Morin, J.-F. Emerging Bottom-Up Strategies for the Synthesis of Graphene Nanoribbons and Related Structures. *Angew. Chem. Int. Ed.* **59**, 4624–4633 (2020). DOI: 10.1002/anie.201906379.

- [291] Rogers, C. *et al.* Synergistic Enhancement of Electrocatalytic CO₂ Reduction with Gold Nanoparticles Embedded in Functional Graphene Nanoribbon Composite Electrodes. *J. Am. Chem. Soc.* **139**, 4052–4061 (2017). DOI: 10.1021/jacs.6b12217.
- [292] Huang, Y. *et al.* Supramolecular Nanostructures of Structurally Defined Graphene Nanoribbons in the Aqueous Phase. *Angew. Chem. Int. Ed.* **57**, 3366–3371 (2018). DOI: 10.1002/anie.201712637.
- [293] Joshi, D. *et al.* Super-Resolution Imaging of Clickable Graphene Nanoribbons Decorated with Fluorescent Dyes. *J. Am. Chem. Soc.* **140**, 9574–9580 (2018). DOI: 10.1021/jacs.8b04679.
- [294] Xu, F. *et al.* Tunable Superstructures of Dendronized Graphene Nanoribbons in Liquid Phase. *J. Am. Chem. Soc.* **141**, 10972–10977 (2019). DOI: 10.1021/jacs.9b04927.
- [295] Tan, Y.-Z. *et al.* Atomically precise edge chlorination of nanographenes and its application in graphene nanoribbons. *Nat. Commun.* **4**, 2646 (2013). DOI: 10.1038/ncomms3646.
- [296] Keerthi, A. *et al.* Edge Functionalization of Structurally Defined Graphene Nanoribbons for Modulating the Self-Assembled Structures. *J. Am. Chem. Soc.* **139**, 16454–16457 (2017). DOI: 10.1021/jacs.7b09031.
- [297] Slota, M. *et al.* Magnetic edge states and coherent manipulation of graphene nanoribbons. *Nature* **557**, 691–695 (2018). DOI: 10.1038/s41586-018-0154-7.
- [298] Xu, F., Yu, H., Sadrzadeh, A. & Yakobson, B. I. Riemann Surfaces of Carbon as Graphene Nanosolenoids. *Nano Lett.* **16**, 34–39 (2016). DOI: 10.1021/acs.nanolett.5b02430.
- [299] Schuster, N. J. *et al.* The Structural Origins of Intense Circular Dichroism in a Wagging Helicene Nanoribbon. *J. Am. Chem. Soc.* **142**, 7066–7074 (2020). DOI: 10.1021/jacs.0c00646.
- [300] Ajayakumar, M. R. *et al.* On-surface synthesis of porous graphene nanoribbons containing nonplanar [14]annulene pores. *Journal of Polymer Science* **60**, 1912–1917 (2022). DOI: 10.1002/pol.20220003.
- [301] Daigle, M., Miao, D., Lucotti, A., Tommasini, M. & Morin, J.-F. Helically Coiled Graphene Nanoribbons. *Angew. Chem. Int. Ed.* **56**, 6213–6217 (2017). DOI: 10.1002/anie.201611834.
- [302] Castro-Fernández, S. *et al.* Two-Photon Absorption Enhancement by the Inclusion of a Tropone Ring in Distorted Nanographene Ribbons. *Angew. Chem. Int. Ed.* **59**, 7139–7145 (2020). DOI: 10.1002/anie.202000105.
- [303] Niu, W. *et al.* A Curved Graphene Nanoribbon with Multi-Edge Structure and High Intrinsic Charge Carrier Mobility. *J. Am. Chem. Soc.* **142**, 18293–18298 (2020). DOI: 10.1021/jacs.0c07013.
- [304] Ma, S. *et al.* Supertwistacene: A Helical Graphene Nanoribbon. *J. Am. Chem. Soc.* **142**, 16887–16893 (2020). DOI: 10.1021/jacs.0c08555.

Bibliography

- [305] Shekhirev, M. *et al.* Aggregation of atomically precise graphene nanoribbons. *RSC Adv.* **7**, 54491–54499 (2017). DOI: 10.1039/C7RA08049B.
- [306] Radocea, A. *et al.* Solution-Synthesized Chevron Graphene Nanoribbons Exfoliated onto H:Si(100). *Nano Lett.* **17**, 170–178 (2017). DOI: 10.1021/acs.nanolett.6b03709.
- [307] Ran, W. *et al.* Depositing Molecular Graphene Nanoribbons on Ag(111) by Electro-spray Controlled Ion Beam Deposition: Self-Assembly and On-Surface Transformations. *Angew. Chem. Int. Ed.* **61**, e202111816 (2022). DOI: 10.1002/anie.202111816.
- [308] Eigler, D. M. & Schweizer, E. K. Positioning single atoms with a scanning tunnelling microscope. *Nature* **344**, 524–526 (1990). DOI: 10.1038/344524a0.
- [309] Eigler, D. M., Lutz, C. P. & Rudge, W. E. An atomic switch realized with the scanning tunnelling microscope. *Nature* **352**, 600–603 (1991). DOI: 10.1038/352600a0.
- [310] Ko, W., Ma, C., Nguyen, G. D., Kolmer, M. & Li, A.-P. Atomic-Scale Manipulation and In Situ Characterization with Scanning Tunneling Microscopy. *Adv. Funct. Mater.* **29**, 1903770 (2019). DOI: 10.1002/adfm.201903770.
- [311] Meyer, G. A simple low-temperature ultrahigh-vacuum scanning tunneling microscope capable of atomic manipulation. *Rev. Sci. Instrum.* **67**, 2960–2965 (1996). DOI: 10.1063/1.1147080.
- [312] Meyer, G., Zöphel, S. & Rieder, K. H. Manipulation of atoms and molecules with a low temperature scanning tunneling microscope. *Appl. Phys. A* **63**, 557–564 (1996). DOI: 10.1007/BF01567211.
- [313] Moresco, F. *et al.* Low temperature manipulation of big molecules in constant height mode. *Appl. Phys. Lett.* **78**, 306–308 (2001). DOI: 10.1063/1.1339251.
- [314] Moresco, F. Manipulation of large molecules by low-temperature STM: Model systems for molecular electronics. *Phys. Rep.* **399**, 175–225 (2004). DOI: 10.1016/j.physrep.2004.08.001.
- [315] Chen, C. *et al.* Graphene Nanoribbons Under Mechanical Strain. *Adv. Mater.* **27**, 303–309 (2015). DOI: 10.1002/adma.201403750.
- [316] Kawai, S. *et al.* Superlubricity of graphene nanoribbons on gold surfaces. *Science* **351**, 957–961 (2016). DOI: 10.1126/science.aad3569.
- [317] Pawlak, R. *et al.* Single-molecule manipulation experiments to explore friction and adhesion. *J. Phys. D: Appl. Phys.* **50**, 113003 (2017). DOI: 10.1088/1361-6463/aa599d.
- [318] Beton, P. H., Dunn, A. W. & Moriarty, P. Manipulation of C₆₀ molecules on a Si surface. *Appl. Phys. Lett.* **67**, 1075–1077 (1995). DOI: 10.1063/1.114469.
- [319] Cuberes, M. T., Schlittler, R. R. & Gimzewski, J. K. Room-temperature repositioning of individual C₆₀ molecules at Cu steps: Operation of a molecular counting device. *Appl. Phys. Lett.* **69**, 3016–3018 (1996). DOI: 10.1063/1.116824.
- [320] Jung, T. A., Schlittler, R. R., Gimzewski, J. K., Tang, H. & Joachim, C. Controlled Room-Temperature Positioning of Individual Molecules: Molecular Flexure and Motion. *Science* **271**, 181–184 (1996). DOI: 10.1126/science.271.5246.181.

-
- [321] Fishlock, T. W., Oral, A., Egdell, R. G. & Pethica, J. B. Manipulation of atoms across a surface at room temperature. *Nature* **404**, 743–745 (2000). DOI: 10.1038/35008030.
- [322] Griessl, S. J. H. *et al.* Room-Temperature Scanning Tunneling Microscopy Manipulation of Single C60 Molecules at the Liquid-Solid Interface: Playing Nanosoccer. *J. Phys. Chem. B* **108**, 11556–11560 (2004). DOI: 10.1021/jp049521p.
- [323] Kawai, S. *et al.* Atom manipulation on an insulating surface at room temperature. *Nat. Commun.* **5**, 4403 (2014). DOI: 10.1038/ncomms5403.
- [324] van der Lit, J., Jacobse, P. H., Vanmaekelbergh, D. & Swart, I. Bending and buckling of narrow armchair graphene nanoribbons via STM manipulation. *New J. Phys.* **17**, 053013 (2015). DOI: 10.1088/1367-2630/17/5/053013.
- [325] Bronner, C., Haase, A. & Tegeder, P. Image potential states at chevron-shaped graphene nanoribbons /Au(111) interfaces. *Phys. Rev. B* **91**, 045428 (2015). DOI: 10.1103/PhysRevB.91.045428.
- [326] Khomyakov, P. A. *et al.* First-principles study of the interaction and charge transfer between graphene and metals. *Phys. Rev. B* **79**, 195425 (2009). DOI: 10.1103/PhysRevB.79.195425.
- [327] Schulzendorf, M. *et al.* Altering the Properties of Graphene on Cu(111) by Intercalation of Potassium Bromide. *ACS Nano* **13**, 5485–5492 (2019). DOI: 10.1021/acsnano.9b00278.
- [328] Kawai, S., Canova, F. F., Glatzel, T., Foster, A. S. & Meyer, E. Atomic-scale dissipation processes in dynamic force spectroscopy. *Phys. Rev. B* **84**, 115415 (2011). DOI: 10.1103/PhysRevB.84.115415.
- [329] Koch, S. *et al.* Elastic Response of Graphene Nanodomes. *ACS Nano* **7**, 8 (2013). DOI: 10.1021/nn304473r.

Appendix

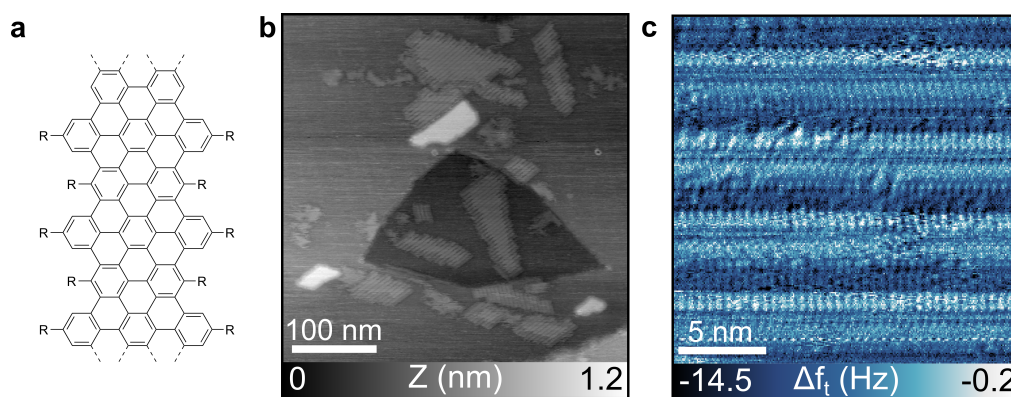


Figure A.1: Alkyl chain fragments of a "cove"-type GNR with high alkyl chain functionalization. **a**, Chemical structure of the highly alkyl chain equipped "cove"-type GNR. **b**, AFM topography image of alkyl chain aggregates formed after deposition of a "cove"-type GNR ($A_2 = 1.2$ nm, $\Delta f_2 = -82$ Hz). **c**, Torsional frequency shift image inside an aggregate showing aligned alkyl chains ($A_2 = 800$ pm, $\Delta f_2 = -90$ Hz, $A_t = 40$ pm).

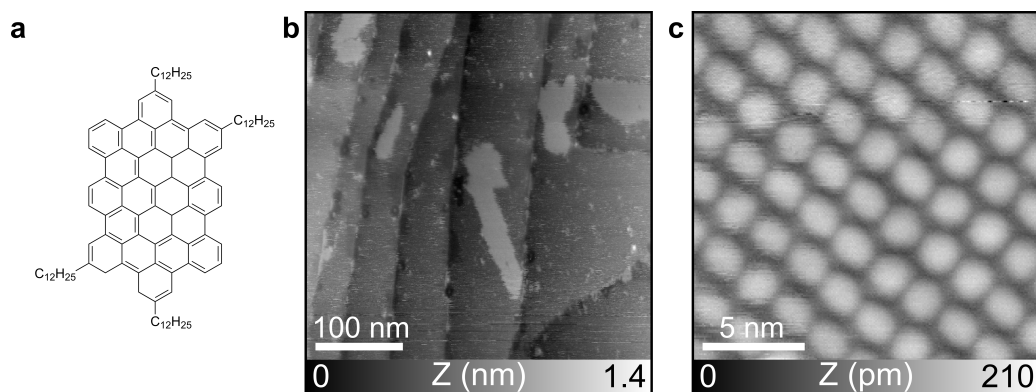


Figure A.2: $C_{60}-4C_{12}H_{25}$ molecule assemblies deposited by ESD. **a**, Chemical structure of dodecyl equipped $C_{60}-4C_{12}H_{25}$. **b**, Large scale nc-AFM topography image of $C_{60}-4C_{12}H_{25}$ molecule assemblies deposited by ESD ($A_2 = 600$ pm, $\Delta f_2 = -20$ Hz). **c**, Close-up image of a $C_{60}-4C_{12}H_{25}$ molecule network ($A_2 = 600$ pm, $\Delta f_2 = -31$ Hz).

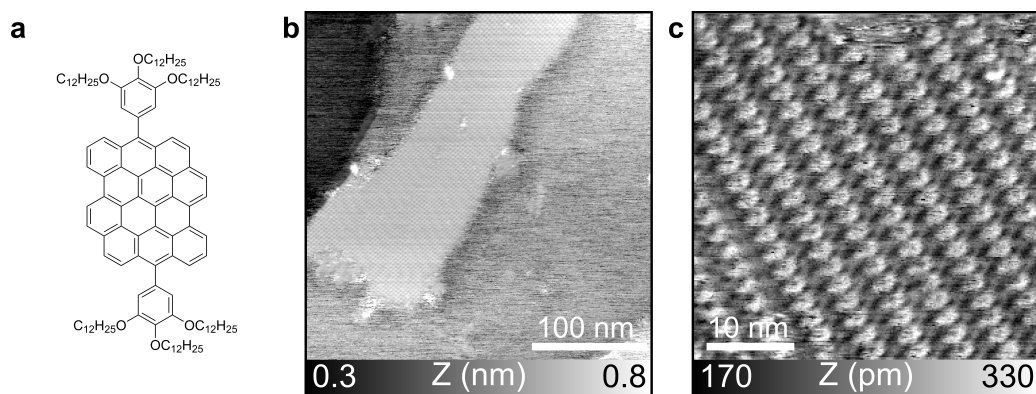
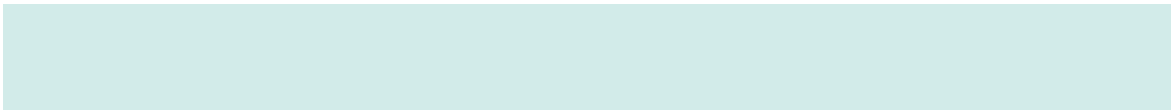


Figure A.3: DBOV-TDOP molecule assemblies after ESD. **a**, Chemical structure of Dibenzo[hi, st]ovalene-tris(dodecyloxy)phenyl (DBOV-TDOP). HB is visible below the molecular island. **b**, Large scale nc-AFM topography image of DBOV-TDOP molecule assemblies ($A_1 = 3$ nm, $\Delta f_1 = -50$ Hz). **c**, Close-up image of a DBOV-TDOP molecule network ($A_2 = 600$ pm, $\Delta f_2 = -36$ Hz).



Abbreviations

AC	Alternating current
AFM	Atomic force microscopy/microscope
AM	Amplitude modulation
CPD	Contact potential difference
DC	Direct current
ESD	Electrospray deposition
ESI	Electrospray ionization
fcc	face-centered cubic
FM	Frequency modulation
GNR	Graphene nanoribbons
HBC	Hexabenzocoronene
hcp	hexagonal close-packed
KPFM	Kelvin Probe Force Microscopy
LT	Low temperature
nc	Non-contact
PLL	Phase locked loop
QMB	Quartz micro balance
QPD	Quadrant photo diode
RT	Room temperature
SEM	Scanning electron microscopy/microscope
SLD	Superlum diode
SPM	Scanning probe microscopy/microscope
STM	Scanning tunneling microscopy/microscope
SW	Spoked wheel molecule
TE	Thermal evaporation
UHV	Ultra-high vacuum
XPS	X-ray photoelectron spectroscopy
2D	Two-dimensional
3D	Three-dimensional

Symbols

Latin letters

A	Amplitude
A_1	Oscillation amplitude of the first flexural resonance
A_2	Oscillation amplitude of the second flexural resonance
A_t	Oscillation amplitude of the torsional resonance
A_H	Hammaker constant
a	Lattice parameter
C	Capacitance
E	Energy
E_{bond}	Bonding energy
e	Elementary charge
F	Force
F_{chem}	Chemical force between tip and sample
F_{el}	Electrostatic force
F_{int}	Interaction force
F_{vdW}	Van der Waals force
f	Frequency
f_1	Eigenfrequency
f_2	Second flexural resonance frequency
f_t	First torsional resonance frequency

Nomenclature

I_t	Tunneling current
Q	Quality factor
q_r	critical charge
r	Radius of the tip
R	Radius of a droplet
T	Temperature
V	Potential difference between tip and sample
V_{AC}	Alternative current voltage
V_{Bias}	Bias voltage, in this work: STM tip bias, nc-AFM sample bias
V_{CPD}	Voltage compensating the contact potential difference
V_{DC}	Direct current voltage
x	Coordinate of the horizontal scan axis perpendicular to the cantilever
y	Coordinate of the horizontal scan axis along the cantilever extension
z	Coordinate of the vertical axis between tip and sample
z_{offset}	Multipass offset distance

Greek letters

α	Coefficient of thermal expansion
Δf	Frequency shift
$\Delta\phi$	Work function difference
γ	Surface tension of liquid
ϵ_0	Vacuum permittivity
κ	Decay length of bounding interaction
σ	Equilibrium distance
ϕ	Work function
ω	Angular frequency of the oscillation

Acknowledgments

AT last, I want to express my gratitude to everyone, who made this work possible, each in their own way. Be it with the science, by corrections, in the evaluations or in moral and general support.

First, I would like to thank Prof. Ernst Meyer for allowing me the opportunity to perform this work in the excellent environment of his group and all his support. Starting with my project thesis and then following with my master thesis, I always enjoyed my work in the lab, but also the work atmosphere with communal lunches and excursions.

Second, I thank Dr. Clemens Barth for evaluating this thesis as the external expert and Prof. Martino Poggio for joining my committee as second supervisor and his inputs during our yearly meetings.

This thesis and my work with AFM and ESD would not have been possible without the expert instructions and advice provided by Dr. Antoine Hinaut. He supervised with exceptionally patience and involvement my work over the last four years of PhD work. Working closely with me on keeping the system running and on measurements, but also collaborating on publications and finally also correcting this thesis. I always greatly enjoyed working but also just talking and discussing with You, meeting Your boys and Angela, having crêpes, or going swimming in the Rhein. Your talent for hiking is also greatly appreciated.

I want to express my gratitude to PD Dr. Thilo Glatzel for his expert advice, vast scientific insights and KPFM abilities, for bringing in new students to show AFM to and for correcting this thesis.

For the important calculations and his friendship, I thank Dr. Gui Vilhena. Our discussions always helped bring my work but also me personally forward. Swimming in the Rhein and also the trips to conferences were some highlights. Your joy in snowboarding still brings me joy.

To my lab partner and skiing companion Dr. Yiming Song I also express my gratitude. The times in the lab and otherwise with you were always very fun. Discussing about anything, science or otherwise was of great enjoyment to me and helped me

Acknowledgments

greatly with this work. Our skiing trips to Feldberg and other excursions added some much needed sports and excitement after the long corona time.

I also thank Dr. Rémy Pawlak for his support during the LT measurements and the on-surface reactions, even when times were busy and for his valuable scientific inputs.

For his exceptional technical support and hiking abilities, I want to thank Yves Pellmont. Whenever, we faced serious issues with the microscope or system, he was there to help, just to name a few replacing the fiber when I started and even replacing the second mirror and cabling close to the finalization of my measurements. Thank you.

I also want to thank all my colleagues past and present in Nanolino group for the fun working environment. In particular I want to mention Zhao Liu, Shuyu Huang and Gema Navarro for the nice times in RT lab, Carl Drechsel, Philipp D'Astolfo and Alexina Ollier for the trips and the visits to conferences. Paul Huret and Jung-Ching Liu for the skiing trips and together with Fabian Sanchez and Kunal Soni for the nice office environment even though I spent little time outside of the lab. Marco Zutter for our discussions about anything and the camaraderie. Dr. Marcin Kisiel for his scientific insights and especially for his capacity meter, Dr. Laurent Marot for facilitating all the security risky solvent uses and keeping the building running. Roland Steiner for his technical help and the fun skiing in Andermatt.

For their invaluable support and help, and always in any situation being there for me, I thank my parents and my siblings. Without You I would not be where and who I am today. You always believed in me and helped me in any way possible. Mama, thank You for everything You have invested in me, helping me through my struggles in bachelor studies, going inline skating with me, and everything else. Papa, also thank you for everything you have done for me, your support and help always brought me forward even when times were hard. Our discussion, be it politics, society or science, always gave me new insights and inputs. Together you gave me a precious childhood lacking nothing with all the love and support one could wish for.

To all my siblings thank you for being there, making my life since childhood interesting, fun and fulfilling.

Christopher, You paved the way for many of my choices, to study in Basel, for school or also for sports and eased many of my decisions. Our trips to Hawaii and the US mainland still remain highlights of traveling.

Christiane, with our small gap in age we spent a lot of time together even during our studies. Dancing has been a joy over the last decade but also your support especially during the bachelor even though we are not quite in the same field was invaluable. Kitesurfing together is and will hopefully be a lot of fun.

Viktoria, as our youngest, always sporty and energetic, but also listening to me and supporting me. As the last two to move out fully, a lot of our time was spent together in the last years and we had many fun trips and times.

All five of you have my eternal gratitude and love.

List of Publications & Communications

Peer-reviewed Journal Publications

1. **Scherb, S.**; Hinaut, A.; Pawlak, R.; Vilhena J. G.; Song Y.; Müllen K.; Glatzel, Th.; Narita, A. and Meyer, E. Tuning the thermal expansion of supramolecular networks by surface and alkyl chain length modification. *paper in preparation* (2022).
2. **Scherb, S.**; Hinaut, A.; Yao X.; Götz A.; Wang X.-Y.; Hu Y.; Qiu Z.; Song Y.; Müllen K.; Glatzel, Th.; Narita, A. and Meyer, E. Solution synthesized extended graphene nanoribbons deposited by high-vacuum electrospray deposition. *under review* (2022).
3. Song, Y.; Hinaut, A.; **Scherb, S.**; Pellmont, Y.; Pawlak, R.; Huang S.; Liu, Z.; Glatzel, Th. and Meyer, E. Observation of robust superlubricity of MoS₂ on Au(111) in ultrahigh vacuum. *Applied Surface Science* (2022). DOI: [10.1016/j.apsusc.2022.154230](https://doi.org/10.1016/j.apsusc.2022.154230)
4. Hou, I. C.-Y.; Hinaut, A.; **Scherb, S.**; Meyer, E.; Narita A. and Müllen, K. Synthesis of Giant Dendritic Polyphenylenes with 366 and 546 Carbon Atoms and Their High-vacuum Electrospray Deposition. *Chemistry - An Asian Journal* (2022). DOI: [10.1002/asia.202200220](https://doi.org/10.1002/asia.202200220)
5. Liu, Z.; Hinaut, A.; Peeters, S.; **Scherb, S.**; Meyer, E.; Righi, M. C. and Glatzel, Th. 2D KBr/Graphene Heterostructures—Influence on Work Function and Friction. *Nanomaterials* **12**, 968 (2022). DOI: [10.3390/nano12060968](https://doi.org/10.3390/nano12060968)
6. Hinaut, A.; **Scherb, S.**; Freund, S.; Glatzel, Th. and Meyer, E. Influence of electrospray deposition on C₆₀ molecular assemblies. *Beilstein Journal of Nanotechnology* **12**, 552-558 (2021). DOI: [10.3762/bjnano.12.45](https://doi.org/10.3762/bjnano.12.45)
7. Liu, Z.; Hinaut, A.; Peeters, S.; **Scherb, S.**; Meyer, E.; Righi, M. C. and Glatzel, Th. Reconstruction of a 2D layer of KBr on Ir(111) and electromechanical al-

List of Publications & Communications

teration by graphene. *Beilstein Journal of Nanotechnology* **12**, 432-439 (2021). DOI: [10.3762/bjnano.12.35](https://doi.org/10.3762/bjnano.12.35)

8. **Scherb, S.**; Hinaut, A.; Pawlak, R.; Vilhena J. G.; Liu Y.; Freund S.; Liu Z.; Feng X.; Müllen K.; Glatzel, Th.; Narita, A. and Meyer, E. Giant thermal expansion of a two-dimensional supramolecular network triggered by alkyl chain motion. *Communications Materials* **1**, 1-7 (2020). DOI: [10.1038/s43246-020-0009-2](https://doi.org/10.1038/s43246-020-0009-2)

Presentations

1. Tuning thermal expansion of supramolecular networks by alkyl chain modification. **Scherb, S.**; Hinaut, A.; Pawlak, R.; Vilhena, J. G.; Song Y.; Müllen K.; Glatzel, Th.; Narita A. and Meyer, E. *The 23rd International Conference on Non-contact Atomic Force Microscopy*, 2022-08-05, Nijmegen, Netherlands.
2. Giant thermal expansion of 2D supramolecular networks tuned by alkyl chain functionalization. **Scherb, S.**; Hinaut, A.; Pawlak, R.; Vilhena, J. G.; Liu Y.; Feng X.; Müllen K.; Glatzel, Th.; Narita A. and Meyer, E. *iSPM³*, 2021-07-01, online, USA.
3. Giant thermal expansion of 2D supramolecular networks by alkyl chain functionalization. **Scherb, S.**; Hinaut, A.; Pawlak, R.; Vilhena, J. G.; Liu Y.; Feng X.; Müllen K.; Glatzel, Th.; Narita A. and Meyer, E. *28th International Colloquium on Scanning Probe Microscopy*, 2020-12-11, online, Japan.
4. Large thermal expansion of a 2D supra-molecular network in UHV. **Scherb, S.**; Hinaut, A.; Vilhena, J. G.; Pawlak, R.; Müllen K.; Glatzel, Th.; Narita A. and Meyer, E. *International Scanning Probe Microscopy*, 2019-05-27, Louvain-La-Neuve, Belgium.
5. Large thermal expansion of a self-assembling monolayer in UHV. **Scherb, S.**; Hinaut, A.; Vilhena, J. G.; Pawlak, R.; Narita A.; Glatzel, Th. and Meyer, E. *DPG Spring Meeting*, 2019-04-04, Regensburg, Germany.

Posters

1. Thermal expansion of 2D supramolecular networks tuned by alkyl chain functionalization. **Scherb, S.**; Hinaut, A.; Pawlak, R.; Vilhena J. G.; Liu Y.; Feng, X.; Müllen K.; Glatzel, Th.; Narita A.; and Meyer, E. *Swiss Nano Convention*, 2021-06-24, Fribourg, Switzerland.
2. Giant thermal expansion by alkyl chain fluctuations. **Scherb, S.**; Hinaut, A.; Pawlak, R.; Vilhena J. G.; Feng, X.; Glatzel, Th.; Narita A.; and Meyer, E. *SAOG Meeting*, 2020-01-30, Fribourg, Switzerland.

3. Two-dimensional supramolecular networks formed by intermolecular interdigitation. **Scherb, S.**; Hinaut, A.; Pawlak, R.; Vilhena J. G.; Liu, Y.; Freund, S.; Liu Z.; Feng X.; Müllen K.; Glatzel, Th.; Narita A. and Meyer, E. *Chirality@The Nanoscale*, 2019–10–14, Ascona, Switzerland.
4. Large thermal expansion of a 2D supramolecular assembly. **Scherb, S.**; Hinaut, A.; Pawlak, R.; Vilhena, J. G.; Glatzel, Th.; Narita A.; and Meyer, E. *The 22nd International Confereee on Non-contact Atomic Force Microscopy*, 2019–07–29, Regensburg, Germany.